



**University of Crete
Department of Physics**



**Institute of Electronic
Structure and Laser**

Study of luminescence of optically pumped transition metal dichalcogenides for use in polariton devices

Andriani Vervelaki

*Thesis
for the Master degree*

Thesis supervisor: Dr. Deligeorgis Georgios

Table of Contents

1 Motivation – Introduction.....	5
2 Theory.....	6
2.1 MoS ₂ material.....	6
2.1.1 Structural properties.....	6
2.1.2 Electronic band structure.....	7
2.1.3 Optical properties - excitons.....	7
2.2 Fabrication techniques.....	8
2.2.1 Exfoliation.....	8
2.2.2 Van der Waals epitaxy.....	9
2.2.3 Chemical Vapor Deposition.....	9
2.3 Transfer process.....	10
2.3.1 PMMA-mediated transfer method.....	11
2.4 Surface treatments.....	11
2.4.1 TFSI treatment.....	11
2.5 Optical cavities.....	14
2.5.1 Fabry - Perot resonator.....	14
2.5.2 DBR cavities.....	16
2.6 Polaritons.....	19
2.6.1 Exciton polariton.....	19
3 Experimental techniques (methods).....	24
3.1 Raman.....	24
3.1.1 Theoretical background.....	24
3.1.2 Experimental set-up.....	25
3.1.3 Raman on 2D MoS ₂	26
3.2 Photo-luminescence.....	31
3.2.1 Theoretical background.....	31
3.2.2 Photo-luminescence Experimental set-up.....	32
3.2.3 PL on 2D MoS ₂	33
3.3 MoS ₂ CVD growth.....	38
3.4 2D material transfer.....	38
3.5 MoS ₂ surface treatment.....	39
3.5.1 TFSI treatment.....	39
4 Results and discussion.....	40
4.1 CVD grown samples.....	40
4.1.1 Optical microscopy.....	40
4.1.2 Raman spectrum.....	41
4.1.3 Photoluminescence spectrum.....	43
4.2 2D material transfer.....	56

4.3 Chemical treatments - TFSL.....	65
4.3.1 Optical Microscopy.....	66
4.3.2 Raman spectrum.....	67
4.3.3 PL spectrum.....	68
4.4 Encapsulation / Stacking.....	80
4.4.1 Encapsulation.....	80
4.4.2 Stacking.....	82
5 Conclusions.....	85
6 Literature.....	87

Acknowledgements

First and foremost, I would like to express my sincere gratitude to my supervisor, Dr. Deligeorgis Georgios, for the continuous support, patience, motivation and immense knowledge. His guidance and support has been invaluable all the time of research and writing this thesis. In addition, I would like to thank the rest of my thesis committee, Prof. Iliopoulos Eleftherios and Prof. Savvidis Pavlos for the time spent on my account and their insightful comments.

My sincere thanks and appreciation also goes to Dr Iacovella Fabrice and Mavrotsoupakis Emmanouil for their excellent cooperation. Their assistance in sample preparation and measurements were crucial to complete my research. Special thanks to Ballas Ioannis for the valuable assistance during the last days of my research work. In addition, I thank all of them, for all the sleepless nights we were working together and for all the fun we have had.

Last but not least, it is my privilege to express my gratitude to my family and friends for all the their encouragement, support and patience during this time.

1 Motivation – Introduction

Monolayer Molybdenum Disulfide is a 2D material that belongs to the family of TMDs. It is a direct bandgap semiconductor and it exhibits promising optical properties that have attracted scientific attention. Because of the strong Coulomb interactions that result from its 2D nature, excitons are formed with very high binding energies (hundreds of meV) and dominate the optical emission even at room temperature. This opens the way towards the formation of room temperature exciton-polaritons which is a difficult task using classical 3D semiconductors that due to their exciton formation energy require cryogenic temperatures.

However, the quality of the material is influenced by defects that restrict its final performance. Chemical Vapor Deposition is a leading technique for the large area synthesis of monolayer TMDs but it creates defects during growth. The transfer of the grown material to another substrate is often necessary but further affects the quality of the material. Overall, the need to control and improve the Photoluminescence emission of the MoS₂ arises so that it can be used in polaritonic applications.

The scope of this thesis, is the study and optimization of the optical properties of CVD-grown monolayer MoS₂. An organic superacid, bis(trifluoromethane)-sulfonimide (TFSI), was used to improve the optical emission of the monolayer. Optical microscopy, Raman and Photoluminescence spectroscopy were the techniques used to evaluate the changes that occur in the material. Further insight to the quality of the material was given by temperature and power dependent PL measurements. Finally, we studied the interaction of the sample with the environment and the influence of exposure to the pump laser beam to the material's response.

2 Theory

2.1 MoS₂ material

MoS₂ is a two-dimensional material that belongs to the family of layered TMDs. These materials are represented with the chemical formula MX₂, where M is a transition metal atom while X is a chalcogen atom. Each layer of these materials consists of 3 hexagonal atomic planes: the M atom plane is sandwiched between two X atom planes, X-M-X, and the atoms interact with covalent bonds. The layers have a typical thickness of 6-7Å and they are kept together by weak van der Waals forces. Among the TMDCs, molybdenum disulfide (MoS₂) is one of the most commonly studied because of its availability. It also has promising properties for photonic, electronic and optoelectronic applications and its semiconducting nature gives it an advantage compared to the gapless graphene. [1]–[5]

2.1.1 Structural properties

Monolayer MoS₂ has a similar hexagonal layered structure to graphene but with the differences mentioned in the previous paragraph.

The bulk MoS₂ is found in three polymorphs (1T, 2H, 3R), which are specified by their stacking order and atom coordination. (figure 1) The 1T type has trigonal symmetry with one layer in the unit cell, the 2H has hexagonal symmetry with two layers in the unit cell and the 3R has rhombohedral symmetry with three layers in the unit cell. The 2H and 3R structures have trigonal prismatic coordination and can be found in nature while the 1T has octahedral coordination. Finally, the 1T and 3R types are metastable and they can be transformed into 2H through heating. [2], [5]

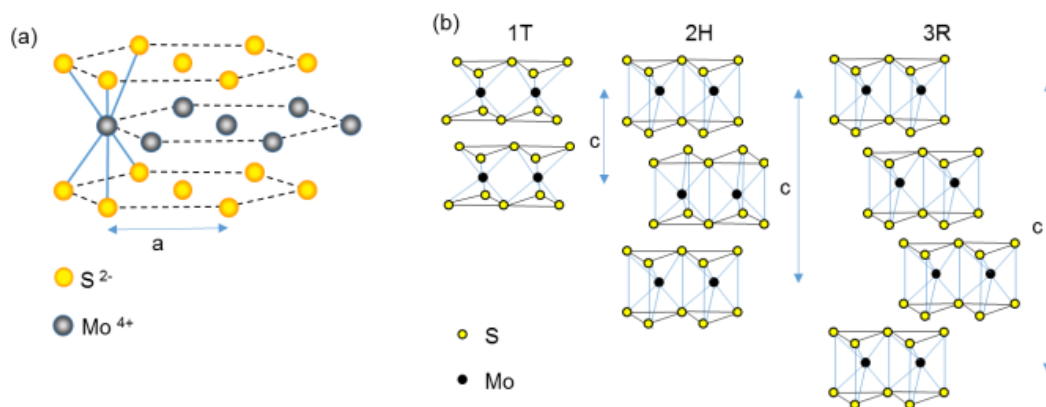


Figure 1: a) Hexagonal structure of S and Mo planes in a monolayer MoS₂. (b) The 1T/2H/3R type structures of bulk MoS₂. Reprinted from [2]

2.1.2 Electronic band structure

The electronic band structure of MoS₂ is strongly dependent on the layer number. This occurs because the quantum confinement in the axis perpendicular to the layer's surface alters the band structure. In bulk MoS₂, an indirect bandgap of ~1.2 eV appears between the Γ point of the top of the valence band and the point halfway between the Γ and K points of the conduction band. There is also a direct bandgap at the K point, which is higher in energy than the indirect bandgap. As the number of layers decreases, the indirect bandgap drastically increases, while the direct bandgap changes only slightly (less than 0.1 eV). Finally, when the material is thinned down to a monolayer, the indirect bandgap exceeds the direct bandgap and as a result, monolayer MoS₂ is a direct bandgap material of ~1.9 eV. [2], [3], [5] All these schematically appear in figure 2.

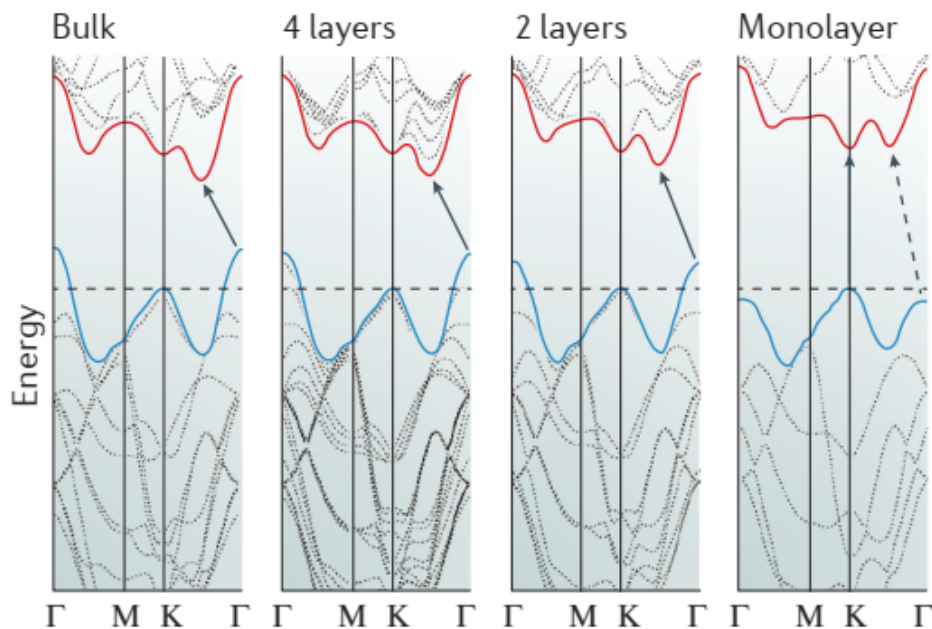


Figure 2: Band structure evolution with layer number of 2H MoS₂. Reprinted from [3]

2.1.3 Optical properties - excitons

In contrast to traditional 3D crystals, excitons in monolayer MoS₂ dominate the optical phenomena because of the strong Coulomb interactions that result from spatial confinement in the in-plane direction and reduced dielectric screening. Due to the lack of inversion symmetry, spin-orbit coupling causes valence band splitting which causes the appearance of two distinct excitons, called A and B. These excitons are easily observed in the absorption and emission spectra (photoluminescence). Also, the

n-character of the material helps the formation of negatively charged excitons, trions, which also appear in the emission spectra. In figure 3, the absorbance and PL spectrum evolution with the thickness of the material are presented. The quenching of the PL emission with the layer number can be easily explained by the direct to indirect bandgap transition. [2], [3], [6], [7]

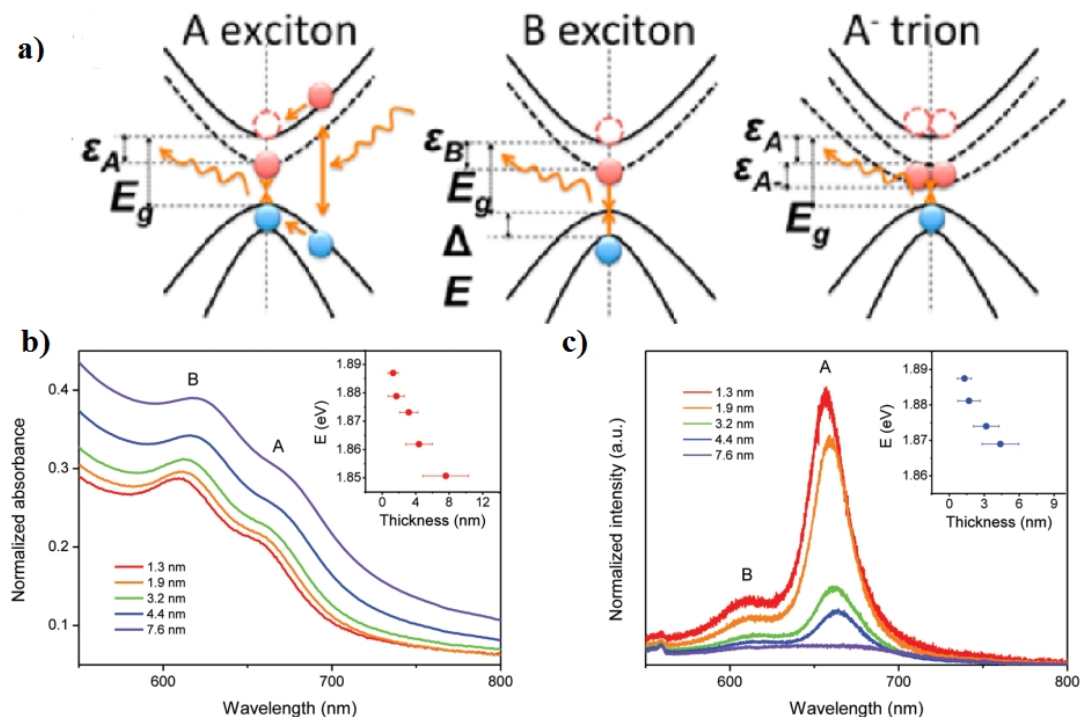


Figure 3: a) Schematic representation of light absorption and the exciton related radiative transitions at the K-point in the Brillouin zone. Reprinted from [8] b) absorption and c) photoluminescence spectrum evolution with the layer number (thickness). Reprinted from [7]

2.2 Fabrication techniques

Since the successful exfoliation of graphene in 2004, there has been a great progress in the field and alternative methods have been used for the production of monolayer samples. Below, we present the basic three categories that are mainly used.

2.2.1 Exfoliation

Mechanical exfoliation using scotch tape (or generally an adhesive tape) is a simple method that is based on peeling off a material many times. Eventually, a monolayer can be produced starting from its bulk form. This method produces high quality samples and requires only a bulk crystal, an optical microscope and the tape. So, it is very popular for fundamental research. However, it is not suitable for large scale

production as it produces low yield flakes whose size and layer count are not easily controllable.

Chemical exfoliation is an alternative method that gives higher production but it comes with the cost of lower flake size and the creation of defects in the lattice. The most widely used techniques include ion intercalation and/or ultrasonication . [1], [3]–[5]

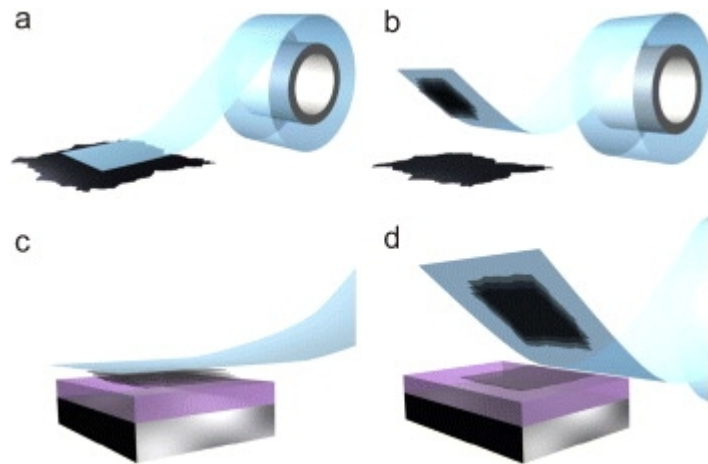


Figure 4: Schematic representation of micromechanical exfoliation of 2D crystals. Reprinted from [9]

2.2.2 Van der Waals epitaxy

This method is a MBE-based (Molecular Beam Epitaxy) growth method but with some differences from the traditional 3D epitaxy. The lattices of the materials used (the substrate and the grown material) don't have to be well matched because the growth proceeds with a van der Waals interaction. The substrates used in the method are either other layered materials or 3D materials with passivated surfaces. The method includes an ultrahigh vacuum chamber, the precursors that are usually evaporated from elemental sources and the substrate which is usually heated. [3], [10]

2.2.3 Chemical Vapor Deposition

CVD is one of the most promising and practical techniques for uniform, large-area and high quality growth of TMDCs. A general and very simple description of the technique is the following: The precursor gases flow into a vacuum chamber which contains the (heated) substrate. Then, thermally assisted chemical reactions occur between the precursors which lead to the deposition of a thin film on the surface. The precursor gases that did not react and the chemical by-products are pumped out of the chamber. An inert carrier gas, such as N_2 , is sometimes introduced into the chamber to transport the vapors from its sources to the substrate. One of the main disadvantages

is the random lattice orientation which results in the formation of grain boundaries. [1], [3], [11], [12]

This deposition method has been used in our work for the growth of monolayer MoS₂ and the details for the parameters used will be described in 3.3.

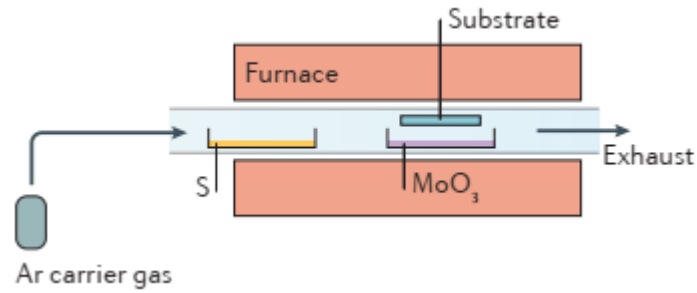


Figure 5: Schematic illustration of the CVD synthesis setup of MoS₂. Reprinted from [3]

2.3 Transfer process

The need to transfer the monolayer sample from the substrate that was used during growth to another substrate often arises. For this purpose, many transfer methods have been developed. The most frequently used techniques are the PMMA carrying layer method, the elvacite method, the wedging method, the transfer by all-dry viscoelastic stamping (PDMS), thermal release tapes and the van der Waals pick-up method. Each category of the above has its own variations and their extend presentation is beyond the scope of this thesis. The following table briefly presents a comparison of some basic categories. [13]–[17]

The method used in the present work is the PMMA carrying layer method which will be described in the next paragraph.

Method	Cleanness	Easiness	Speed	Notes
PMMA carrier layer	***	***	***	Spin-coating is needed, direct contact with polymer.
Elvacite sacrificial layer	*	***	***	Capillary forces, spin-coating is needed, direct contact with polymer.
Wedging	*	**	***	Capillary forces, dip-coating is needed, difficult alignment, direct contact with polymer, transfer over curved or uneven surfaces is possible.
PDMS dry transfer	***	*****	*****	Direct contact with polymer.
Van der Waals pick-up	*****	*	**	Spin-coating is needed, several steps involved, only works to transfer heterostructures, direct contact with the polymer only for the topmost layer.

Figure 6: Comparison between the different transfer methods. Reprinted from [14]

2.3.1 PMMA-mediated transfer method

The basic characteristic of the method is that the 2D material is coated by PMMA (polymethyl methacrylate) but beyond that there are many variations of the method. One technique is to use a water soluble intermediate layer between the substrate and the 2D flake. The stack is then immersed in DI water where the PMMA supported 2D flake is released. This technique is used in ex-foliated samples. In CVD grown samples, the method involves etching of the substrate (for example SiO₂ or Cu). After the wet transfer and some drying procedure, the most common step is to dissolve the PMMA layer in acetone.

The main problems that result from the technique are the following:

- Contamination that happens during etching. Atoms coming from the etching solution (e.g. Cl⁻ when HCl is used) stick to the monolayer. Also, incomplete etching can lead to substrate residues on the monolayer (for example Cu when it is used as a substrate).
- Water is often trapped underneath the monolayer when the monolayer is scooped out from the DI water by the target substrate. Sample drying results in the appearance of holes, wrinkles and cracks originating from mechanical stress.
- The PMMA removal is usually incomplete leaving PMMA residues on the surface of the monolayer which is another source of surface contamination. [15]–[17]

The detailed description of the procedure followed is presented in 3.4.

2.4 Surface treatments

2.4.1 TFSI treatment

An organic superacid, bis(trifluoromethane)sulfonamide (TFSI), was reported by Amani et al to drastically enhance the photoluminescence quantum yield of exfoliated MoS₂. [18] The degree of the PL enhancement depended on the quality of the sample. The achieved quantum yield was higher than 95% in low excitation power (~200 enhancement). Based on a simple model, the recombination mechanisms in a MoS₂ monolayer are:

1. radiative recombination of excitons (which is proportional to exciton concentration $\langle N \rangle$),
2. non-radiative biexcitonic recombination ($\propto \langle N \rangle^2$) which dominates in high pump power and

- defect-mediated non-radiative recombination ($\propto n^2$, n is the concentration of optically generated electrons which equals with holes).

When the TFSI treatment is used, the defect-mediated recombination (the latter) is suppressed. This model explains the linear pump-power dependence of emission at low power ($<10^{-2} \text{ W cm}^{-2}$) and the sublinear behavior in higher power. A possible explanation is the reduction/passivation of S-vacancies caused by the rearrangement of S-adatoms on the surface. This hypothesis is supported by the increase in ratio of S/Mo as shown by XPS data. (before: 1.84 ± 0.04 , after: 1.95 ± 0.05) Also, the technique is effective only in S-based TMDs while the emission on Se-based 2D materials seems to be slightly lower after treatment. [18], [19] In a latter study, they also observed a great PL enhancement (x20-60) but it appeared only in high temperatures. In low temperatures, the intensity of the peaks did not increase. However, there was an important reduction in the emission of localized states. [20] Other studies have reported $\sim x20 - 80$ times enhancement. [17], [21]–[23] In contrast to what has been mentioned so far, in a recent work by Molas et al. [24], the enhancement in the room temperature PL was not significant (2-fold increase). Their findings suggest that trion emission quenches and the neutral excitons redshift after treatment. They attributed this behavior to the passivation of doping centers which causes the reduction of the carrier density and subsequently the out of plane electric field in the sample

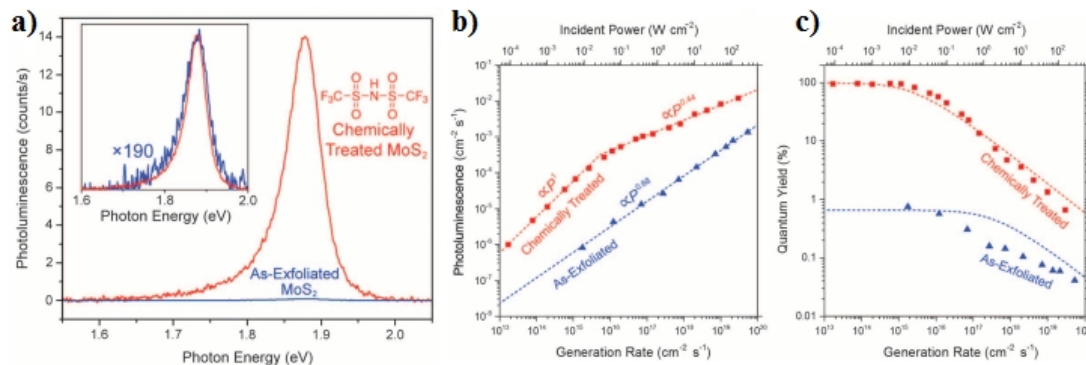


Figure 7: a) PL spectrum of as-exfoliated and TFSI treated samples. The power dependence of the b) integrated PL intensity and c) QY. Reprinted from [18]

In order to understand the mechanism of the treatment, the importance of the protonated environment and the acidity of the solvents were studied. TFSI and sulfuric acid were the two acids tested while DCE, acetonitrile and water the three different solvents under study. It is suggested that due to higher acidity, the DCE shows higher enhancement (x20) compared to the other two (x6). Using the same solvent (water in this case), the TFSI and H₂SO₄ showed similar enhancement (x4-8) which indicates that the protonation environment is more important than the counter

anions as far as the degree of PL enhancement is concerned. [22] The importance of cations is also mentioned by Yu et al. They attributed the PL enhancement and blueshift of the peak to the intercalation of cations between the monolayer and the substrate (H^+ and Li^+ coming from TFSI and Li-TFSI). They claimed that intercalation causes p-type doping of the material and also decreases the interaction with the substrate. The p-doping was supported by PL, Raman and XPS data. The p-doping alone could explain the results of samples that were transferred before the treatment but not the effect of the treatment on as-grown samples as well. Treated as-grown samples did not show the expected reproducibility and in combination with other observations, such as AFM measurements which showed an increase in the height of as-grown monolayers (from 0.7 to 1.1 nm) after TFSI treatment, indicating the intercalation of the cations rather than just their adsorption on top of the monolayer. [25]

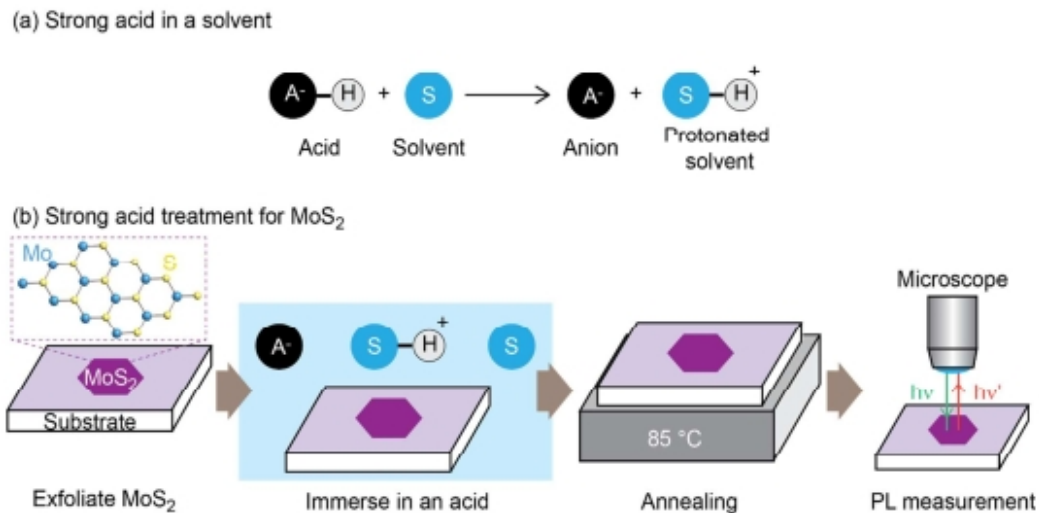


Figure 8: a) Representation of the dissociation of acids in a solvent and b) the experimental procedure of the treatment. Reprinted from [22]

A different study with CVD grown samples, used a slightly different method and the results were slightly different as well. Acetonitrile was proposed to be a better solvent than DCE/DCB which is commonly used in exfoliated samples. Also, the technique showed significant improvement only when the as-grown monolayer was transferred to a different substrate which was attributed to strain release. Finally, it was found that Sulfur-precursor temperature during growth plays a critical role in the efficiency of the method where the highest QY (quantum yield) was observed in sulfur deficient conditions. This observation agrees with the hypothesis that TFSI passivates S-vacancies. Under optimized conditions, the maximum QY reached was ~30%. [17]

Alharbi et al also studied CVD grown MoS₂ and found that TFSI treatment (using DCE/DCB as a solvent) decreases the density of the trap states in S-deficient conditions. They further noted that the relative emission of excitons to trions increases upon treatment. The presence of S-vacancies causes enhanced local charge which helps the trion formation and is a possible explanation for this effect. [21]

Many studies reported that the treatment does not alter the structure or induce strain which was supported by the Raman spectrum. [17], [18], [21]

The experimental procedure that was followed in the current work will be presented in 3.5.1.

2.5 Optical cavities

2.5.1 Fabry - Perot resonator

Optical resonators are used to confine and store photons of certain frequencies. This is the result of constructive interference of the reflected beams in the cavity. Below, we are going to present the basic characteristics of the well-known Fabry-Perot microcavity. It consists of two parallel planar (metallic) mirrors of reflectivities R_1 and R_2 that are placed opposite to each other at a distance L_{cavity} . We also set

$R = \sqrt{(R_1 R_2)}$ for the following analysis.

The photon states are quantized in the vertical direction of the mirrors surface. The longitudinal resonant modes λ_m are given by the following formula:

$$\frac{m\lambda_m}{2} = n_{cavity} L_{cavity} \text{ or } f_m = m \frac{c}{2 L_{cavity}} \quad \text{Equation 1}$$

where m =integer c : the speed of light in vacuum and n_{cavity} : the refractive index of the cavity

The photon's wavevector can be analyzed into two components, one perpendicular (k_{\perp}) and one parallel to the mirror's surface (k_{\parallel}). The perpendicular is defined by the cavity length as we mentioned above, while the parallel has no confinement. So, the cavity photon energy is parabolic for small k_{\parallel} :

$$E = \frac{\hbar c}{n_{cavity}} k = \frac{\hbar c}{n_{cavity}} \sqrt{\left(\frac{\pi m}{L_{cavity}}\right)^2 + k_{\parallel}^2} \Rightarrow E \simeq \frac{\hbar c \pi m}{n_{cavity} L_{cavity}} \left(1 + \frac{L_{cavity}^2 k_{\parallel}^2}{2 \pi^2 m^2}\right) \quad \text{Equation 2}$$

where $k_{\parallel} = \frac{\omega}{c n_{cavity}} \sin(\varphi)$, φ : the incident angle

Two important characteristics of the cavity are the Free Spectral Range (FSR) and the Full Width Half Maximum (FWHM) which are the mode frequency separation and the linewidth of the modes respectively.

The FSR is constant and is given by the formula:

$$\Delta f_{FSR} = \frac{c}{2L} \quad \text{Equation 3}$$

The finesse of a Fabry-Perot cavity is defined as its free spectral range divided by the full width at half-maximum bandwidth of its resonances. It essentially shows the number of reflections in the cavity and depends only from the mirrors' reflectivity:

$$F = \frac{\Delta f_{FSR}}{\Delta f_{FWHM}} = \frac{\pi \sqrt{R}}{1 - R} = \pi N \quad \text{Equation 4}$$

where N is the mean number of reflections in the cavity

The finesse is also connected with the photon lifetime in the cavity:

$$\tau = \frac{N t_{roundtrip}}{2} = \frac{1}{2\pi \Delta f_{FWHM}} \quad \text{Equation 5}$$

where $t_{roundtrip}$ is the photon's roundtrip time

The quality factor Q is used to characterize the losses and is defined as:

$$Q = \frac{f_m}{\Delta f_{FWHM}} \quad \text{Equation 6}$$

Finally, it can be shown that an approximation for the resonant intensity of the field in an anti-node is:

$$I_{intracavity} \approx \frac{4}{1 - R} I_{incident} \approx 4 \frac{F}{\pi} I_{incident} \quad \text{Equation 7}$$

The above analysis was based on [26]–[31]

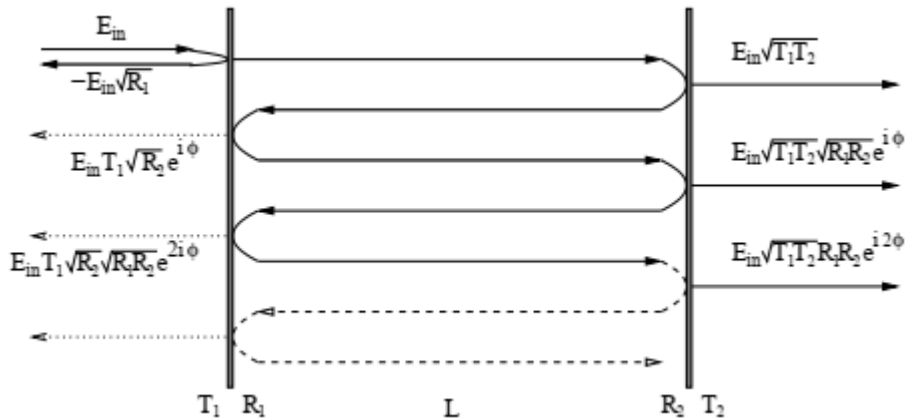


Figure 9: Schematic representation of the Fabry-Perot cavity and the partial reflections/transmissions of the incident beams. Reprinted from [28]

2.5.2 DBR cavities

The maximum reflectivity that can be reached using metallic mirrors is limited by the dielectric constant of the metal. In contrast, DBR cavities offer the opportunity of controlling the reflectivity of the mirrors around the desired wavelength. [26] DBR cavity is actually a Fabry-Perot interferometer that consists of two planar DBR mirrors.

2.5.2.1 Distributed Bragg Reflector (DBR)

DBR is a multilayer structure that acts as a high reflectivity mirror in a bandwidth around a chosen wavelength. It consists of films of two different alternating optical materials and the optical thickness of the layers is chosen to be equal to one quarter of the desired wavelength. [32] (figure 10) In other words, DBRs obey to the condition:

$$n_{\text{high}}d_{\text{high}}\cos(\theta_1)=n_{\text{low}}d_{\text{low}}\cos(\theta_1)=\lambda_0/4 \quad \text{Equation 8}$$

Where: n_{high} , n_{low} are the refractive indices of the two materials (the one is much higher than the other), d_{high} , d_{low} are the thicknesses of these materials, λ_0 is the design vacuum wavelength and θ_1 is the angle of incidence.

This condition leads to constructive interference of the reflections that originates from each boundary, resulting in a high reflectance at the front surface. Increasing the number of layers enhances the reflectance. So, our structure can have the desired reflectivity at the desired wavelength, determining the refractive indices, the thicknesses and the number of layers.

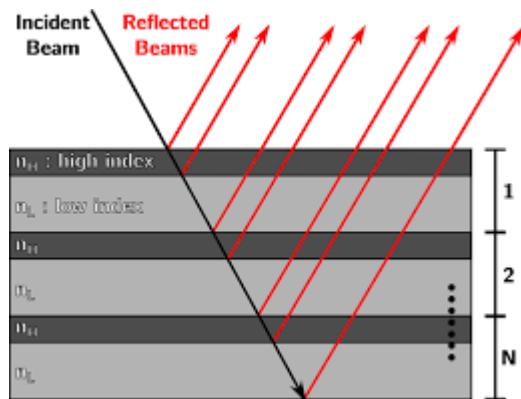


Figure 10: Structure of a DBR. It consists of N layers with alternating refractive indices n_H and n_L . Reprinted from [33]

The transfer matrix method is used to describe the propagation of electromagnetic waves through a stack of layers. It assumes that the field within one layer is the superposition of a left- and right-traveling wave and can be represented by a vector. Based on the Fresnel equations and the boundary conditions that demand the E/M waves to be continuous across the interfaces between the layers, we can derive the matrix that transfers the wave from the one layer to the next. After some calculations, it comes out that the matrix that relates the waves between two successive layers is:

$$M_n = \begin{pmatrix} e^{-i\theta_n} & 0 \\ 0 & e^{i\theta_n} \end{pmatrix} \begin{pmatrix} 1 & r_{n,n+1} \\ r_{n,n+1} & 1 \end{pmatrix} \frac{1}{t_{n,n+1}} \quad \text{Equation 9}$$

where $r_{n,n+1}$, $t_{n,n+1}$ the reflection and transmission coefficients in the boundary of layers n , $n+1$ and θ_n the phase that the wave obtains passing through the layer n

Multiplying all the matrices and considering that the light that enters the structure satisfies: $f_1=1$, $b_1=r$ while the light that exits the structure: $f_n=t$, $b_n=0$ (where f , b are the wave amplitudes that move forwards and backwards), we can derive the formula for the reflected intensity which is $R=|r|^2$. [34]

An example of a reflectivity spectrum, which was calculated based on the above analysis, is presented in figure 11.

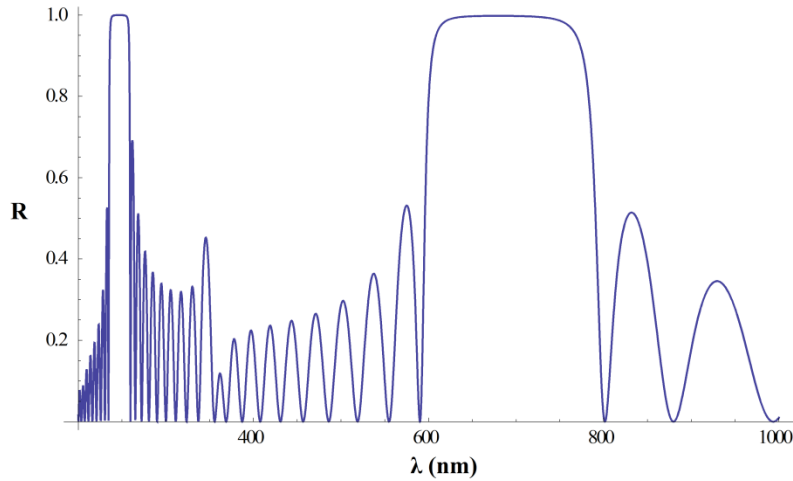


Figure 11: Calculated reflectance using transfer matrix method for a DBR designed at 680nm. It consists of 10 layer pairs of alternating MgF_2 , Si_3N_4 . The refractive indices of the two materials are approximated by Cauchy formula.

2.5.2.2 Special characteristics of the DBR cavity

In contrast to metallic cavities, the penetration of the cavity field into the DBRs is noticeable when we refer to DBR cavities. So, the effective length of the cavity is:

$$L_{eff} = L_c + L_{DBR} \quad \text{Equation 10}$$

where L_{DBR} represents the penetration length mentioned previously and is given by the following formula:

$$L_{DBR} = \frac{\lambda_0}{2n_{cavity}^2} \frac{n_{low}n_{high}}{n_{high} - n_{low}} \quad \text{Equation 11}$$

The resonant mode frequency also changes if the Fabry-Perot frequency (ω_c) is not equal to the DBR's designed frequency (ω_{DBR}) which can be caused by the imperfectly controlled growth:

$$\omega = \frac{L_c \omega_c + L_{DBR} \omega_{DBR}}{L_{eff}} \quad \text{Equation 12}$$

[26], [29], [30]

The Transfer matrix method can be used in this case as well, as the cavity region is actually another layer which only differs in thickness and material used.

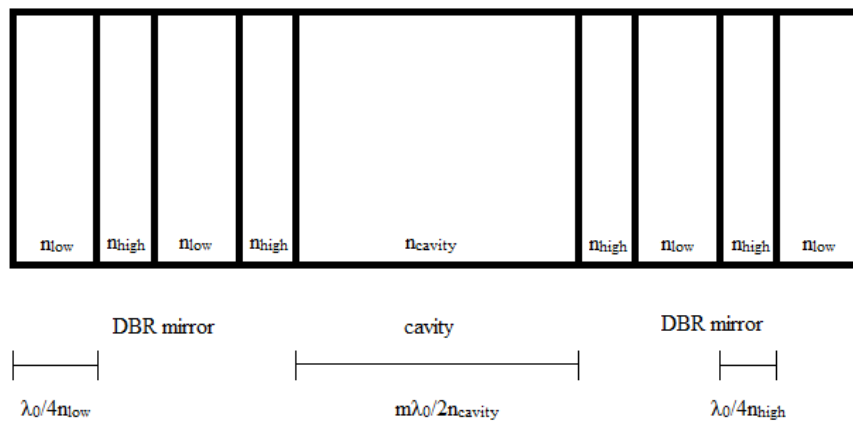


Figure 12: Structure of a DBR cavity.

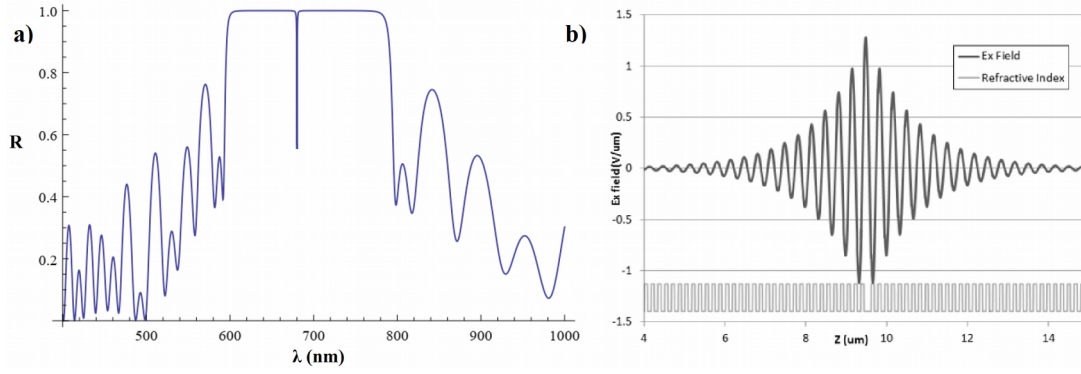


Figure 13: a) Reflectance of a DBR cavity. The first DBR consists of 7 layer pairs and the second DBR consists of 11 layer pairs. The materials used in the DBRs are MgF_2 and Si_3N_4 while the material of the active region is MgF_2 . b) The intensity distribution of the electric field and the refractive index profile of a typical microcavity. Reprinted from [26]

2.6 Polaritons

Polaritons are bosons resulting from the strong coupling of photons with other quasiparticles. They are distinguished in three types: [35], [36]

- Phonon polariton: Strong coupling of photon with a phonon
- Plasmon polariton: Strong coupling of photon with a plasmon
- Exciton polariton: Strong coupling of photon with an exciton

2.6.1 Exciton polariton

As mentioned before, an exciton polariton is created by the interaction of the electromagnetic wave (light) with an exciton and exhibits properties of both photon and exciton. [29]

2.6.1.1 Exciton

When a semiconductor absorbs light and as a result an electron is excited from the valence band into the conduction band, it leaves behind a positively charged hole. The electron and the hole are both charged and so they can form an atom like system due to the electrostatic coulomb attraction. The bound state of an excited electron and its hole is called exciton and it is a neutral quasiparticle (figure 14).

The excitonic energy is given by:

$$E_{ex}(n, k) = E_{gap} - \frac{\mu e^4}{32 \pi^2 \hbar^2 (\epsilon \epsilon_0)^2} \frac{1}{n^2} + \frac{\hbar^2 k^2}{2M} \quad \text{Equation 13}$$

where $\frac{1}{\mu} = \frac{1}{m_e} + \frac{1}{m_h}$, $M = m_e + m_h$, n is the principal quantum number (integer) and k is the combined electron and hole wavevector [31], [37]

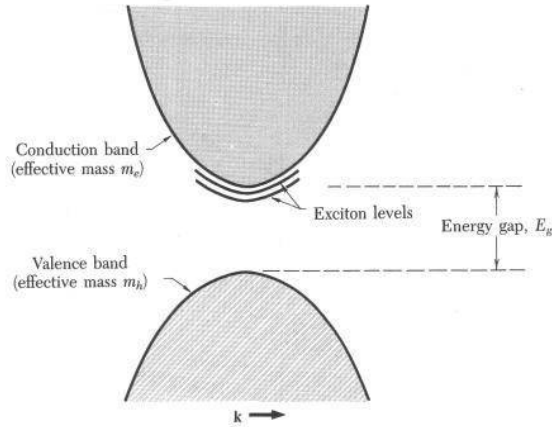


Figure 14: Representation of the conduction and valence band of a semiconductor. Exciton levels are also shown. Reprinted from [38]

2.6.1.2 Exciton polariton in microcavity

In order to create cavity polaritons, a quantum well (in our case a 2D material) is embedded in a DBR cavity whose resonance wavelength equals or is close to the wavelength of quantum well excitons. [29] However, the interaction between the photons confined in the cavity and the excitons of the material does not always lead to the polariton's formation. Actually, two regimes should be distinguished when the light interacts with matter: The strong coupling regime and the weak coupling regime.

In the weak coupling limit, the photon will be absorbed by the semiconductor and an exciton will be created. Then, the electron will recombine with the hole emitting a photon and this process will be repeated. The two systems are coupled but their states remain unchanged (crossing behavior).

In the strong coupling limit, the two states are so strongly coupled that can't be distinguished anymore (anti-crossing behavior). The energy of the system oscillates back and forth between the two modes, the cavity and the exciton modes. [29], [37]

In this limit, the polariton is created and in a semiclassical approach it can be considered as the coupling between two harmonic oscillators: the photon modes in the cavity and excitons of the quantum well. Coupling occurs between exciton and photon states of the same in-plane wavevector and similar energy and is influenced by two factors: the exciton oscillator strength and the amplitude of the cavity field at the position the quantum well/2D material is embedded. As photon- exciton has been considered a system of two harmonic oscillators, their coupling leads to energy splitting and formation of two new branches which are termed upper and lower polaritons and result from symmetric and antisymmetric combinations of the exciton and cavity mode (figure 15). [29], [39] The energy splitting is called vacuum Rabi splitting (Ω_v) and assuming the quantum wells are placed close to the electric field's antinodes it can be calculated by the following formula [29]:

$$\hbar\Omega_i \approx 2\hbar \left(\frac{2\Gamma_0 c N_{qw}}{n_c L_{eff}} \right)^{1/2} \quad \text{Equation 14}$$

Where: $\hbar\Gamma_0$ is the radiative width of a free exciton, N_{qw} the number of quantum wells in the cavity, n_c the cavity refractive index and L_{eff} the effective length of the cavity.

Based on the coupled oscillator model the interaction hamiltonian is a 2x2 matrix:

$$H_{inter} = \begin{pmatrix} E_{ex} + i\hbar\Gamma_{ex} & V \\ V & E_{cav} + i\hbar\Gamma_{cav} \end{pmatrix} \quad \text{Equation 15}$$

where $E_{ex}=E_{ex}(k_{||})$ and $E_{cav}=E_{cav}(k_{||})$ are the energies of the exciton and cavity modes, Γ_{ex} and Γ_{cav} are the FWHM of the bare cavity photon and exciton respectively and $V=\hbar\Omega_i/2$ the interaction potential. So, we have the system:

$$H_{inter} \begin{pmatrix} \alpha \\ \beta \end{pmatrix} = E_{pol} \begin{pmatrix} \alpha \\ \beta \end{pmatrix} \quad \text{Equation 16}$$

where $E_{pol}=E_{pol}(k_{||})$ are the eigenvalues of the polaritonic branches and α, β the hopfield coefficients where $|\alpha|^2$ and $|\beta|^2$ quantify the contribution of photonic and excitonic part to the photonic states respectively. [29], [40]–[42]

Exciton and photon have very different energy dispersion as a function of momentum (k). So, their energy modes are on resonance for a small range of in plane wavevectors where the polaritons (upper and lower) are full admixtures of exciton and photon modes in this region, which is called anticrossing region. Moving away from resonance, the lower branch becomes more exciton like while the upper branch more photon like. [29], [43]

Finally, a way to determine the nature of the system at hand, is to compare the vacuum rabi splitting (Ω_i) to the decay rates of the photon and exciton. If Ω_i is much greater than both the exciton and the cavity linewidths, the system is in the strong coupling limit. Otherwise, it is in the weak coupling limit and exhibits only classic crossing behavior. [26], [29], [31]

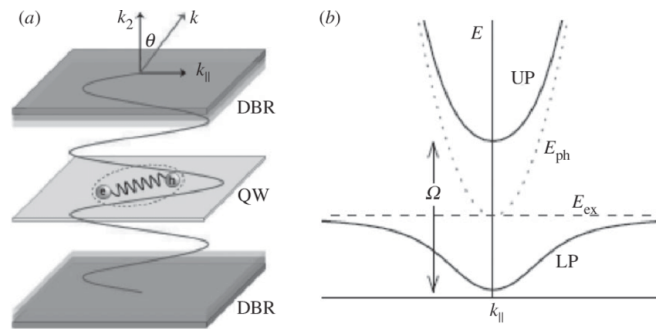


Figure 15: (a) An optical microcavity. A quantum well is placed between two mirrors, usually composed of DBRs. (b) Dashed line, dispersion of photons in a planar microcavity. Dotted line, energy of excitons in a quantum well resonant with the cavity photon energy. Solid lines, upper polariton (UP) and lower polariton (LP) modes. Reprinted from [39]

The coupled exciton-cavity modes can be observed in a reflectivity spectrum as two dips in the reflectivity that appear in the stop band of the DBR mirrors. An example of a quantum microcavity reflectivity spectrum for on-resonance case is shown in figure 16.

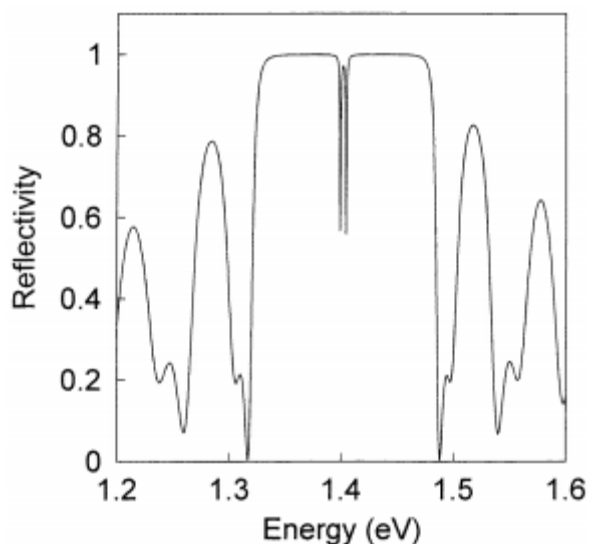


Figure 16: Calculated reflectivity spectrum for a microcavity for on-resonance case. The two coupled-mode polariton dips are superimposed on the high-reflectivity stop band of the DBR. Reprinted from [29]

2.6.1.3 Exciton polariton using TMDCs as the active medium

The formation of exciton polaritons require large exciton oscillator strength. TMDCs have big radiative decay rate of excitons (higher than 1 ps^{-1}) and as a result the oscillator strength (which is proportional to the radiative decay rate) is also high. This characteristic, in combination with the high exciton binding energy and the valley degree of freedom puts them in the center of attention and makes them promising candidates for polariton based devices and allows operation in room temperature, in contrast to cryogenic temperatures that were required in traditional inorganic semiconductors. [26], [44], [45]

After the first demonstration of room temperature cavity polaritons using MoS_2 from Liu et al in 2014 [45], many others followed using other TMDCs at room temperature, or lower temperatures [40]–[42], [46]–[48]. The Rabi splitting that has been reported by two different groups for cavities with embedded MoS_2 is around 40meV. [45], [46] The field was also approached theoretically: for example physicists calculated some characteristics of the polaritons (such as Rabi splitting, mode lifetimes etc) theoretically [49] while others tried to predict the basic parameters required for room-temperature superfluidity. [50]

In the literature, different experimental groups used different fabrication methods to achieve strong coupling. The mirrors used are usually DBRs because of their high finesse [40], [45], [46], [48] but metallic mirrors [47] (that offer the advantage of smaller mode volume), half metallic [42] or combination of metallic and DBR mirror [41] have also been used for the fabrication of the cavity. The monolayers are often grown by CVD method and then transferred to the bottom mirror [41], [45], [46] or they are exfoliated from its bulk form [40], [42], [47], [48]. Also, Dufferwiel and his team managed to construct the cavity with 2 monolayers placed at an electric field antinode, separated by a thin sheet of h-BN (3nm).[48]

In most studies, angle-resolved PL and reflectivity measurements were carried out to extract the dispersion relation. [40], [42], [45]–[47] However, some groups varied the cavity length instead with the assistance of a Piezo microactuator [41] or via nanopositioners [48]. In addition to their previous analysis, different detunings were also studied ($\Delta = E_{\text{ph}} - E_{\text{ex}}$) by modifying either the exciton part or the photon part. For example, Liu et al modified the exciton energy by using different temperatures [40] while Sun et al changed the cavity energy by changing the cavity length [47].

Finally, some groups showed that the exciton polaritons are valley polarized and the polarization is preserved even at room temperature. [46], [47]

3 *Experimental techniques (methods)*

3.1 Raman

Raman spectroscopy is based on inelastic scattering of light by the material under study (Raman scattering). This technique provides information about the vibrational modes of the material which help in finding its chemical composition, structure and concentration of the different substances. It further helps us to identify defects (which are related to its crystalline quality), the presence of strain and others. [51]–[53]

3.1.1 *Theoretical background*

3.1.1.1 Raman scattering

One of the main processes that emerge from the interaction between light and matter is scattering. The irradiation of a sample with monochromatic light that doesn't lead to absorption and causes the distortion of the molecule's electron cloud around the nuclei, leads to the formation of a short-lived state, the "virtual state". This state is not an excited state of the static molecule but a mixture of all ground and excited states. Due to the instability of this state, the electron quickly falls back to the ground level re-radiating a photon. When the relaxation of the electron cloud happens without any nuclear movement, the scattered light has very small difference in frequency compared to the incident photon. This elastic scattering that involves only electron perturbation is called Rayleigh. In contrast, the Raman scattering involves change in nuclear motion and the irradiated photon has different energy from the incident.

Raman scattering is divided into two categories, the Stokes and anti-Stokes. Stokes scattering occurs when the electron moves to a higher vibrational state after scattering and includes the emission of a phonon. In this case, the scattered light has lower frequency than the incident. Anti-Stokes scattering occurs when the electron moves to a lower vibrational state, includes the absorption of a phonon and the scattered light has higher frequency than the incident. Rayleigh scattering is the dominant scattering process while only one in 10^6 - 10^8 photons results from Raman process. The process that involves only one phonon is called first order Raman and the wavevector of the phonon is $k \approx 0$ because of the momentum conservation. When the frequency of the laser is close to the frequency of an electronic transition, the process is called resonance Raman scattering. [51]–[54]

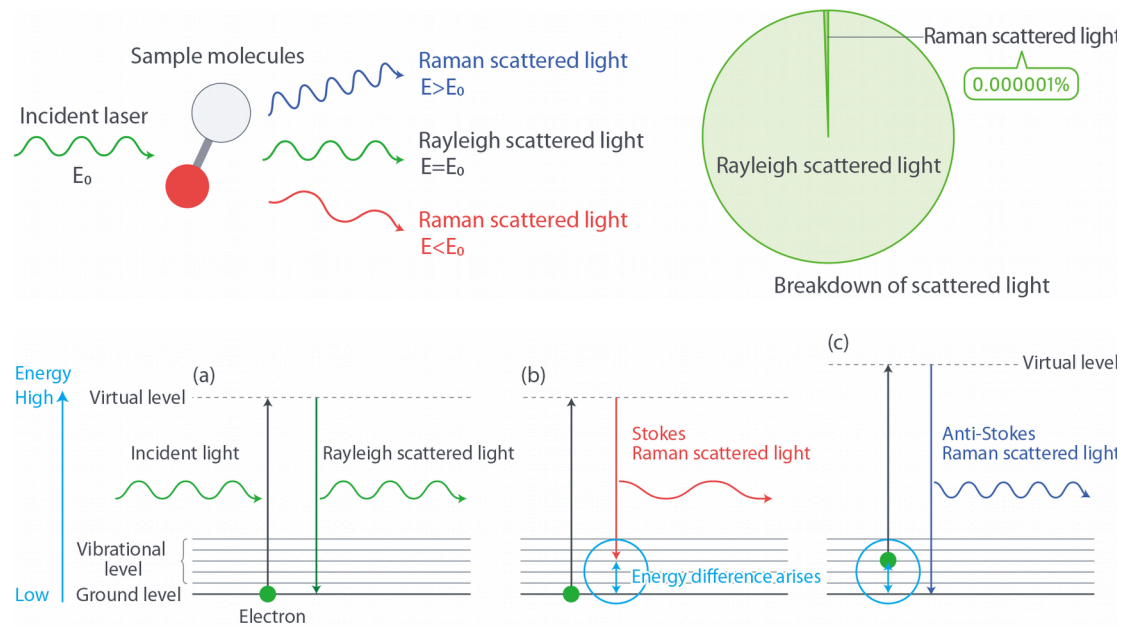


Figure 17: Representation of the scattering process and the energy diagram of Rayleigh and Raman scattering. Reprinted from [51]

3.1.1.2 Vibrational modes and selection rules

In contrast to absorption processes, Raman scattering does not require matching between the energy of the incident photon and the energy difference between the ground and excited states. On the contrary, the laser defines the energy of the virtual state.

A molecule which consists of N atoms has $3N-6$ vibrational degrees of freedom except from linear molecules which have $3N-5$. In crystals, which have N atoms per unit cell, there will be $3N$ phonon modes: The $3N-3$ of them are optical branches and the remaining 3 are acoustic.

However, not all the vibrations are Raman active. In order for a vibration to be Raman active, it is necessary to induce a change in the polarizability of the electron cloud. So, the most intense Raman scattering will come from symmetric vibrations as they give the largest changes. [52], [53], [55]

3.1.2 Experimental set-up

Usually, a laser is used as the light source whose beam is focused on the sample. The resulting scattered light consists mainly of elastic scattered light. In order to be able to detect the much weaker inelastic scattered component, a Notch filter cuts off the elastic scattered photons. Also, a high resolution grating diffracts the light and a CCD sensor converts the incident photons to electrical signal which is analyzed by the software. The described set-up is presented in figure 18.

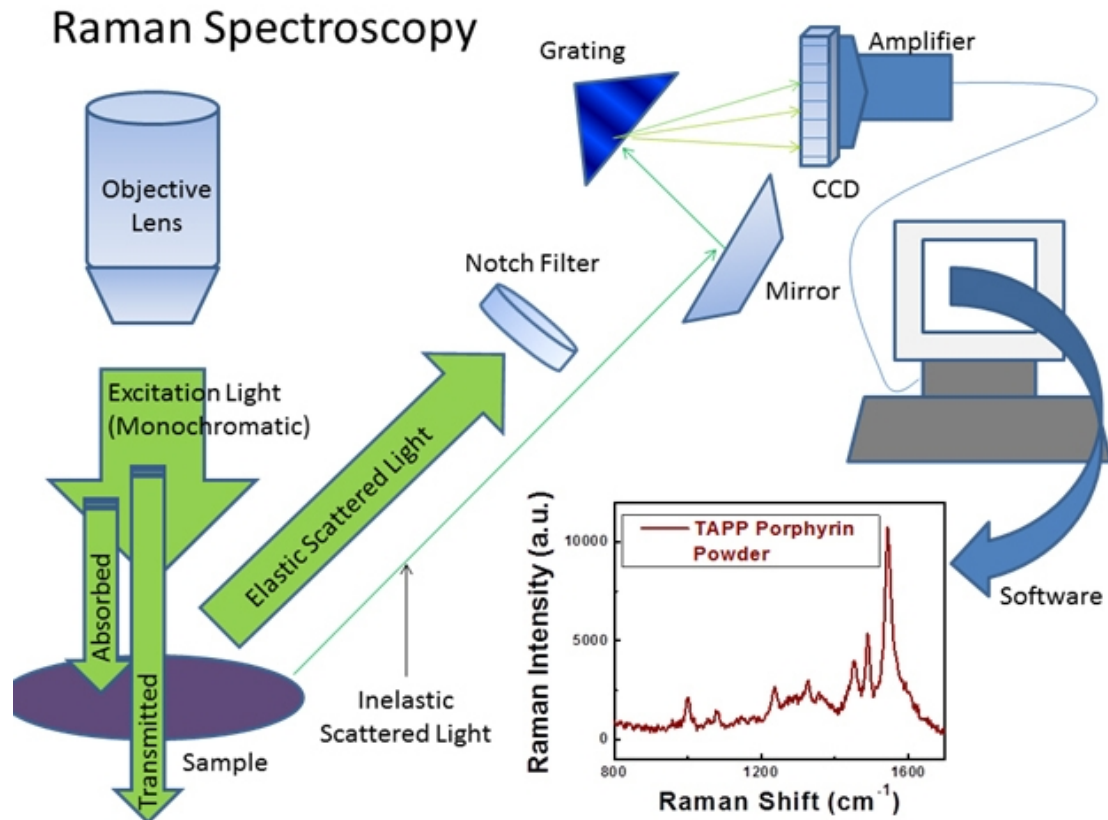


Figure 18: Simple schematic of a typical Raman set-up. Reprinted from [56]

In this work, a Thermo scientific Nicolet Almega XR Micro Raman system was used, including microscope objective lens and a diode pumped solid state laser (473nm).

3.1.3 Raman on 2D MoS₂

Each unit cell of bulk 2H-MoS₂ consists of 6 atoms while monolayer MoS₂ consists of 3 atoms. So, 18 and 9 phonon modes arise for bulk and monolayer MoS₂ respectively. From them, only 4 of them are Raman active: the out of plane mode A_{1g} and the in plane doubly degenerate modes E_{2g}¹, E_{2g}² and E_{1g}. In monolayer samples, these modes are called A₁['], E', E' (LA/TA) and E'' respectively. Among them, A_{1g} (A₁[']) and E_{2g}¹ (E') are usually detected and used to give important information about the material. [54], [57], [58] The peak positions of these modes and their spacing, their linewidth and their relative intensity are the main characteristics studied to determine the number of layers, strain, doping level, defect density, dielectric environment, interference effect and different substrates on these spectra as we will present in detail below. The excitation wavelength and power, the temperature of the environment and other parameters can also affect the Raman spectrum. [54], [59]

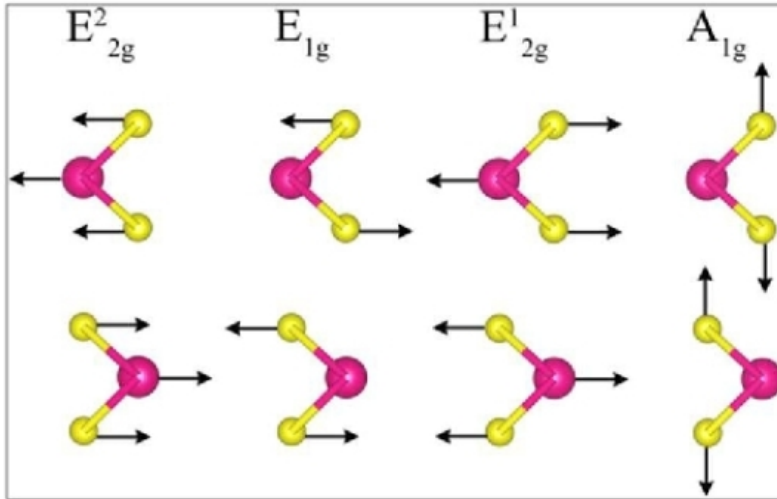


Figure 19: Raman active modes of bulk MoS₂. Reprinted from [60]

3.1.3.1 Effect of the layer number

Many studies have reported the dependence of E_{2g}^1 and A_{1g} peaks on the layer count and have indicated the peak spacing as a precise method to determine the layer thickness. Increasing the layer thickness up to four layers, the E_{2g}^1 mode softens while A_{1g} mode stiffens. For higher number of layers, the mode frequencies approach the value of the bulk. Taking into account the van der Waals interaction between the layers, a stiffening of the modes is expected as additional layers are added because the effective restoring forces are enhanced. This hypothesis explains the trend of the out of plane A_{1g} vibration but not the shift of the E_{2g}^1 mode. An important explanation for this anomalous behavior is the effect of dielectric screening. The long-range interlayer coulomb interactions lead to the increase of the dielectric screening as the number of layer increases. The effect is more prominent in Mo atoms and so E_{2g}^1 mode is mainly affected as it involves motion of Mo atoms. So, the redshift coming from the increased dielectric screening overcompensates the small effect of the increased van der waals interactions to this in plane mode. An alternative hypothesis based on stacking-induced structural changes in intralayer bonding has also been suggested. Changes in linewidth and integrated intensity of the peaks with the layer thickness have also been reported but it is difficult to be used as a tool to identify the number of layers. [2], [54], [57]–[59], [61]

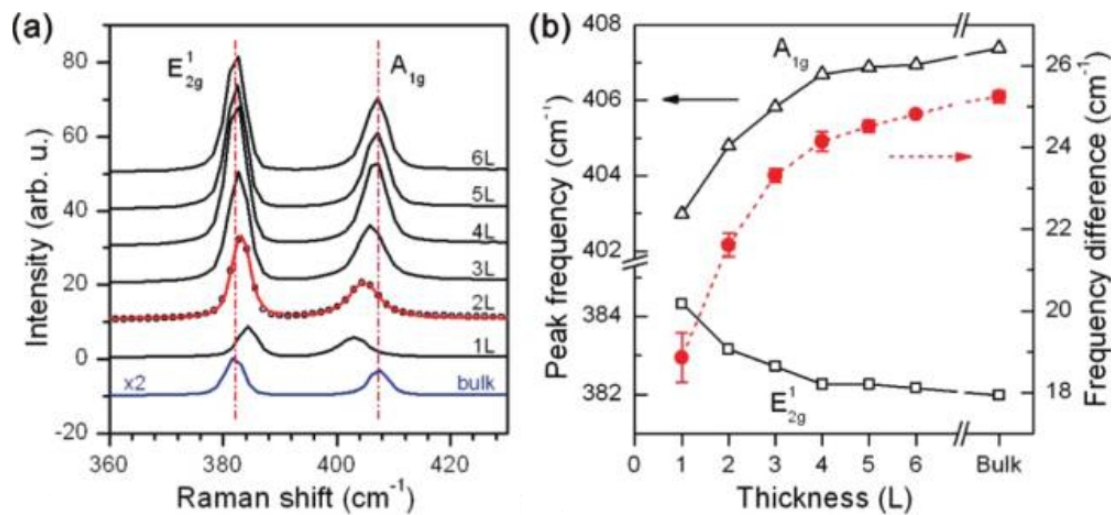


Figure 20: The evolution of (a) the Raman spectrum and (b) the peak positions with the number of layers. Reprinted from [57]

3.1.3.2 Strain effect

When the sample is grown by CVD process, biaxial strain is induced due to the difference in thermal expansion coefficients of the MoS₂ (or any TMD monolayer) and the substrate during the cooling process. When the monolayer is transferred to a different substrate the strain is released. [20], [21], [62] The application of strain influences the behavior of the phonon modes as the effective restoring forces between the atoms change.

Many groups have claimed that strain affects mainly the E_{2g}¹ mode and in a much smaller rate, the A_{1g} mode. [63]–[69] Rice et al used a linear fitting for the dependence of peak positions of E_{2g}¹ and A_{1g} modes from the application of uniaxial strain on a monolayer area. Their results show a softening of the modes at a rate -2.1 cm⁻¹/ % strain and -0.4 cm⁻¹/ % strain respectively for small amount of strain (<1%), which are in good agreement with their theoretical calculations based on DFT method (-2.22 cm⁻¹/ % strain and -0.55 cm⁻¹/ % strain). They also reported a broadening of the pristinely double degenerate E_{2g}¹ mode as strain increases which could be caused by unresolved splitting of the two subbands E_{2g}¹⁺, E_{2g}¹⁻. [63]

According to most of the studies, when the uniaxial strain is 1% or higher, the mode splits into the two singlet subbands and the integrated intensity of the mode also splits between the two bands. [64], [68], [70] For example, in another study, where the amount of strain applied was up to 2.2%, they did not find a measurable shift of A_{1g} mode while they observed the splitting of the E_{2g}¹ mode and measured different rate of change for the two bands: -4.5±0.3 cm⁻¹/ % strain for E_{2g}¹⁻ and -1.0±1 cm⁻¹/ % strain for E_{2g}¹⁺. [70]

Also, it has been shown that the intensities are strongly dependent on the angle between polarizations of the incident and scattered light, in contrast to the unstrained case (non-polar behavior of E_{2g}^1 mode). [64] Finally, in a theoretical study by Kukucska et al, the calculated intensity ratio of the two peaks (E_{2g}^1 and A_{1g}) is a more accurate way to identify the amount of strain than the frequency shift of the peaks. [65] However, the intensity ratio is influenced by many other parameters as well. So, the question that rises is if it will be indeed a useful method to identify strain.

In contrast to uniaxial strain, experimental research on biaxial strain is much more difficult. So, only a few teams have worked on this direction and have reported a higher effect on Raman (and PL) spectrum in comparison with uniaxial strain. [71]–[74] Li and his group generated a funnel effect using biaxial strain and noted a -4.48 and -1.02 $\text{cm}^{-1}/\%$ strain for E_{2g}^1 and A_{1g} modes respectively based on theoretical and experimental data. The biaxial strain used was below 1%. [73] Another study also found similar changes: -5.2 and -1.7 $\text{cm}^{-1}/\%$ strain for E_{2g}^1 and A_{1g} modes. [71]

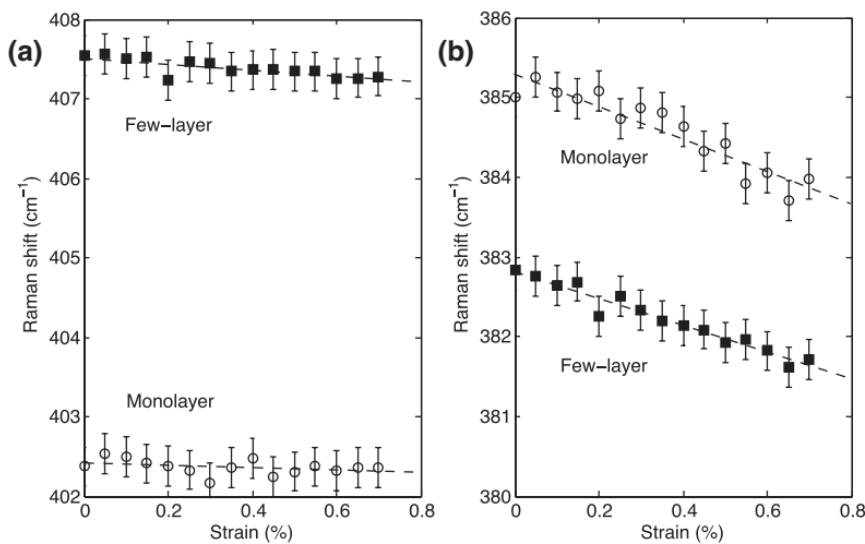


Figure 21: The peak positions of (a) A_{1g} mode and (b) E_{2g}^1 mode under uniaxial strain. Reprinted from [63]

3.1.3.3 Doping effect

Doping on MoS₂ film could be introduced due to chemical residues created during the transfer process, charge transfer from the substrate or defects on the film. [75] The dominant type of defect, especially in exfoliated MoS₂, is S-based defects and mainly sulfur vacancies which generate n-type doping. [76]

Doping mainly affects the A_{1g} mode while E_{2g}^1 mode is less sensitive. A softening / stiffening of the A_{1g} mode has been observed in many studies, and was attributed to increased / decreased electron density. [65]–[67], [77], [78] Using theoretical analysis, the strong dependence of A_{1g} phonon mode from doping is justified. The theory is presented in reference [77].

Other changes in spectrum such as the increase / decrease of the intensity ratio of the two modes ($I_{A_{1g}}/I_{E_{2g}^1}$) with p / n - doping and the broadening of the A_{1g} mode with n-doping have also been noted. [67], [77], [79] The broadening of the mode is also explained by the theoretical arguments referred above, as phonon linewidth arises from the contribution of electron-phonon coupling and non-linear effects. So, higher electron-phonon coupling resulting from doping leads to an increase of the FWHM as well. [77]

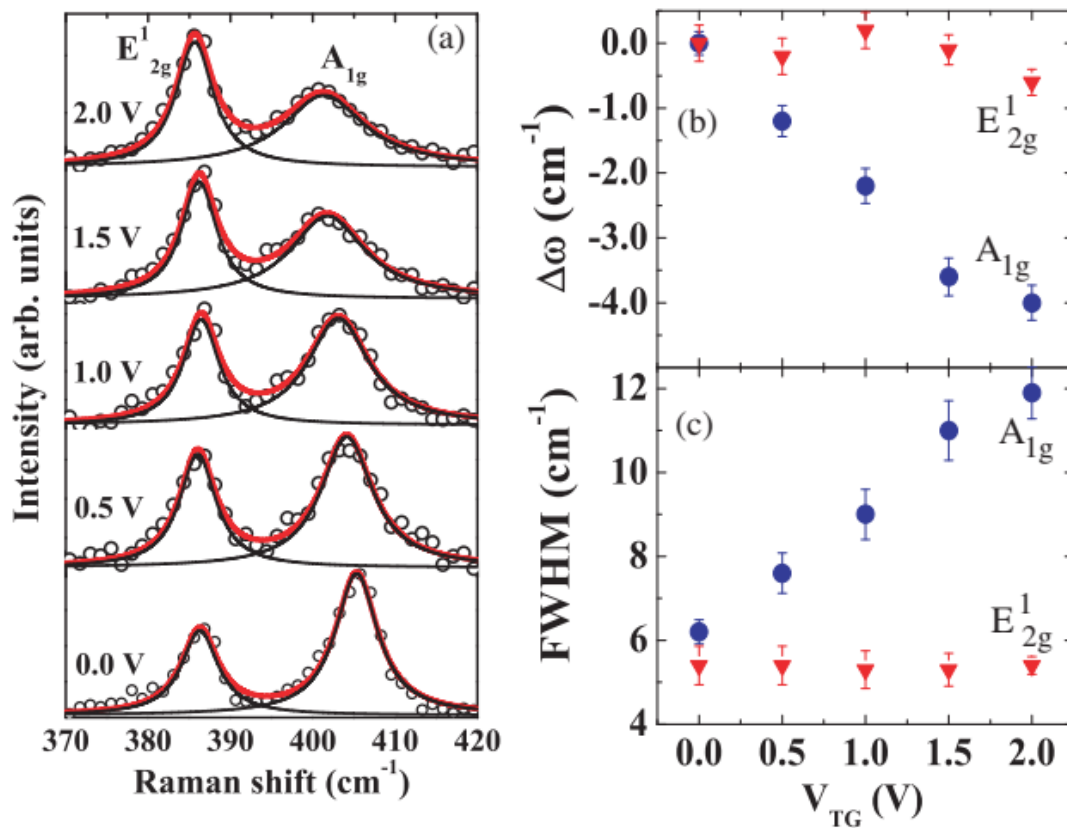


Figure 22: a) Raman spectrum b) mode shift and c) FWHM evolution with different top gate voltages (and consequently with doping). Reprinted from [77]

3.1.3.4 Effect of the defect density

The FWHM of E_{2g}^1 Raman mode has been reported to be an indication of the crystalline quality. The lower the width of the mode, the higher the crystal quality i.e. lower lattice imperfections. [80]–[82]

One of the most prominent type of defects in monolayer MoS_2 is Sulfur vacancies. So, special attention should be given to their behavior. Parkin et al studied their effect on the Raman spectrum. A sulfur vacancy is actually the removal of an atom from the system which weakens the restoring force constant k of the phonon mode and also reduces the total mass of the system. Considering the relationship for a simple harmonic oscillator: $\omega = \sqrt{\frac{k}{m}}$, the frequency of the modes can be either increased or decreased. Based both on DFT analysis and experimental results, they concluded that the S-vacancies cause a redshift of E_{2g}^1 mode and a very slight blueshift of A_{1g} mode. [83] However, someone could wonder if their experimental results are also influenced from the n-doping that is caused by the creation of S-vacancies and how they managed to reject this effect.

The effect of interference and the use of different substrates will be presented later (3.2.3.4, 3.2.3.6) in combination with their effect in photoluminescence spectrum.

3.2 Photo-luminescence

Photoluminescence is a spectroscopic technique that provides information about the electronic structure of the materials. Studying the characteristics of its spectrum, the frequency, intensity, FWHM, and shape of the peak, can help to investigate the recombination mechanisms, to identify the composition of the material, the optical bandgap of a semiconductor, the presence of defects, the crystalline quality of the material etc. [84]–[87]

3.2.1 Theoretical background

When a material absorbs a photon of sufficient energy after irradiation with light, an electron moves into a permissible excited state. More specifically, in semiconductor systems, the electron is excited from the valence to the conduction band leaving a hole behind it. The energy of the incident photon must be higher than the bandgap. Then, the photoexcited carriers, which are electrons and holes, will relax toward their respective band edges and will finally recombine causing the release of energy either by a radiative process (emission of a photon) or by non radiative processes (through multiple phonons or other recombination paths). Photoluminescence is referred to the first case, i.e. it is the emission of a photon coming from the radiative recombination of the photoexcited carriers. The energy of the emitted photon is the energy difference between the excited and ground state and is characteristic of the material. The

photoluminescence includes two categories: fluorescence and phosphorescence. Phosphorescence is a much rarer and slower radiative process because it involves intersystem crossing into a state with a different spin multiplicity. An important characteristic of photoluminescence is the Quantum Yield which is the ratio of the emitted photons/absorbed photons and is related to the contribution of radiative and non-radiative processes. [84]–[88]

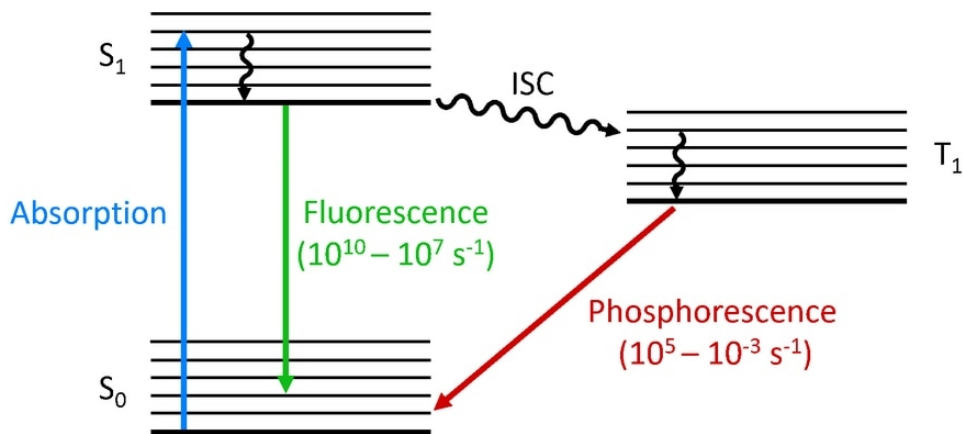


Figure 23: The energy diagram of fluorescence and phosphorescence process. Reprinted from [89]

3.2.2 Photo-luminescence Experimental set-up

In this thesis we used two different set-ups for the PL measurements. Initially, photoluminescence was recorded using the standard Raman set-up (Thermo scientific Nicolet Almega XR). The incident power was $300\mu\text{W}$, the spot size $\sim 1\mu\text{m}$ and the Raman (Pump) laser wavelength 473nm . Despite the advantages of this system (equipped with optical microscope, automation), it offered limited choices as far as the pump power and could only be used for room temperature measurements.

So, a bespoke photoluminescence set-up was designed. That setup is presented in figure 24. The laser source used was an optically pumped semiconductor laser (Verdi, 532nm). For time-resolved measurements a Ti-Saph tunable pulsed laser (Mira) tuned at 800nm was used. The laser pulses were then frequency-doubled with a BBO crystal. The incident power was controlled by a neutral density filter and the laser's beam diameter was approximately $7\mu\text{m}$. The resulting fluence was typically orders of magnitude lower in the bespoke set-up compared to the Raman system.

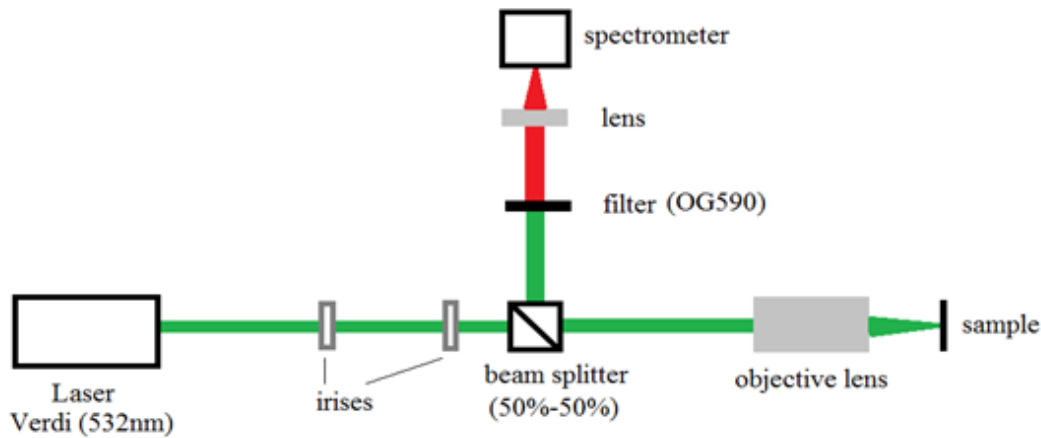


Figure 24: A simple schematic of the developed PL set-up.

3.2.3 PL on 2D MoS₂

The transition of the MoS₂ from an indirect bandgap semiconductor, in its bulk form, to a direct bandgap semiconductor, in its monolayer form, induces big changes in emission properties. Earlier research has shown that the PL signal increases drastically as we move down to the monolayer sample. [90] In most studies, two peaks seem to be related to MoS₂ emission and have been attributed to excitonic and trion emissions. The first peak, which is around 1.8 - 1.9 eV and is the prominent one at room temperature, arises from the contribution of A exciton and negative trion as their peaks often overlap. (At room temperature) The extra peak comes from the emission of B exciton and is found around 1.95 - 2.05 eV. [8], [82], [90]–[94] These limits are just an indication of the position of the peaks as every study presents different results because the spectral characteristics are strongly influenced by many parameters such as temperature, excitation wavelength and density, substrate used, method of growth and many others. [18], [92], [95], [96] Below, we will present some of the parameters that affect the PL spectrum and the changes they cause as they have been mentioned in literature.

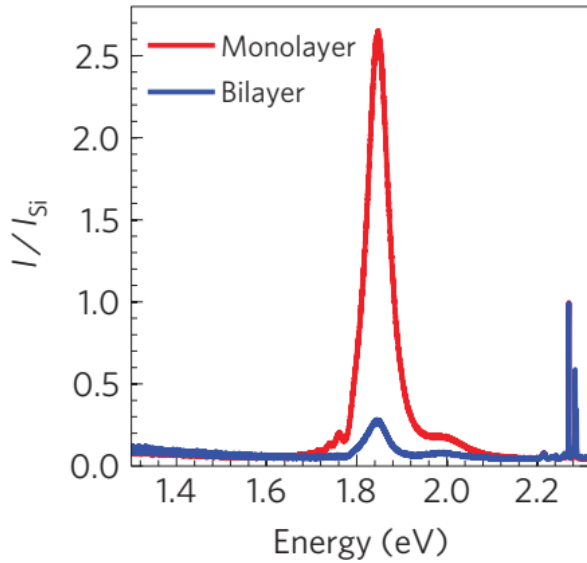


Figure 25: The PL spectrum of monolayer and bilayer MoS₂. The intensity of the PL is drastically lower in samples with higher number of layers. Reprinted from [93]

3.2.3.1 Strain effect

The application of strain influences the electronic and optical properties of MoS₂ and consequently the monolayer photoluminescence emission. It has been reported that the strain causes bandgap deformation while the change induced in exciton binding energies is less significant and can be neglected. [69], [97] A qualitative way to explain the effect is to think that the strain weakens the bonds between the atoms and so a reduction of the optical overlap and hybridization is caused. It is also possible, that the strain causes the reduction of carrier effective masses. [97] The change in bandgap results in the appearance of a redshift at the excitonic emission peaks. [68], [75], [97] The amount of the shift found seems to have an approximately linear dependence on strain but varies based on different studies:

1. 64 ± 5 meV/% strain for A exciton and 68 ± 5 meV/% strain for B exciton determined experimentally [97]
2. 45 ± 7 meV/% strain for A exciton peak based on experimental results and 59 meV/% strain based on GW0-BSE calculation [70]
3. 48 meV/% strain for A exciton peak determined experimentally and 42 meV/% from DFT calculations [68]

Because of the progressive transition of the bandgap from direct to indirect with application of strain (the indirect bandgap decreases more rapidly than direct), the intensity of the PL decreases. [68], [70] Furthermore, as indirect transitions ($\Gamma \leftrightarrow K^{\pm}$) become more important, the polarization degree also decreases. [68]

On the other hand, applying biaxial strain of about 10% does not simply reduce the bandgaps (direct and indirect) but leads to a semiconductor to metal transition, as has been reported theoretically. [98]–[100] In smaller biaxial strains, the shift of the PL peaks found by several studies is $-(90-100)$ meV/% tensile strain (-99 ± 6 meV/% strain in [71], approximately -90 meV/% strain in [74] and about -100 meV/% strain in [72]). Lloyd also noted that the shift rate was similar between exfoliated and CVD grown samples and for all three peaks. [71]

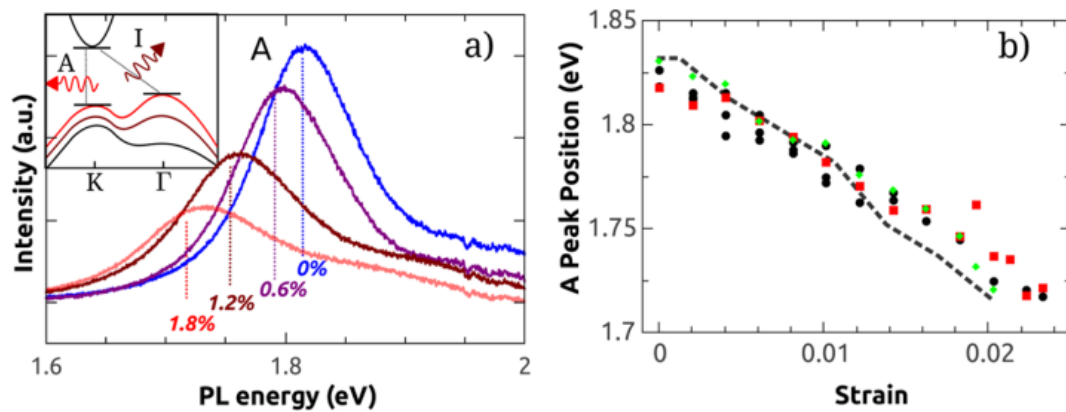


Figure 26: The PL a) spectra and b) A peak position evolution with uniaxial strain. Reprinted from [70]

3.2.3.2 Doping effect

Extensive research has been conducted to study the results of doping on the intrinsically electron doped mono-MoS₂. Based on the type of doping, the n type decreases the PL intensity due to a reduction of Quantum Yield, the peak position is redshifted and the FWHM increases. Conversely for p-type doping the opposite effects are observed as discussed in numerous publications [8], [54], [66], [67], [94], [101], [102] The reason for these changes is related to the natively n-type character of MoS₂. [94], [101], [103] P-dopants electronically deplete its surface while n-dopants create accumulation. The presence of excess electrons enhances the electrostatic screening between free e⁻ and h⁺ which destabilizes the bound states (excitons / negative trions). As the formation of excitons / trions is suppressed, the non radiative recombination of photoexcited electrons and holes dominates and so the PL quenching can be explained. On the other hand, the extra electrons help the formation of trions instead of excitons as they provide the second electron needed. So, the relative population of excitons/trions decreases and the peak redshifts. The opposite behavior is observed with p-doping. [101] Auger recombination is also enhanced with n-doping which enhances the role of non radiative decay processes and gives an extra explanation of the behavior observed. [22] Finally, Mak and coworkers [94] further noted that the exciton and trion energy splitting is linearly dependent from the Fermi energy and consequently the doping density. Qualitatively, the explanation for this behavior is that the exciton results from the dissociation of a trion and the extra electron will be

placed at the fermi level (under the conditions of zero temperature and finite doping densities).

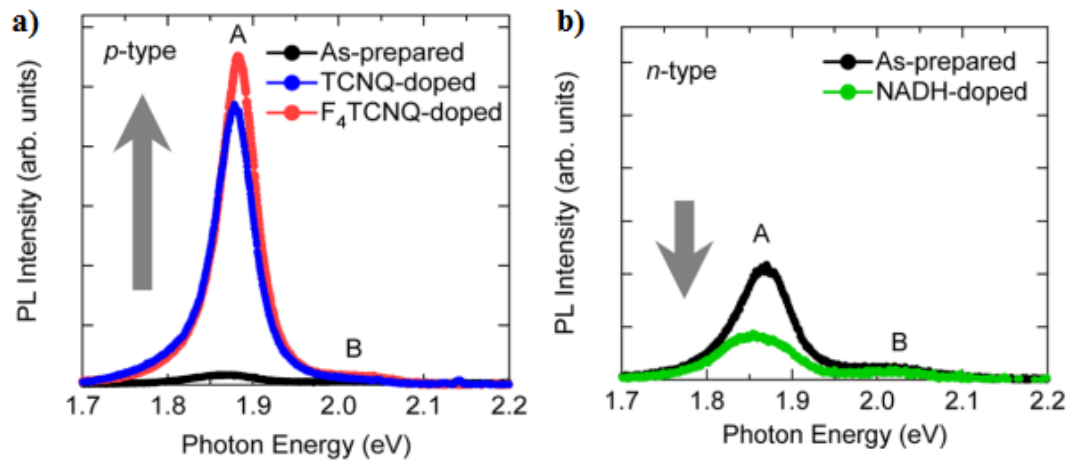


Figure 27: Comparison of photoluminescence spectra between as-grown samples and a) p-doped, b) n-doped samples. Reprinted from [102]

3.2.3.3 Dielectric environment

Lin et al [8] studied systematically the effect of the dielectric environment on PL characteristics and explained their results theoretically. The dielectric constants of substrate and top layer of our film influence the dielectric screened coulomb potential which affects the e-e, e-h interactions. So, the electronic band gap and the binding energies of excitons / trions reduce as the dielectric constants of the environment increase. Also, due to the dielectric screening effect, the higher the dielectric constants, the more confined the coulomb potential within the middle layer. This could reduce the scattering between the excitons/trions and the charged impurities at the interface and thus prolong their lifetime. As a consequence of these effects, the exciton/trion peaks blueshift (in a small rate), their intensities increase and their FWHM decrease as a function of dielectric constant. Finally, the ratio of trion / exciton emission intensity decreases as well.

3.2.3.4 Interference effect

The substrate induced optical interference influences the absorption of the excitation light, Raman and PL intensity.[66], [75], [104] The light is partially reflected and refracted in every interface (upper layer-usually air/ MoS₂ layer/oxide in substrate, oxide / substrate) which can lead to constructive or destructive interference depending on the excitation wavelength, the refractive indices and the thickness of the different layers. So, depending on these parameters the intensity of PL and Raman spectra could be enhanced or suppressed respectively. The effect (enhancement or

suppression) is not constant with respect to wavelength. However, the peak positions of the spectra seem to be unperturbed by this effect. [66], [104]

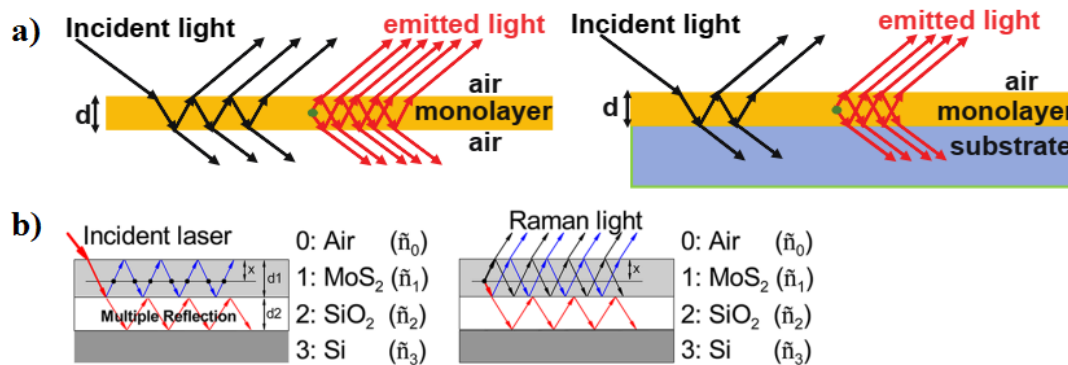


Figure 28: Schematic diagrams for the optical interference of incident and emitted light for a) a suspended and a supported film. Reprinted from supplementary of [103] b) a monolayer supported by a SiO₂/Si substrate. Reprinted from [104]

3.2.3.5 Defect density

It has been reported that the intensity ratio of B/A exciton is associated with the quality of the material. More specifically, when the ratio is low, the non-radiative defect density on the material is also low and consequently the quality is high. This behavior has been explained with the following rationale: The B exciton has an additional available pathway: scattering towards the lower A-band energy. So the B-exciton lifetime is smaller than the A-exciton lifetime. Defect states provide extra non-radiative pathways but affect mainly A exciton while B exciton remains almost unaffected as the induced change in its lifetime is smaller due to the very quick intraband relaxation. [82]

3.2.3.6 Substrate

The type of substrate used has a complex impact on spectral characteristics and is mainly related to the effects mentioned above. First of all, it affects doping. Doping could be caused by charge transfer from the substrate to the film or from the presence of charged impurities at the substrate/film interface. [66], [75], [103] Furthermore, as referred previously, the optical interference is dependent on material type (refractive index) and thickness. [59], [66], [75] The dielectric constant of the substrate further influences the PL characteristics as explained in 3.2.3.4. Finally, non-radiative recombination via the substrate could occur and affect the PL emission. [75], [103]

3.3 MoS₂ CVD growth

The samples were grown using the CVD method. S (14 mgr) and MoO₃ (120 mgr) powder were used as precursors. The targeted substrate was placed behind the MoO₃ boat whose temperature reached up to 700°C during growth (the maximum temperature of S boat was 450°C). The inert carrier gas that was used during growth is Argon with a flow of 20 sccm.

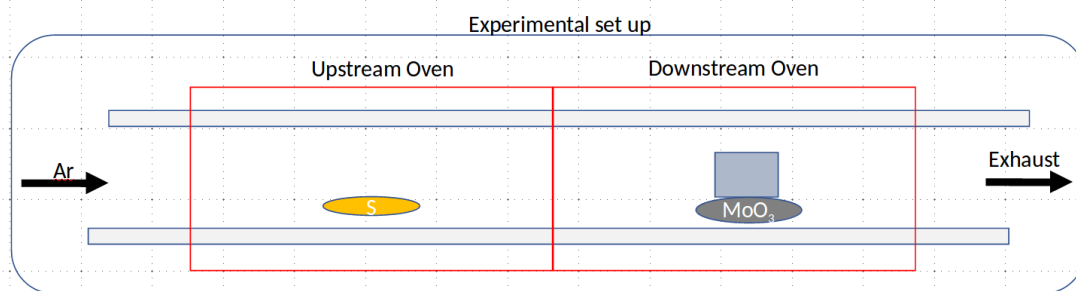


Figure 29: Schematic of the quartz oven arrangement used to perform CVD growth of MoS₂.

3.4 2D material transfer

After CVD growth, the as-grown monolayer MoS₂ can be transferred to an arbitrary substrate using PMMA-mediated transfer. PMMA A11 was spin-coated onto the surface of the sample at 3krpm for 45sec and was left to dry at room temperature overnight to avoid thermal stresses. The PMMA surface was scratched around the 2D sample in order to allow the acid to attack the SiO₂ substrate. Then, the sample was immersed in a diluted hydrofluoric acid (1:6) to etch the oxide (SiO₂). After the PMMA-assisted MoS₂ film was released from the substrate, it was scooped-out using a clean Si wafer and was immersed in deionized water. This process was repeated several times (at least three) to remove any contamination from the etching solution. The final scoop was performed using the target substrate. Following placement of the PMMA membrane with the MoS₂ on the target substrate, a lint free paper was placed on top and pressed onto the surface. This removed excess water from the sides of the membrane and improved adhesion. To completely dry the membrane, the sample was placed in a vacuum hotplate at 20°C for 30 min, after pumping down, the temperature was increased gradually to 60°C and was kept constant for an hour to allow any water trapped below the membrane to gradually evaporate. Finally, the sample was left to cool down gradually to room temperature and then the chamber was vented to ambient pressure. The removal of PMMA layer was accomplished by placing the sample in an acetone vapor chamber that was being heated to increase the acetone deposition on the sample. After dissolution of the PMMA in acetone bath, the sample was rinsed with isopropyl alcohol and was dried by gently blowing nitrogen.

3.5 MoS₂ surface treatment

3.5.1 TFSI treatment

Bis(trifluoromethane)sulfonimide (TFSI) is a strong protonating agent and is reported in [18] to have a strong effect in Luminescence efficiency. The recipe used is similar to the one described in the original paper and is described here for completeness:

Samples were initially annealed in a vacuum hotplate at 100°C or in forming gas at a temperature of 300°C for 5 minutes. 20mg of TFSI were initially dissolved in 10 mL of 1,2 Dichloroethane (DCE). Subsequently, 90mL of 1,2 dichlorobenzene (DCB) were added to obtain a final solution concentration of 0.2mg/mL. The sample was immersed in the solution at 50°C for 10 min and was subsequently dried using N₂. Finally, the samples were annealed at 100°C for 5 minutes in air.

4 Results and discussion

4.1 CVD grown samples

In order to systematically evaluate the quality of each MoS₂ sample produced, we used a series of techniques. The results are presented in the following paragraphs.

4.1.1 Optical microscopy

In order to test the quality of the MoS₂ monolayer produced by CVD method, we used an optical microscope to observe crystal size and 2D layer uniformity. Below, we present 3 characteristic pictures of our sample that show all the different regions.

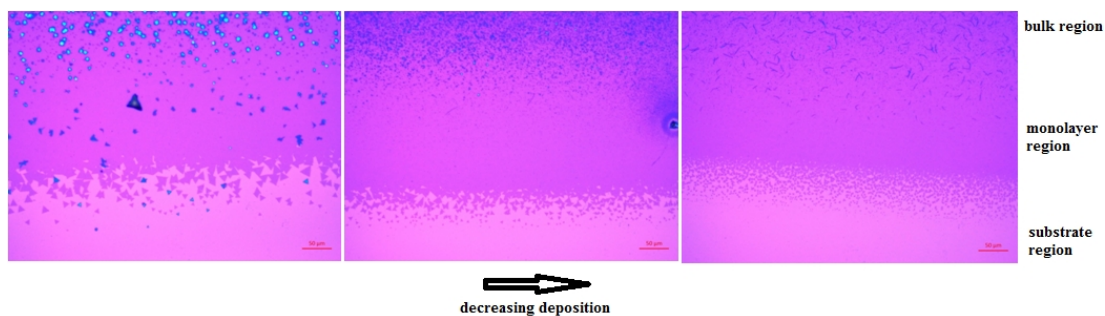


Figure 30: Optical pictures of the sample. In the left picture, bulk spots can be identified in the monolayer region while moving towards the right we observe that the deposition is decreasing (less bulk spots, smaller monolayer triangles, the monolayer tends to become non-continuous).

Moving from the bottom to the top of a typical CVD grown sample we can distinguish 3 regions:

- a region where there is no deposition of MoS₂, only the SiO₂/Si substrate appears
- a monolayer band, about 200µm wide. Between the two regions, there is a narrow area where the deposition is not continuous but consists of small crystallites of triangular shape.
- Above the monolayer, the deposition is higher and the area consists of 2 or more layers of MoS₂ and eventually 3D structures are observed.

There is non uniformity left – right within the monolayer region. The amount of material is apparently decreasing as we move to the right, there are some bulk spots in the left side while in the right edge the monolayer becomes non-continuous and there are small gaps between the monolayer regions. This effect is probably caused by the way that the sample is placed in the CVD chamber: the left edge is closer to the Sulfur boat and so the deposition takes place in S-rich conditions compared to the right edge.

4.1.2 Raman spectrum

The Raman spectra of the samples used were taken and analysed to estimate layer number, stress and other characteristics of the grown material. The samples were irradiated with a fluence of 10^4 Wcm^{-2} at room temperature and in normal atmospheric pressure. The laser used was at 473nm wavelength. The same parameters were used for all Raman measurements that were taken in this thesis.

For each sample, multiple sites along the monolayer region were measured so as to validate the uniformity of the samples used in the study. The measurements were carried out in a specific direction: from the left edge towards the right edge as we defined them in the previous paragraph (from S-rich to S-poor conditions). This principle was kept for all samples and all measurements (PL and Raman).

We are going to focus on the behavior of the two dominant peaks that we observe in the Raman spectrum of a monolayer MoS_2 : the first order E_{2g}^1 and A_{1g} modes. Below, we present the full range of a Raman spectrum and a detailed plot of the important modes. All peaks are fitted using a pseudoVoigt profile.

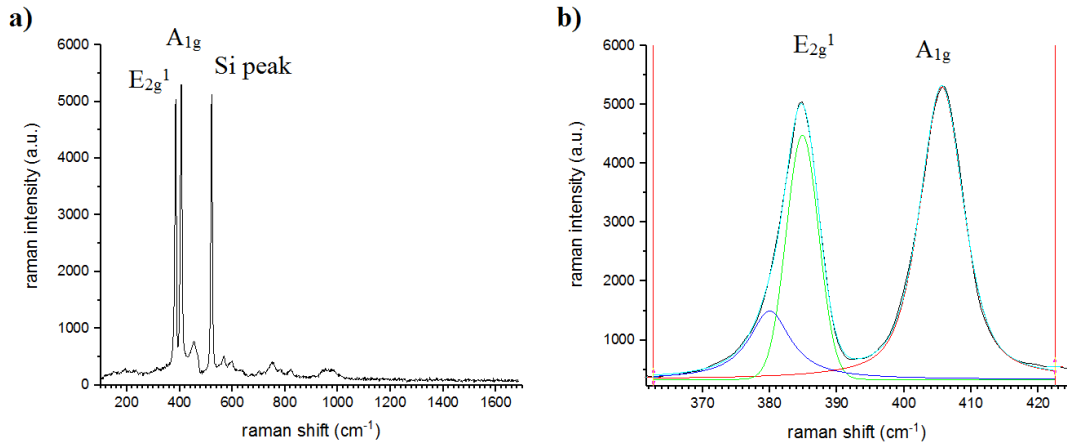


Figure 31: a) Typical Raman spectrum of a monolayer MoS_2 and b) the two dominant peaks in a higher magnification. An extra peak has to be added in the fitting that will be explained in the main text.

In the diagram, except the E_{2g}^1 and A_{1g} modes we can also identify one more dominant peak around 520cm^{-1} which arises from the Si substrate (Si LO phonon mode). To properly fit the acquired data, we need to add one more peak (around 380 cm^{-1}) which overlaps with E_{2g}^1 and is related to disorder according to literature. [105] We could also attribute it to the unresolved splitting of the two subbands E_{2g}^{1+} , E_{2g}^{1-} which could be caused by strain but then we would expect the mode to become degenerate again after transfer, when strain is released, which is not the case here as we will present later (see 3.1.3.2, 4.2.1.2).

In order to prove the monolayer nature of the material deposited, we calculated the spacing between the two modes. The spacing varied from 19.7 to 21.2 cm^{-1} across

sites and various samples. The variations could be attributed to different strain, doping and other parameters as we have discussed in detail in Section 3.1.3.

As mentioned in that section (3.1.3), changes in the characteristics of the modes can offer information about the material. From the fitting of the peaks, we are able to find the FWHM, peak positions and mode spacing.

Most of the samples present a shift to higher energies of the A_{1g} mode by $0.2\text{-}1.4\text{cm}^{-1}$. This could possibly be attributed to reduced electron density (see 3.1.3.3). However, this observation does not seem to be accompanied by a narrowing of the mode. The hypothesis will be also checked by the analysis of the PL spectrum. The peak position and FWHM of the E_{2g}^1 mode do not seem to follow a trend in the majority of the samples. Nevertheless, in some samples a stiffening of the mode is observed, similarly to the case of A_{1g} mode. Below, we present two diagrams. The first diagram presents the characteristics of a sample whose modes shift as we move along the monolayer region while the second diagram is related to a sample where no trend is observed.

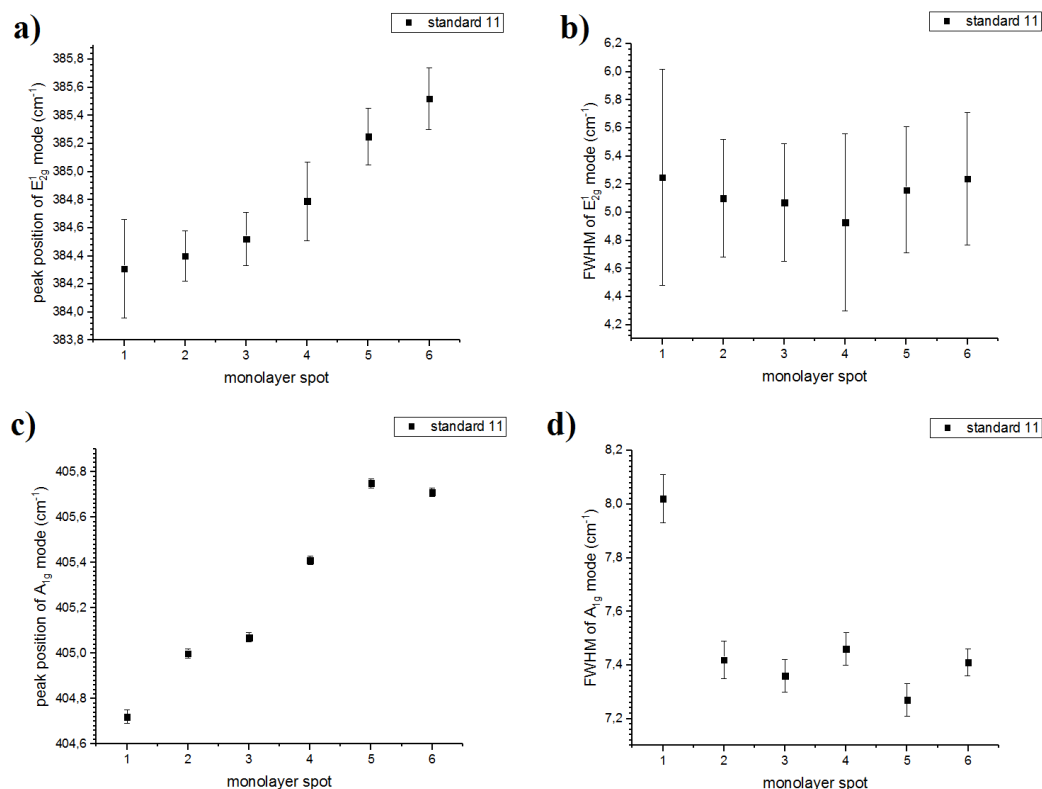


Figure 32: Peak analysis of the sample “standard 11”: a) peak position and b) FWHM evolution of the E_{2g}^1 mode and c) peak position and d) FWHM evolution of the A_{1g} mode.

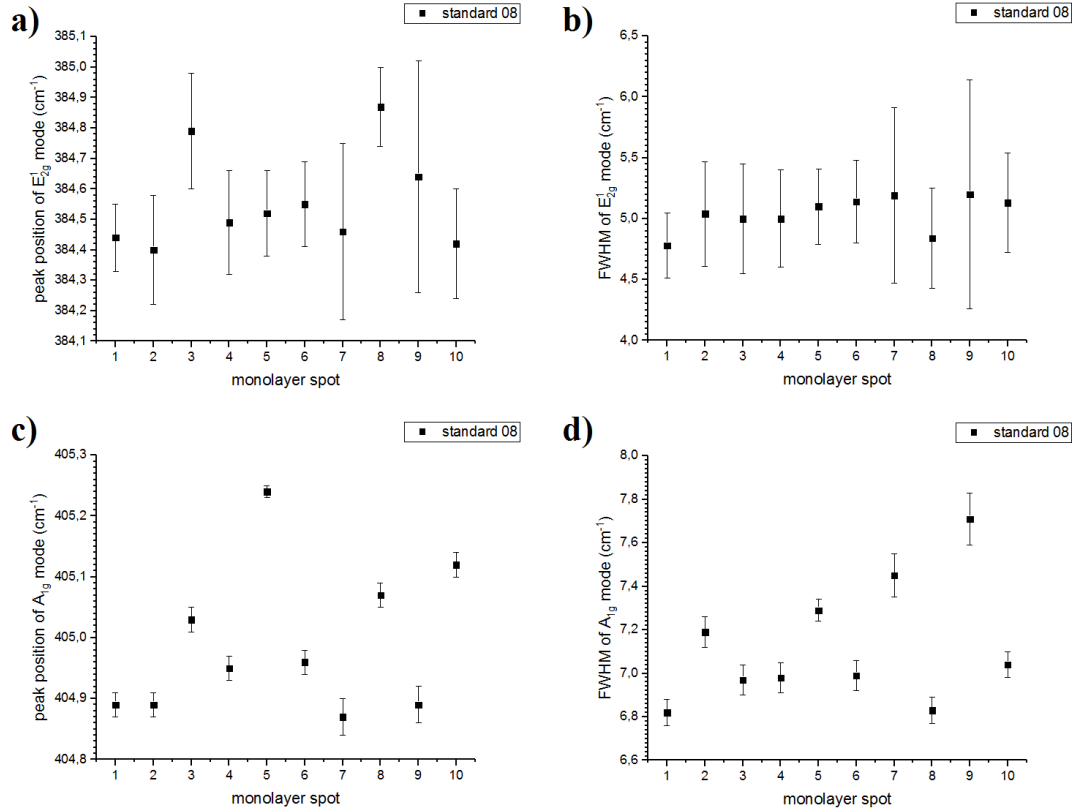


Figure 33: Peak analysis of the sample “standard 08”: a) peak position and b) FWHM evolution of the E_{2g}^1 mode and c) peak position and d) FWHM evolution of the A_{1g} mode.

Despite the fact that we tracked small changes when we compared different spots, we are not able to make general conclusions: The variations are different for each sample and the characteristics do not lead to a consistent response.

4.1.3 Photoluminescence spectrum

The Photoluminescence spectrum was also used to evaluate the quality of the material and especially its optical properties. The Raman set-up was also used to collect PL spectra and all parameters of the experiment were kept unchanged to have comparable measurements.

The spectrum of a MoS_2 monolayer consists of 3 peaks: the B-exciton peak and the overlapping A-exciton and trion peaks. However, as we observe in figure 34, B-exciton and trion peaks are not easily tracked in the spectrum of as-grown samples because of the A-exciton’s high intensity. The B-exciton peak slightly appears compared to A-exciton. Also, the main peak can be fitted quite well with one peak so we conclude that the trion contribution must be negligible in our data. The fitting curve used is a pseudovoigt. The oscillations that appear in the right side of the peak are not part of the MoS_2 emission but they possibly are interference fringes.

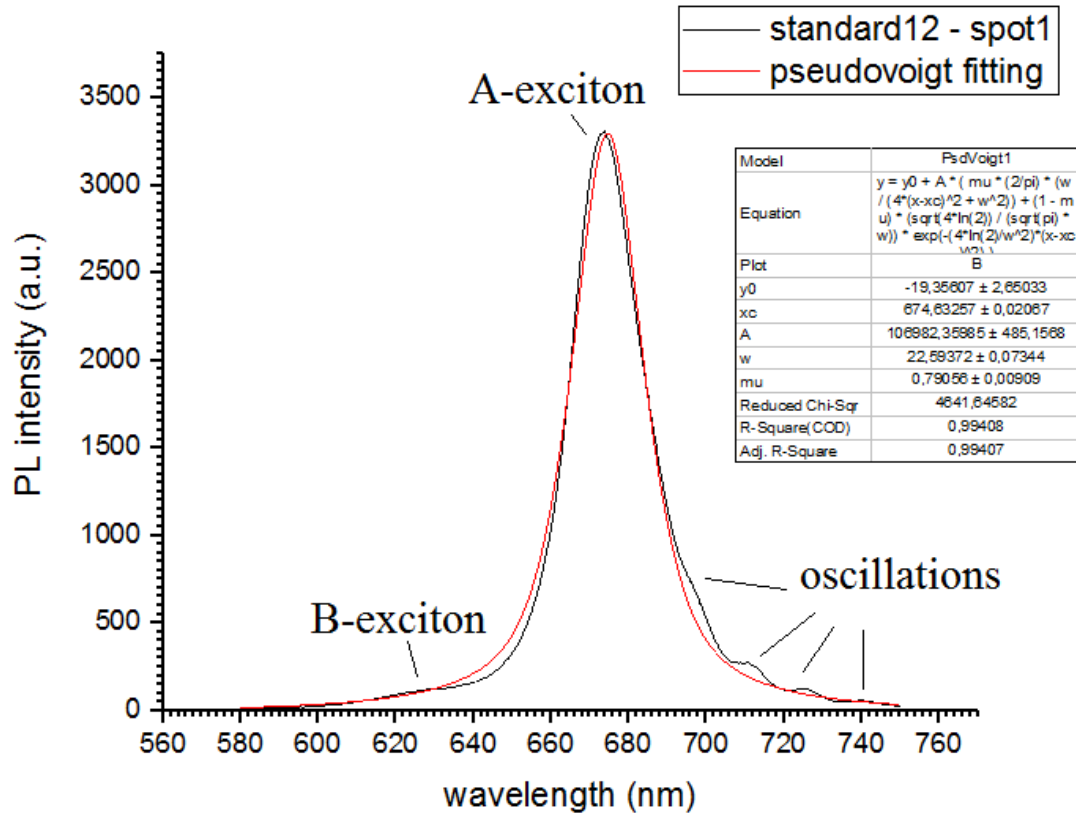


Figure 34: PL spectrum of an as-grown monolayer MoS₂. The red line is the pseudovoigt fitting of the main peak.

From the comparison of the different spots, we find that there is a clear blueshift of the peak as we move towards the right edge of the sample. This behavior was observed in all samples but the shift varied in magnitude (3.5-10 nm) between different samples.

This could further support the hypothesis that n-doping is reduced on the right edge (the relative ratio of A-exciton/trion is increased). However, the other characteristics of the PL do not confirm that assumption. We would expect the FWHM to decrease (because the FWHM of the trion is higher than that of the A-exciton's [102]) and the PL emission (and as a consequence the integrated intensity) to be enhanced as well.

In some samples the integrated intensity was enhanced indeed while in others it had a decreasing trend in the left spots and an increasing trend in the right ones. However, we can not rely on that characteristic. The intensity is strongly influenced by the focus which varies across measurement leading to variations in the PL intensity. Sample defect density could also influence the intensity.

The evolution of FWHM further disputes our initial hypothesis. In most of the samples the variations are small (~2nm) and they do not change in a systematic way.

Strain variations could also account for the PL blueshift but then variations in E_{2g}^1 mode of the Raman spectrum would shift accordingly which is not observed.

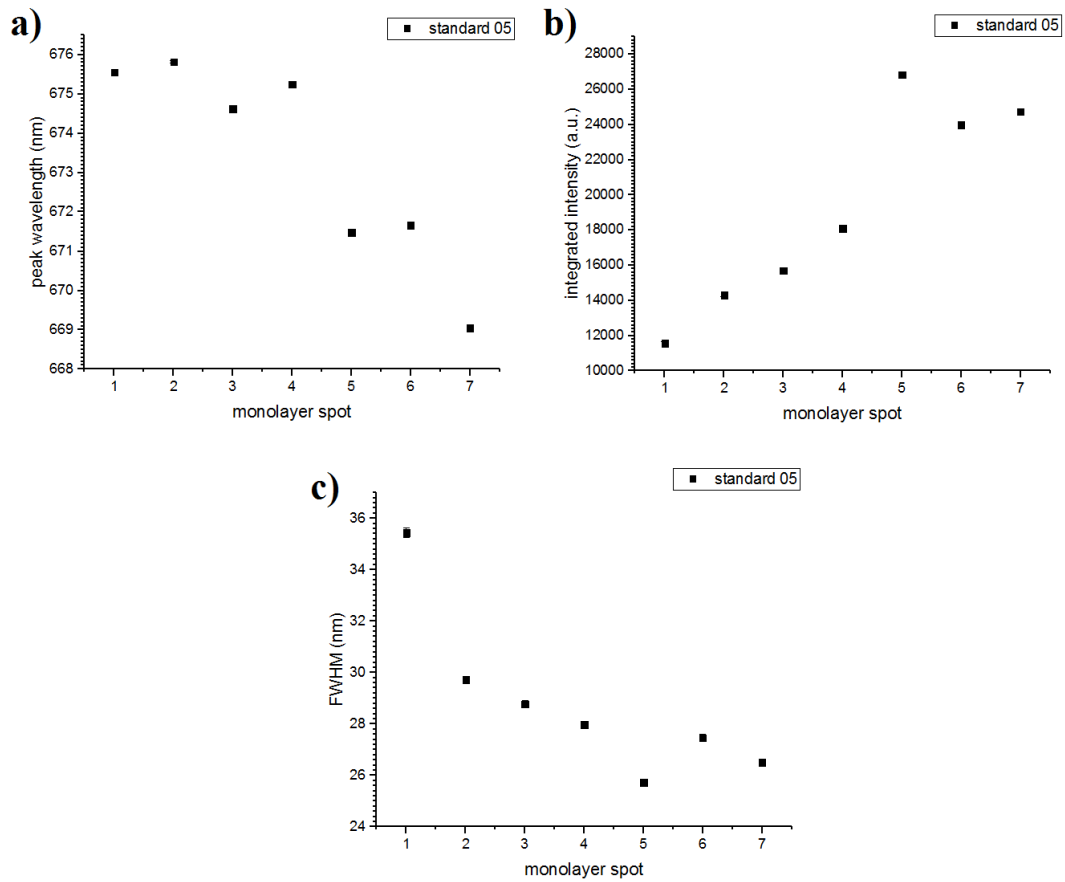


Figure 35: PL a) peak wavelength b) integrated intensity and c) FWHM of the sample "standard 05". The evolution of all characteristics are consistent with the reduction of electron density.

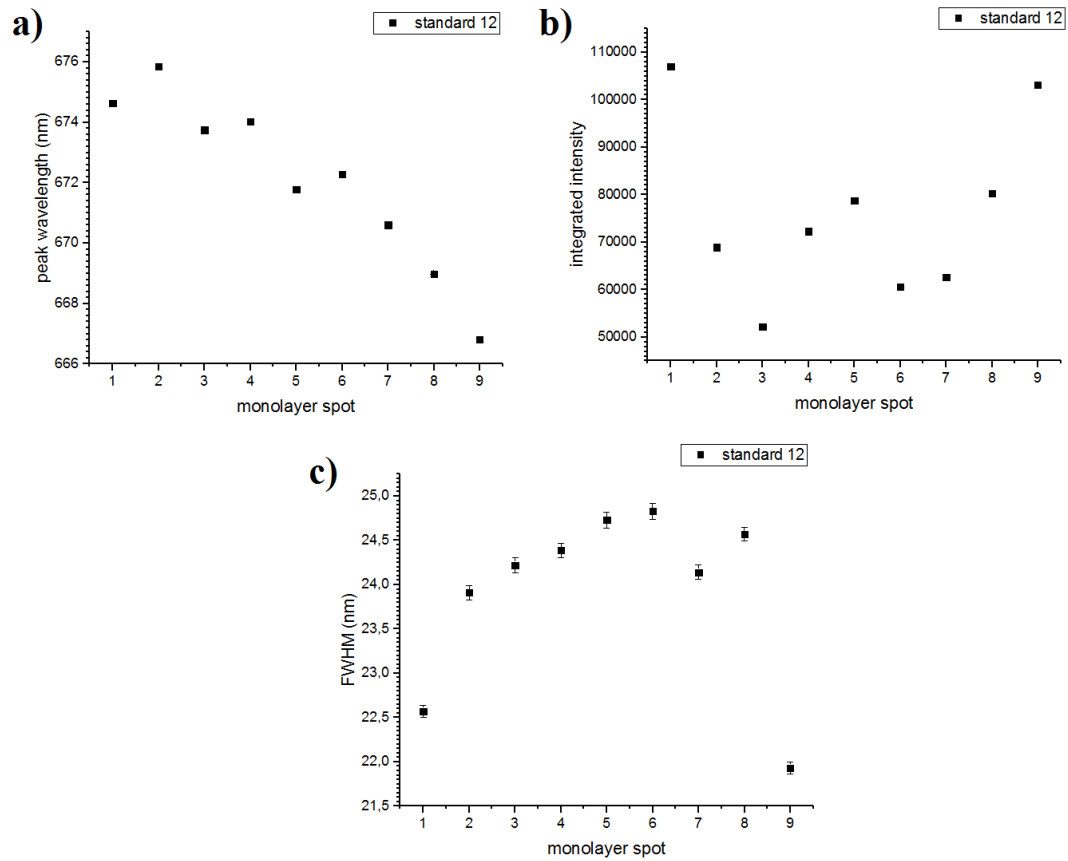


Figure 36: PL a) peak wavelength b) integrated intensity and c) FWHM of the sample "standard 12". The peak wavelength is blueshifting almost monotonically but the other characteristics present a more complicated behavior.

Temperature evolution of PL spectrum

The evolution of PL emission as a function of temperature was studied. The fluence of the laser beam (Verdi, 532nm) was 450 Wcm^{-2} and the sample was placed in a vacuum chamber. The pressure inside the chamber was 10^{-4} mbar. We varied the temperature from 11-295K with a step of 25K starting from the low temperature. The recorded spectra are presented in figure 37.

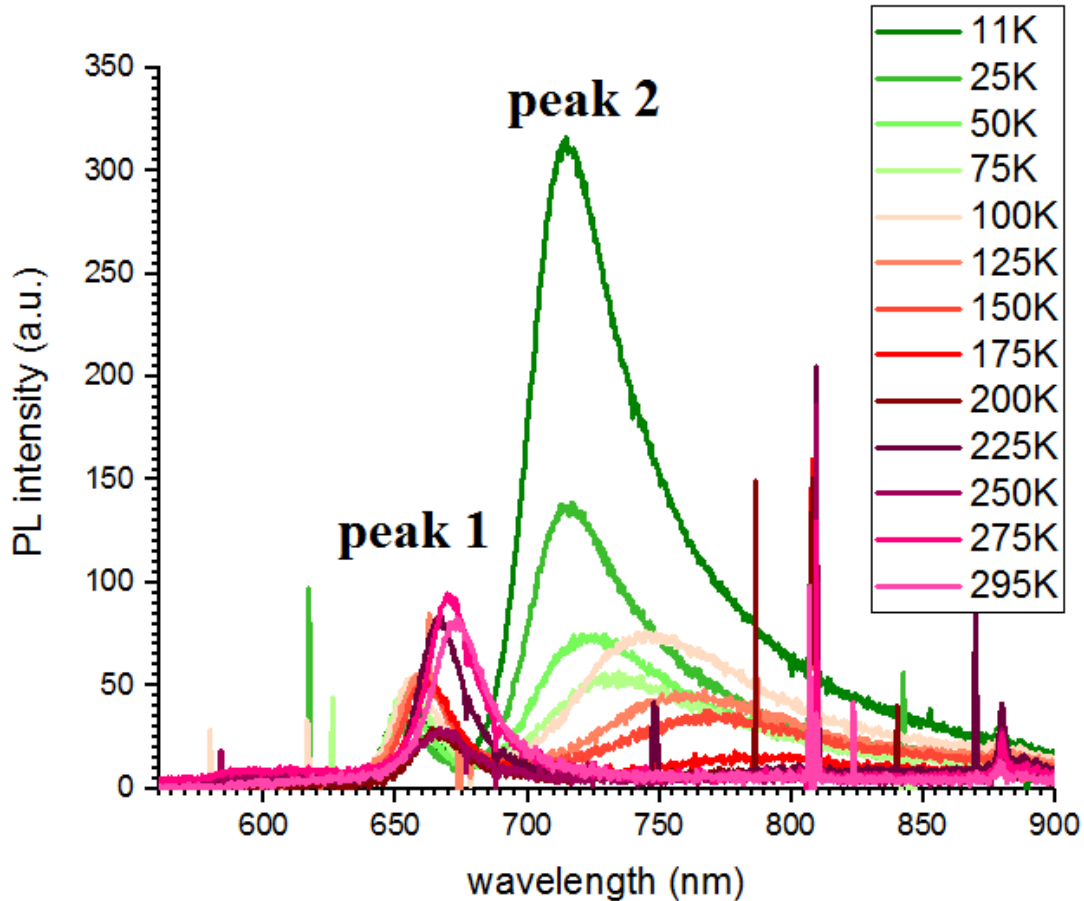


Figure 37: Evolution of a PL spectrum with temperature. As temperature drops the peaks blueshift and their relative intensity changes. The used fluence is 450Wcm^{-2} .

The fitting of the peaks was tested with 2, 3 and 4 peaks and different functions (Pseudovoigt, Lorentzian and Gaussian) but the recorded spectra appear to have a complicated response. To avoid unjustified assumptions we decided to calculate some of the characteristics of the peaks without using a specific fitting function.

Firstly, we will make some qualitative analysis of our findings. As temperature gradually decreases, the peak that was originally arising at $\sim 670\text{nm}$ (peak 1) blueshifts and reaches $\sim 650\text{nm}$ at cryogenic temperatures (11K). When the temperature reaches approximately 200K an extra peak (peak 2) arises in the PL spectrum and finally becomes dominant in low temperatures (below 100K). This peak also blueshifts as temperature drops and the position of the maximum intensity moves from $\sim 780\text{nm}$ to $\sim 710\text{nm}$ as can be seen in figure 37. In the diagram, the maximum intensity of the “peak 1” seems to change with a non-monotonic way. The intensity is very sensitive to the focus and the site that is irradiated. A problem that occurred was that the sample’s position could not be kept steady, possibly because of the cryostat’s thermal expansion/contraction. The used approach to improve repeatability was to attempt to maximize the emission before every measurement by adjusting the spot’s position and focus. This translates to a slightly different measured area in every

measurement. Finally, the emission from peak 2 seems to be highly asymmetric at low temperatures while it tends to become more symmetric in higher temperatures.

The peak wavelengths of the spectrum are rather insensitive to focus and irradiated site. The evolution of central wavelength for the two peaks is plotted in figure 38. The energy difference between peak 1 and peak 2 is approximately 0.16 eV in 11K and reaches as much as 0.29 eV in 150-200 K before the high energy peak vanishes. This extra peak that appears in low temperatures (peak 2) has been previously reported in the literature and has been identified as bound exciton. [92], [106]–[108] Its formation has been correlated to the presence of defects and more specifically S-vacancies. [106]–[108] The binding energies that have been reported are 0.1eV [108] and 0.15-0.25 eV [106] which agree with our findings in this work (0.15-0.3 eV). Both peaks blueshift as temperature reduces. We attribute this change to the variation of energy gap and binding energies with temperature. If we neglect the variation of binding energies with temperature we can fit the changes with the well-known Varshni equation for the evolution of the bandgap energy: $E_g(T) = E_g(0) - aT^2/(b+T)$. The fitted functions seem to match the recorded data well. However, the parameters found for bound exciton are different from the ones of free exciton and this could arise from our approximation - the data do not represent the bandgap but the peak energies of the emission species. Also, the derived parameters for the free exciton ($E_0 = 1.899 \pm 0.002$ eV, $a = (2.8 \pm 0.6) \cdot 10^{-4}$ eV K⁻¹ and $b = 160 \pm 90$ K) do not seem to agree with the ones found by Korn. [96]

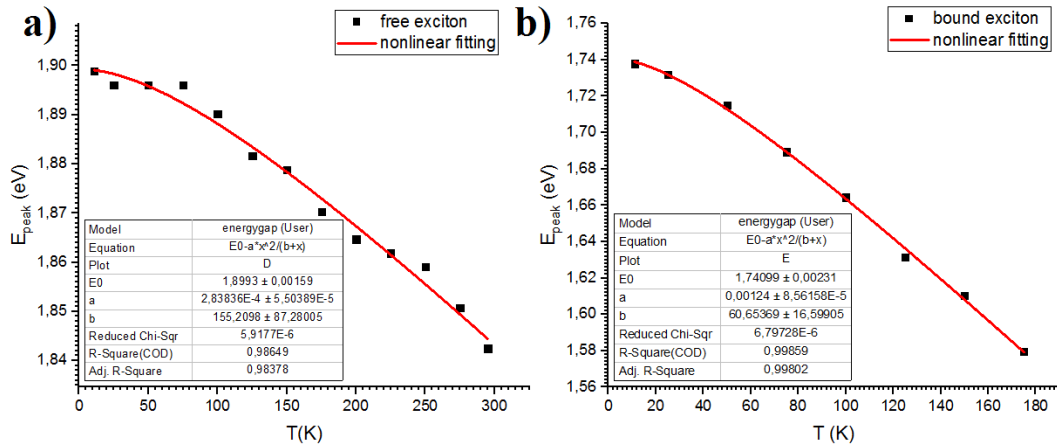


Figure 38: Evolution of the peak energies of a) free exciton and b) bound exciton with temperature. The used fluence is 450 Wcm^{-2} .

Power dependence at low temperature

In order to better understand the origin of the two peaks, we took a series of power dependent PL measurements in low temperature (11K). The pressure in the chamber was 10^{-4} mbar and the used fluences varied from 55 to 1700 Wcm^{-2} . We started measuring with a laser beam of 55 Wcm^{-2} and gradually reached 1700 Wcm^{-2} . Then,

we gradually decreased the power back to the lowest setting. The PL spectra for the “increasing power” case are presented below.

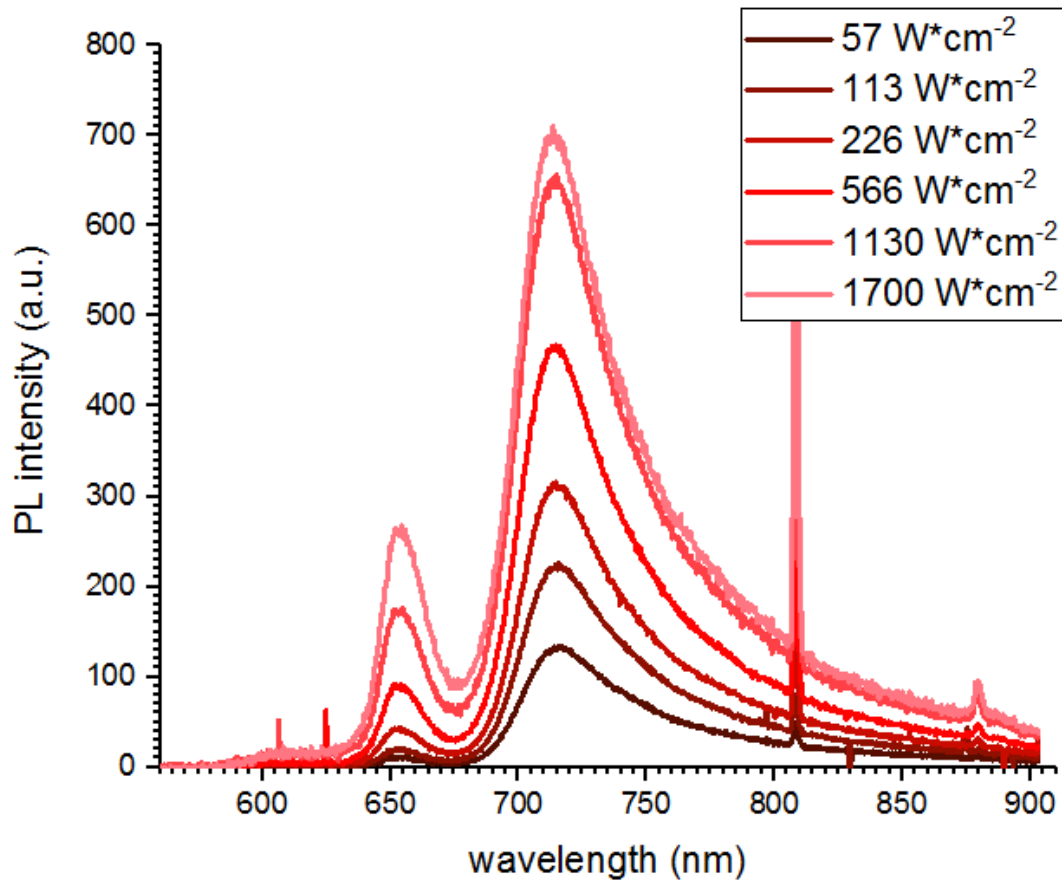


Figure 39: PL spectrum evolution with pump power at 11K.

To get a rough estimate of the integrated PL without resorting to elaborate fitting of the data, we assumed the two peaks are separated at 675nm and integrated the two regions separately. In figure 40, we present how the integrated intensities of the two peaks evolve. As we can observe in the following diagram the power dependence of peak 1 is approximately linear (slope in *b*) diagram ≈ 0.95 while that of bound exciton is sublinear (slope in *c*) diagram ≈ 0.5). This further justifies the hypothesis of bound excitons as bound excitons are expected to saturate at high power intensities when defects are fully populated with electrons. [106], [108] The free exciton’s integrated PL showed similar response in both the “increasing power” and decreasing power” case while not the same behavior was observed in bound exciton. The peak wavelength and linewidth do not change with pump power.

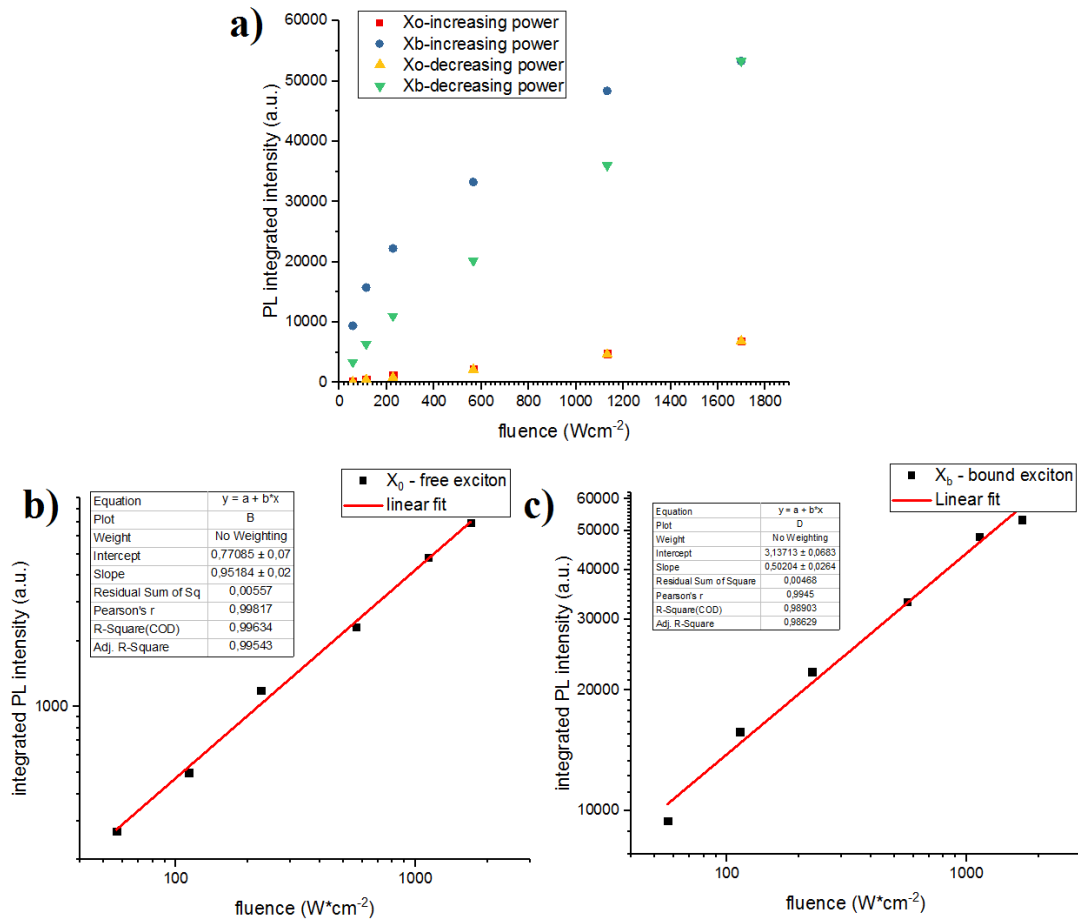


Figure 40: a) The integrated intensity of free (peak 1) and bound (peak 2) exciton versus fluence at 11K for both the “increasing power” and “decreasing power” cases. The linear fittings for b) free and c) bound exciton (the axis in b), c) are in logarithmic scale)

Despite all the indications that the extra peak is related to the emission of bound excitons, it is not well understood why this peak disappears at 200K. The thermal energy at this temperature is just 17.2 meV, far below the formation energy estimated from the wavelength distance (around 150 – 300 meV).

Pump power dependence in ambient air at room temperature

We further studied the behaviour of our material by taking power dependent measurements in air at room temperature. The laser used was Verdi (532nm) and the fluences ranged from 80-4000 Wcm⁻². We started irradiating the sample with low pump power and then increased to higher fluences. When we reached the highest fluence used, we started decreasing again until the minimum. We present the measured spectra for the two experiments in the following diagram.

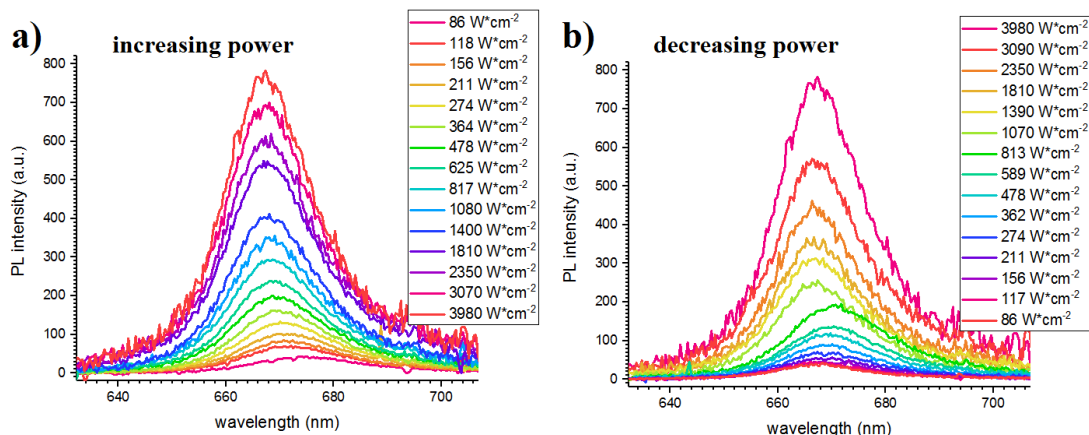


Figure 41: PL spectrum evolution with pump power when we move a) from low fluences to high and b) from high to low

From the analysis of the data we calculate the integrated intensity of each peak, the peak wavelength and the linewidth and we present them below (Figure 42). In the diagram of integrated intensity vs fluence for the “increasing power” case (logarithmic scale, figure 42b)) we observe that the data are well described with a linear fitting of slope 0.77 ± 0.03 which is close to the one found in exfoliated samples [18]. This sublinear behavior is expected because of the presence of non-radiative defect-mediated recombination centers. At higher fluences (higher than $2 \cdot 10^3 \text{ Wcm}^{-2}$), there is a trend for saturation which could be caused by onset of Auger recombination. In the low power regime, the peak blueshifts and its linewidth decreases with increasing power. The higher pump leads to the formation of more electron-hole pairs which compensate the effect of doping. As a consequence, the exciton emission is enhanced compared to trion.

On the other hand, the “decreasing power” data present a different behavior. The peak intensity is lower than before for the same pump-power. The irradiation could have caused the molecules that are physisorbed to be partially removed from the surface which would lead to a lower emission. Moving to smaller fluences could give the chance for adsorbates to return to the surface and the sample to return gradually to its former situation. The peak position and linewidth show a complicated behaviour that can not be easily explained.

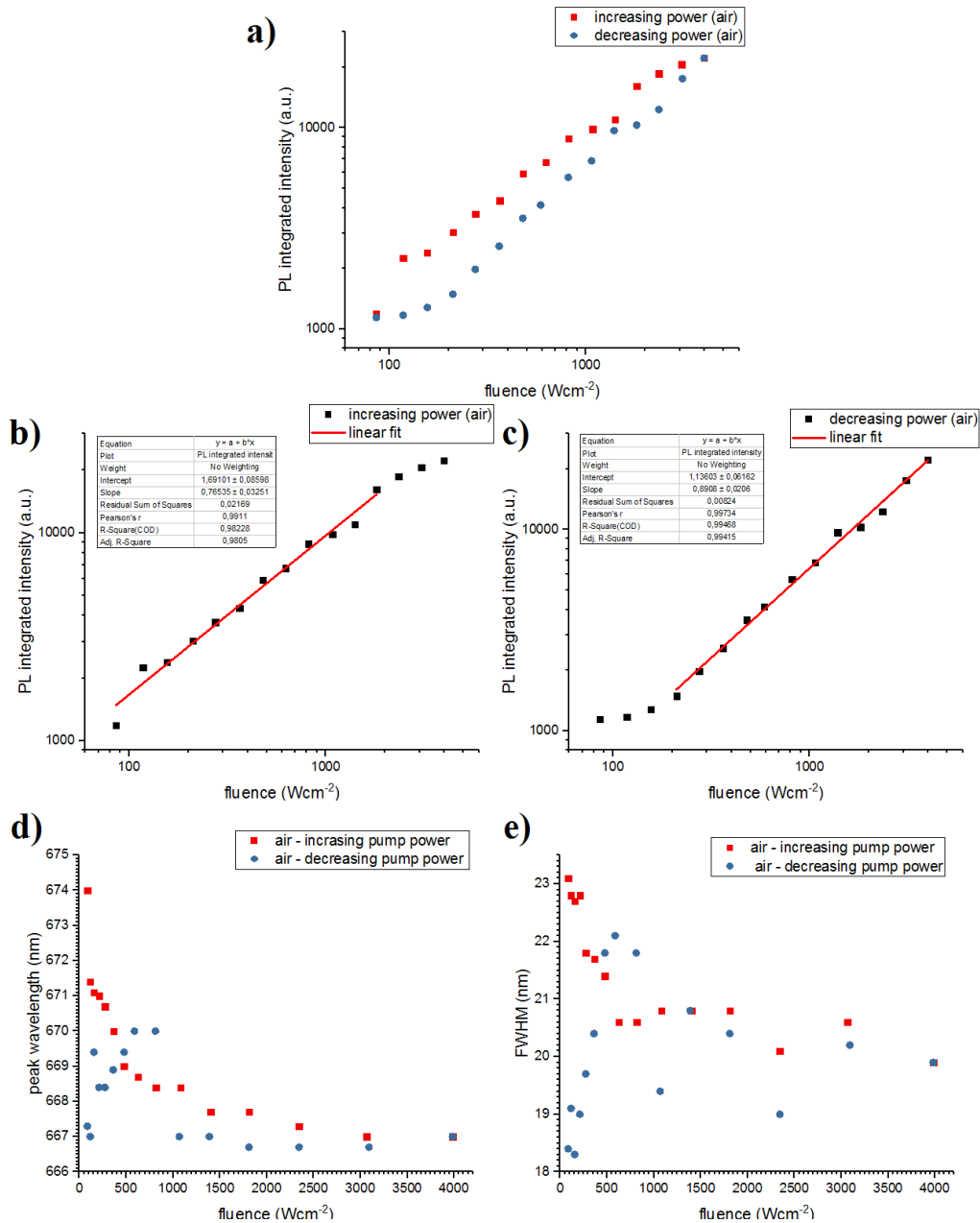


Figure 42: a) The evolution of the integrated intensity with pump fluence in a log scale when we increase (red data) and decrease (blue data) the incident power, b), c) fitting the linear part of the curves and d), e) the evolution of peak wavelength and FWHM with incident fluence respectively

Pump power dependence in vacuum

We repeated the same experiment but this time the pressure inside the chamber was kept constant at 10^{-4} mbar. We present the PL evolution for the case of increasing and decreasing power.

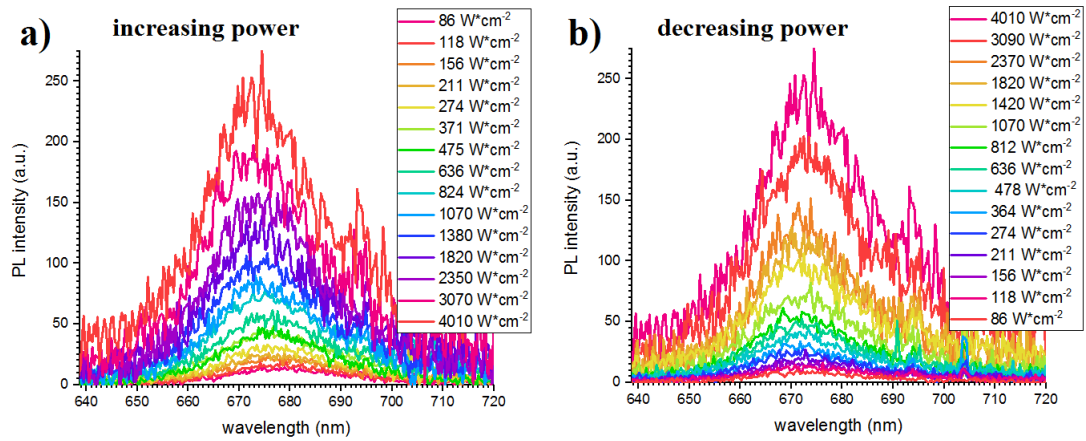


Figure 43: PL spectrum evolution with pump power when we move a) from low fluences to high and b) from high to low

The evolution of the peak's characteristics is different this time as can be seen in figure 44. All data seem to obey the linear fit (when logarithmic scales are used). The slope of the straight line is the same (0.77 ± 0.03) indicating that the recombination mechanisms have not changed. This time the absence of adsorbates in the atmosphere may result in the fact that the “increasing” and “decreasing power” curves present similar intensities.

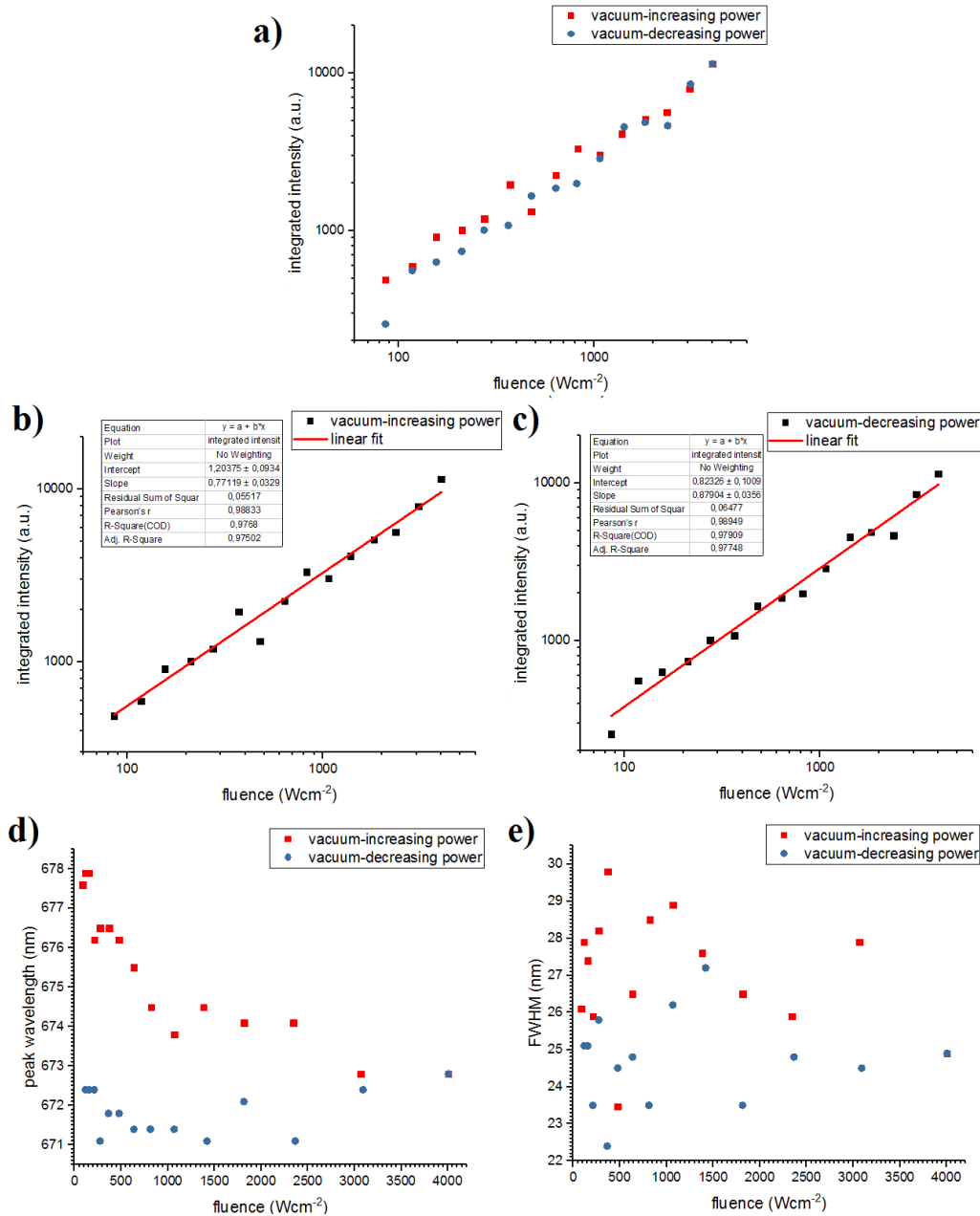


Figure 44: a) The evolution of the integrated intensity with pump fluence in a log scale when we increase (red data) and decrease (blue data) the incident power, b), c) fitting the linear part of the curves and d), e) the evolution of peak wavelength and FWHM with incident fluence respectively

Impact of surrounding environment on PL emission

We wanted to study the interaction of the sample with the environment and particularly to check if the change in PL emission when we measure in vacuum is caused by physisorption or it is the result of low pressure and consequently lower interaction with the substrate. The process is the following: We initially exposed the sample to ambient air, then vacuum, then N_2 and finally back to air and measured its

PL response in each case. The fluence was kept constant at 680 Wcm^{-2} , the sample was kept inside a cryostat vacuum chamber (at room temperature) and a Verdi (532m) pump laser was chosen. All measurements were taken in room temperature. Each time the PL was maximised by micro movements to account for any setup misalignment. Firstly, we measured the PL at air. Then, we pumped the chamber until a vacuum of 10^{-2} mbar and again maximized the PL signal by small movements and focus. We repeated the measurement after 20 minutes to check if the PL response has changed. The next step was to introduce an inert gas – N_2 – in the vacuum chamber in order to study the effect of pressure (if any) on our material. After the first measurement we repeated the measurement 3 more times with a delay of 5, 10 and 15 minutes (total time around 30 minutes). Last but not least, we pumped the chamber again to remove the N_2 and reintroduced air. We measured the sample 3 times after air was introduced with a time delay of 35 and 45 minutes between each measurement (total time 80 minutes).

In figure 45, we present all the PL spectra taken and we plot their integrated intensity in plot b.

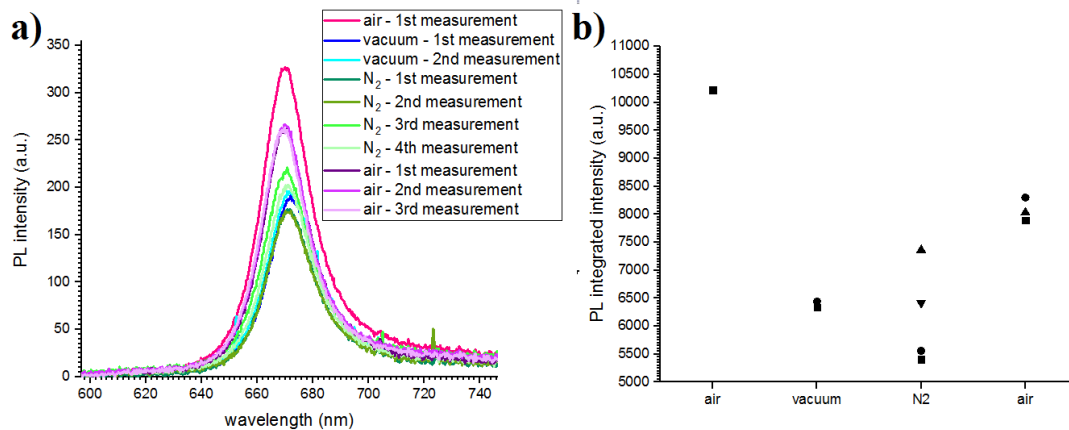


Figure 45: a) Comparison of the PL spectra in air, vacuum and N_2 at 295K and b) the evolution of integrated intensity in different environments, The different data in the same environment correspond to different times and possibly focus and irradiated spot as well. The used fluence is 680 Wcm^{-2} .

The PL intensity drops by a factor of x2 when the air is pumped out of the chamber. This is an indication that there is a strong interaction between air molecules (e.g. H_2O , O_2) and the MoS_2 material. It has been reported that the adsorption of these molecules (at defect sites) causes the depletion of the surface from excess electrons (p-type doping) and the relative intensity of $I_{\text{air}}/I_{\text{vacuum}}$ is related to the amount of defects in the material. While the PL intensity is not influenced significantly by the number of defects when measured in vacuum, the emission of a defective material is higher than the pristine's when measured in air. [91], [106], [107] These studies report a redshift

of the peak when we measure in vacuum (arising from doping) which is also found in our work to a small extent - the peak redshifts by 2.5nm. The changes occurring in the emission because of the different environment are rapid as we did not track any further variation as soon as the pressure stabilized leading to a characteristic time of smaller than a minute (the time it takes to pump down).

The next step was to make a further check on our hypothesis of physisorption. We introduced an inert gas – N₂- in the vacuum chamber. We observed that the emission did not change drastically and the intensity was similar to the one measured under vacuum. Small variations could be the result of different focus and site aimed due to unwanted chamber movement. The peak wavelength changed slightly as well (decreased by 1 nm compared to vacuum). These minor changes support the theory of physisorption. Finally, we pumped the N₂ from the chamber and reintroduced air. The intensity immediately increased but never reached its original value within the 80 minutes that the emission was recorded. We conclude that possibly more time is needed for the adsorption to fully recover.

4.2 2D material transfer

The same techniques were used to study the effects of the transfer process on the monolayer MoS₂.

4.2.1.1 Optical Microscopy

Optical microscopy was used to evaluate the possible damage caused by the transfer process. The monolayer region was successfully transferred. However, we observed subtle changes. The extend of damage was different in each sample but there are some general characteristics that were obvious in the majority of the transferred samples.

Some monolayer triangles are missing and we observe wrinkles and cracks in the continuous monolayer region. Also, in some samples we could see some “pink regions”. Below, we present microscope pictures of a sample that was just transferred.

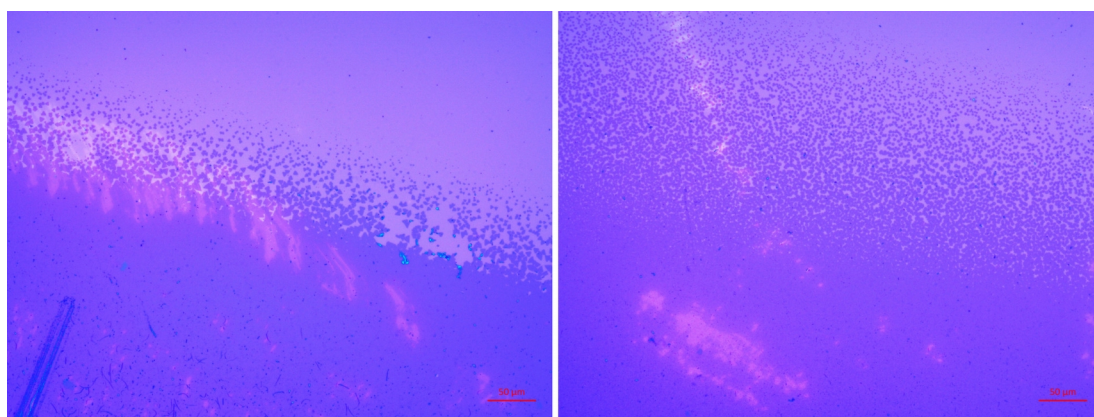


Figure 46: Microscope pictures of the sample “standard 09” after transfer to a new Si/SiO₂ substrate was completed.

4.2.1.2 Raman spectrum

Raman mapping (5 spots per sample) of the samples was taken after transfer using the same parameters (see 4.1.2).

The calibration of the Raman set-up is done by shifting the Silicon peak to the reference value each time. This ensures any errors of the Raman spectrometer are canceled out. For example, in figure 47 we compare the Raman spectra of a sample where the calibration is slightly different between the two measurements (before and after the transfer) and this is easily shown in figure 47c) where the Si peaks differ by 1 cm^{-1} in the two measurements.

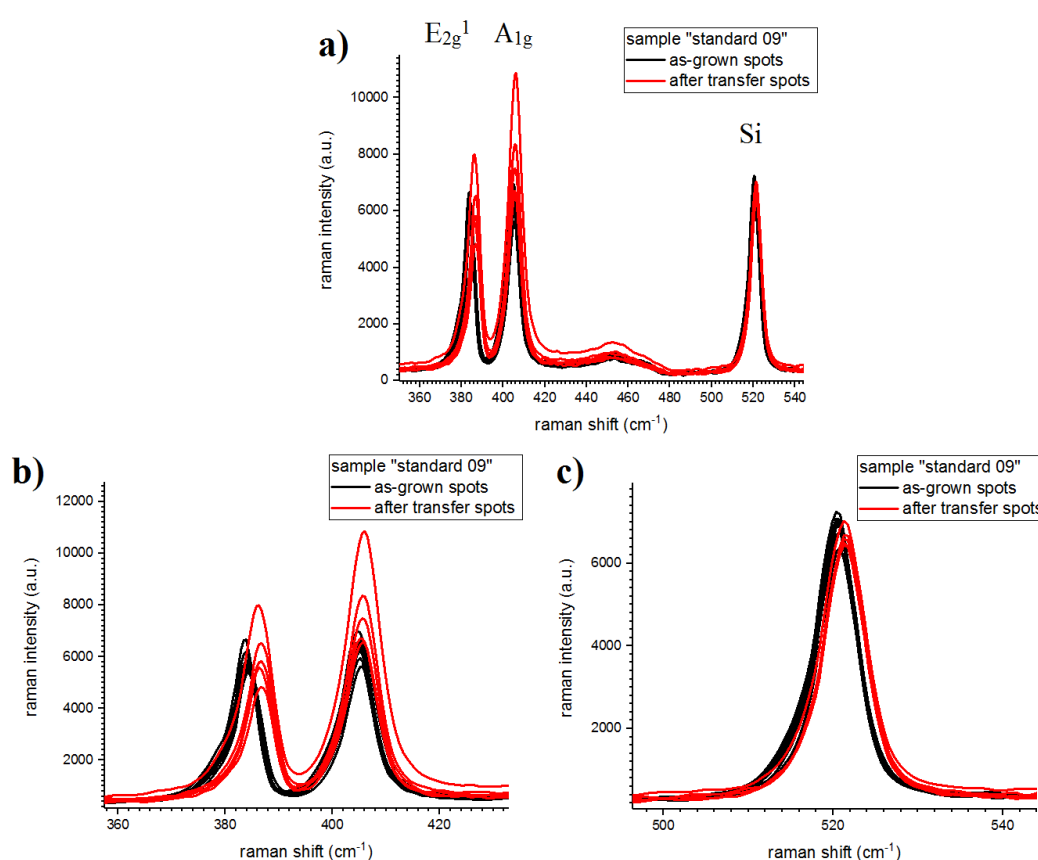


Figure 47: a) Raman spectra of the sample "standard 09" before and after its transfer to a new substrate and the b) E_{2g}^1 and A_{1g} modes, c) the Si peak in a higher magnification to observe small differences.

The peaks are fitted the same way as in 4.1.2 and they are further processed so that the resulting shift from the different calibrations is removed. From the comparison of the characteristics we find the following results:

- there is a systematic stiffening of the E_{2g}^1 mode by 1.4 cm^{-1} . This is attributed to biaxial strain release which had been induced during the CVD growth and

has extensively been reported before. The amount of strain will be calculated later in the text

- Because of biaxial strain we would expect the A_{1g} mode to harden as well but to a lesser extent. In contrast, the mode is slightly softened (around 0.3cm^{-1}). We believe that this is the result of two opposite effects: the strain and n-doping. Release of biaxial strain tends to stiffen the mode while n-type doping tends to soften it. So, n-doping effect overcompensates the small effect of strain and the mode net effect is softening.
- The linewidth of the modes does not seem to be influenced drastically by these changes. Based on literature (see 3.1.3.2, 3.1.3.3), we would expect the FWHM of E_{2g}^1 to be affected by strain while A_{1g} to be influenced by doping. So, possibly they are not as sensitive as we expected.
- The mode spacing is decreased after transfer (about 1.7 cm^{-1}) as a result of the reasons mentioned above. The resulting spacing is around 19 cm^{-1} which agrees with the values found in an exfoliated monolayer MoS_2 ($\sim 18\text{-}19\text{cm}^{-1}$). [91], [96], [108]
- These changes are systematic, i.e. they are observed in all transferred samples.

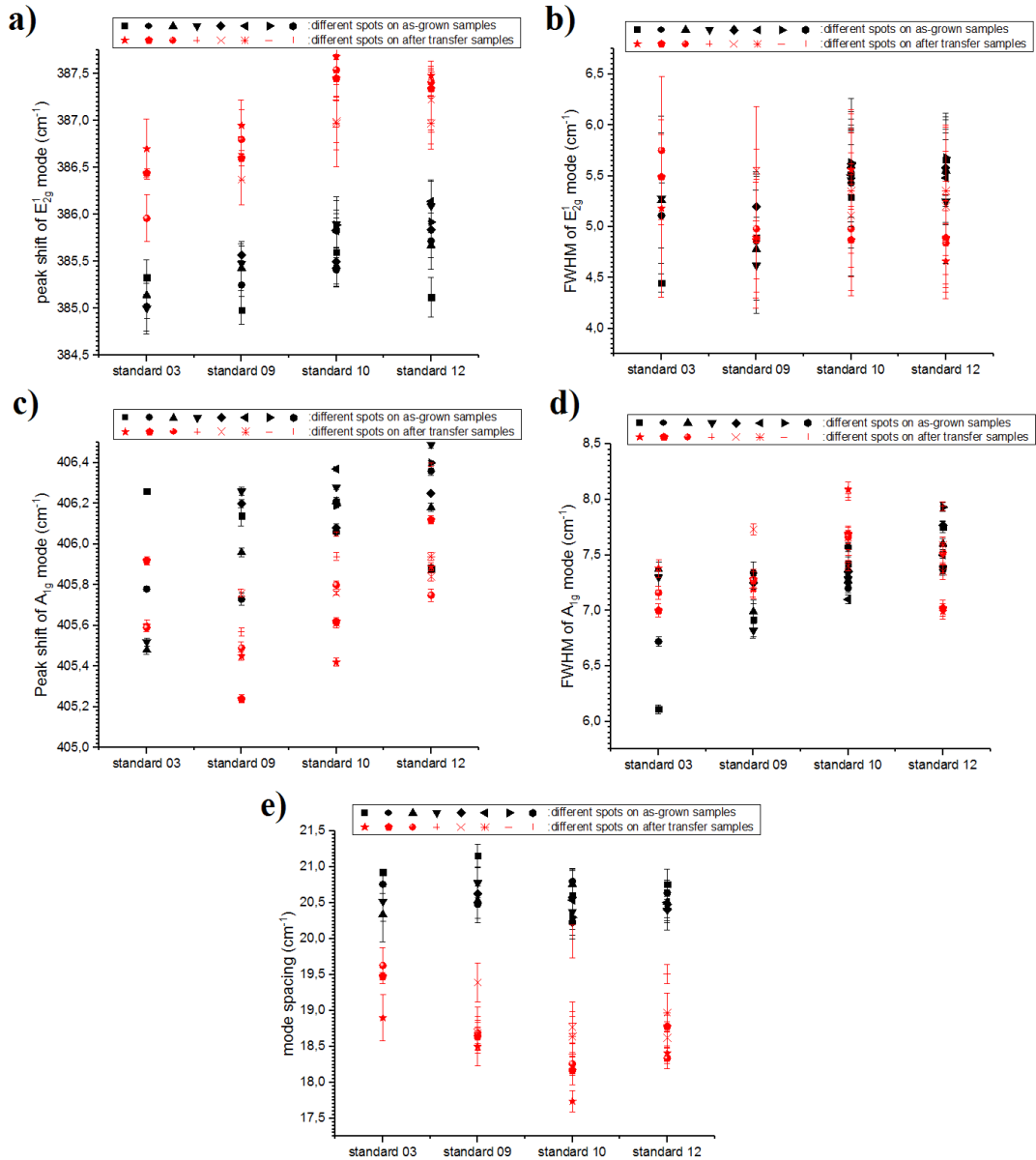


Figure 48: a) Raman comparison of E_{2g}^1 a) peak position and b)FWHM, A_{1g} c)peak position and d)FWHM and e)spacing between the two modes. The comparison is between “before” and “after” transfer for different samples in order to prove the systematic character of the changes.

Based on the shift of the peaks that resulted from the comparison of as-grown and transferred samples, we are able to estimate the amount of strain in our material. Different studies have shown that E_{2g}^1 and A_{1g} mode peak energy change approximately linearly with biaxial strain: -4.48 [73] and $-5.2 \text{ cm}^{-1}/\%$ [71] strain for E_{2g}^1 mode (based on two different studies) and -1.02 and $-1.7 \text{ cm}^{-1}/\%$ strain for A_{1g} mode. For the calculation of strain we will use the results of the first study but the

differences are not so big to concern us. The A_{1g} mode is influenced by doping. So we will calculate the strain based on E_{2g}^1 Raman shift changes.

sample	ΔE_{2g}^1 (cm ⁻¹)	ΔA_{1g} (cm ⁻¹)	Calculated strain based on [73]
Standard 03*	1.25±0.41	-0.06±0.41	(-0.28±0.09) %
Standard 09	1.37±0.33	-0.56±0.28	(-0.31±0.07) %
Standard 10	1.59±0.40	-0.34±0.40	(-0.35±0.09) %
Standard 12	1.47±0.42	-0.35±0.33	(-0.33±0.09) %

* this sample was not transferred to a Si/SiO₂ substrate as the rest but to a DBR/SiO₂ substrate

4.2.1.3 Photoluminescence spectrum

The Raman set-up was used to record the PL emission of the transferred sample with known parameters (10⁴ Wcm⁻² fluence, room temperature, atmospheric pressure, 473nm wavelength of the laser). 5 spectra at different sites were recorded for each sample.

In figure 49, we present the comparison between the spectra that were taken before and after the transfer of a sample to another substrate and we can see the drastic changes that occur in the PL spectrum. The PL intensity has decreased by more than 10 times (in other samples the PL reduction was even higher), the dominant peak has broadened and blueshifted while the B-exciton peak is also more apparent after transfer.

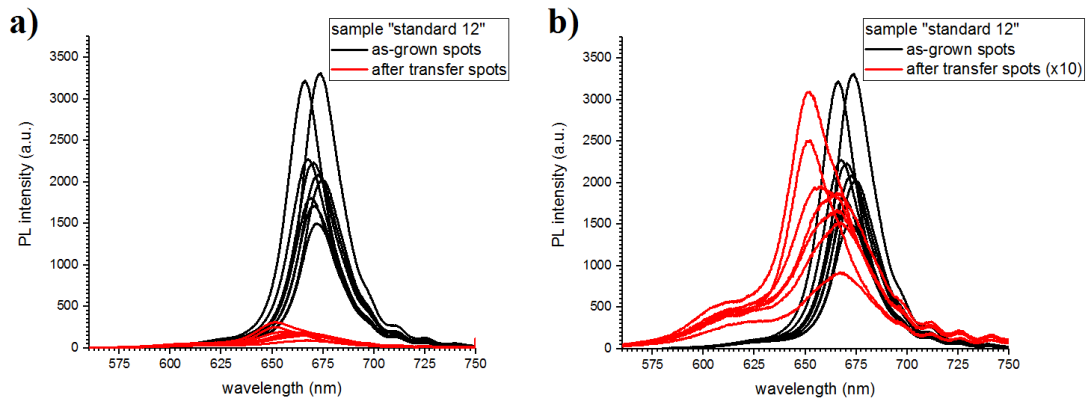


Figure 49: a) PL spectra of sample “standard 12” before (black curves) and after transfer (red curves) b) the PL intensity of the sample after transfer is magnified by 10 in order to observe the changes in a better way.

The fitting of the data after transfer was again pseudovoigt but this time one peak can not fit the data well. In each sample, the minimum of the peaks needed were used. In most of them three peaks were required (A-exciton overlapping with trion and B-exciton) but in some cases, only two peaks were used to perform the fitting. The Trion peak usually dominates after transfer and was always used in the fitting. Below, we present a typical fitting of the spectrum.

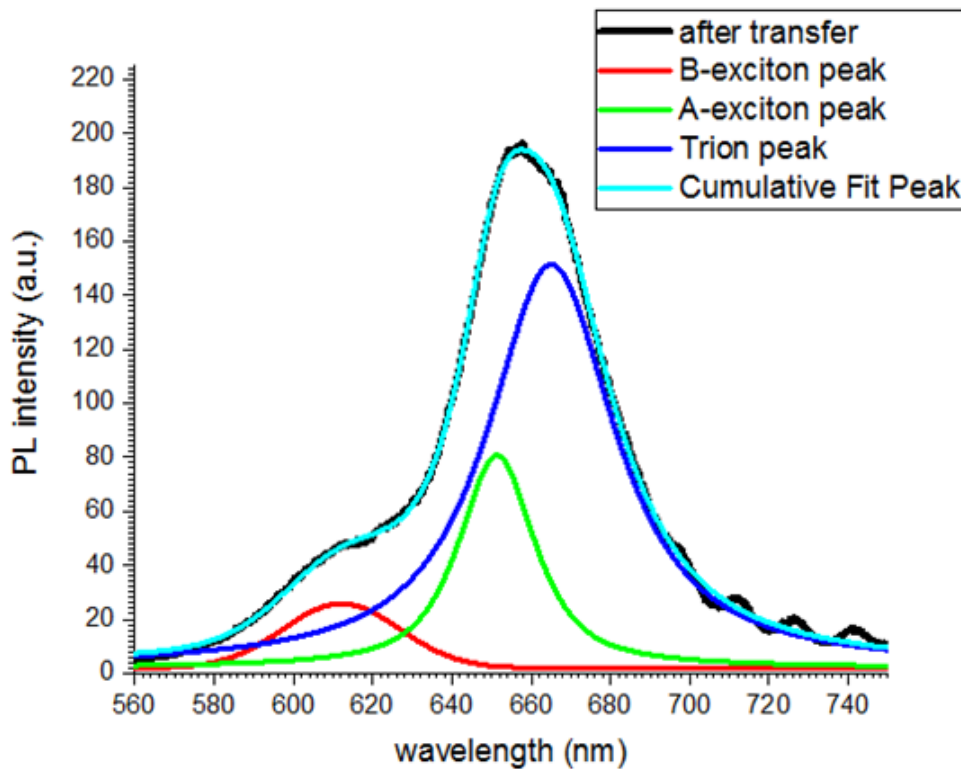


Figure 50: A typical spectrum (black curve) of a transferred sample and its analysis (magenta curve) using three pseudo-Voigt peaks (Red, Green and blue curves).

In order to explain our observations and find if they are systematic, we present the changes in a more quantified way in figures 51, 52 and 53. We have already suggested in 4.2.1.2 that there are two mechanisms that rule the transfer process: strain and doping. So, we need to check if they are consistent with PL observations as well. Doping could explain the high decrease on the intensity of the main peak and the fact that the trion peak now becomes dominant (see figure 52). If there was no other mechanism we would expect the main peak (A-exciton and trion) to redshift as the contribution of the trion gets higher. In contrast, the peak blueshifts (figure 51b) However, because of strain release we expect the bandgap to increase (see 3.2.3.1), which agrees with our findings.

We should also notice that the linewidth of the A-exciton remains unchanged with transfer (figure 53b). The linewidth of trion is much higher than A-exciton's which explains why the linewidth of the main peak increases after transfer (figure 53a).

Finally, the increase in intensity ratio of B/A exciton indicates that non-radiative recombination plays a more significant role after transfer (as we explained in 3.2.3.5). So, the transfer process could possibly cause defects in the sample.

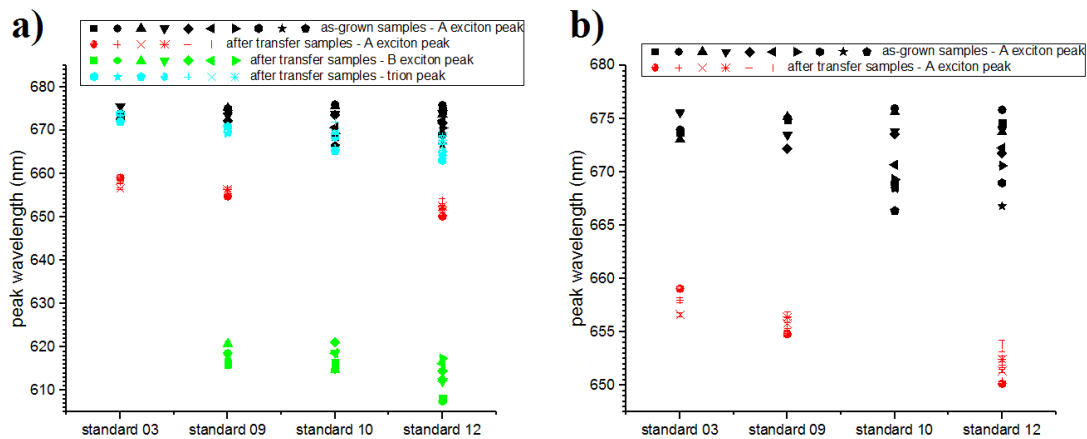


Figure 51: PL comparison of the A-exciton before transfer and A-exciton, trion and B-exciton after transfer. We compare a) the peak wavelengths and b) the A-excitonic peak before and after transfer alone.

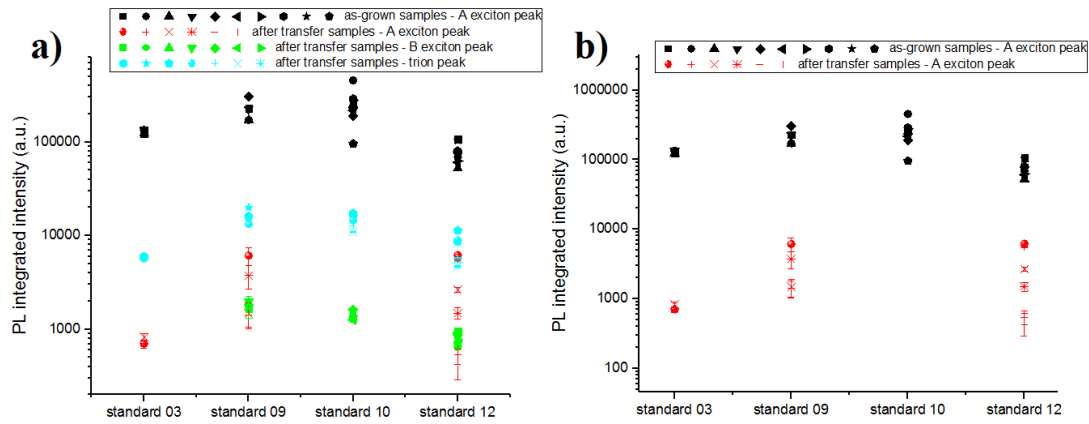


Figure 52: PL comparison of the A-exciton before transfer and A-exciton, trion and B-exciton after transfer. We compare a) the integrated intensity and b) the integrated intensities of A-exciton alone.

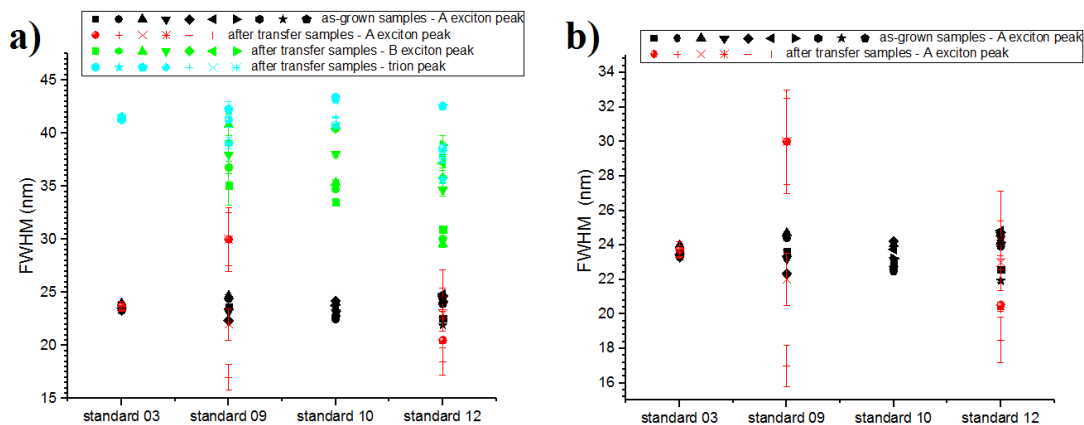


Figure 53: PL comparison of the A-exciton before transfer and A-exciton, trion and B-exciton after transfer. We compare a) the FWHM and b) the linewidth of A-exciton before and after transfer alone.

We can not quantify the doping and defect variations but we can calculate the change in strain. For the energy shift of the PL peaks under biaxial strain we know that it is found $-(90-100)$ meV/% tensile strain (see 3.2.3.1). For the analysis we choose -100 meV/% strain.

sample	A-exciton's energy shift (meV)	Calculated strain based on [72]
Standard 03	45.3±4.5	(-0.45±0.05) %
Standard 09	52.4±4.1	(-0.52±0.04) %
Standard 10	The fitting does not require the presence of A-exciton after transfer	
Standard 12	57.8±8.8	(-0.58±0.09) %

Room-temperature power dependence in atmospheric pressure

The raman set-up was used to record PL after transfer with fluences (10^4 Wcm^{-2} and $4.6 \cdot 10^2 \text{ Wcm}^{-2}$). All data were recorded at room temperature and atmospheric pressure. The normalized spectra for both cases appear in figure 54.

In the low fluence regime, the radiative recombination occurs through A-excitons while in high fluence regime the concentration of B-excitons and trions is relatively high. This is the opposite behaviour of the one observed in as-grown samples. We assume that at such a high fluence, the excited carrier density is high enough that the recombination through A-exciton channel is not quick enough to consume all the photogenerated carriers. This fact, in combination with the increased n-doping and defects promote the recombination through trions and B-excitons (3.2.3.2,3.2.3.5).

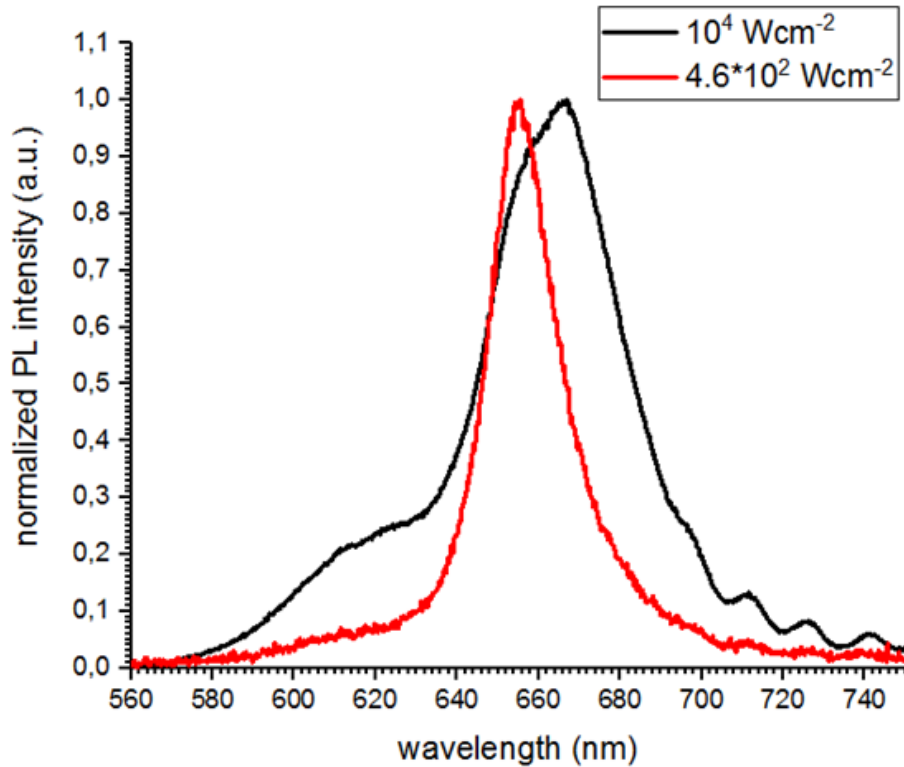


Figure 54: PL emission of an as-transferred sample measured at room temperature and atmospheric pressure in two different fluences.

4.3 Chemical treatments - TFSI

We tested the influence of the TFSI treatment on the CVD-grown samples. The processes followed in TFSI treatment are well described in the literature. As far as sample preparation is concerned, section 3.5.1 presents the standard treatment. The samples that were used had previously been transferred to a new Si/SiO₂ substrate. The differences are concentrated in the pretreatments of the samples:

- Some samples were annealed in 100°C in vacuum for 15 minutes just before the treatment. We will call it the standard process.
- Some samples were annealed in forming gas at a temperature of 300°C for 5 minutes (pretreatment in forming gas).

The stability of the TFSI effect was studied in atmospheric air. We also checked the reproducibility of the process repeating the treatment 10 days after the first treatment. Finally, we used e-gun evaporation to evaporate SiO₂ on top of a sample just after TFSI treatment to test if the effect can be locked into place

4.3.1 Optical Microscopy

Microscope pictures were used to find if the treatment causes structural damage to the 2D material. Figure 55 shows areas of a sample that was treated with TFSI.

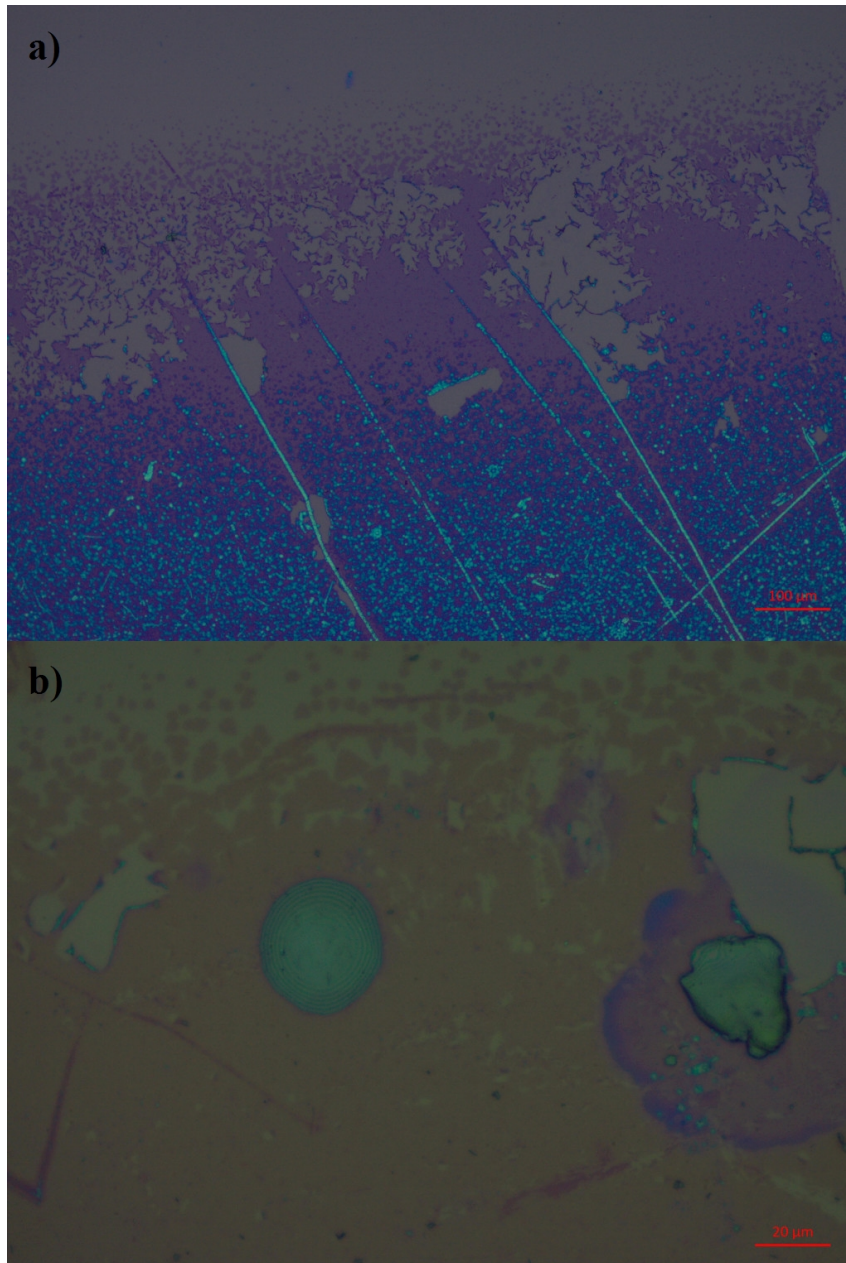


Figure 55: *Optical pictures of a sample that was treated with TFSI.*

Some monolayer regions were removed during the treatment. The above pictures are taken from a sample that was treated twice. In figure 55b), we observe a blue bubble at the middle of the image. The PL emission from this spot was extremely high,

leading us to believe that the 2D material is decoupled from the substrate at that point forming a bubble.

4.3.2 Raman spectrum

We studied the changes that TFSI treatment causes to our sample through Raman measurements. The parameters used are the same as in 4.1.2. Several sites throughout the monolayer area were measured. The fitting used was a pseudovoigt and Raman data were calibrated so that the Si peaks overlap

We present the changes that occur in the Raman characteristics of two samples: Sample “standard 12” and “standard 14”. The linewidth of the modes is not so sensitive to changes and so we will not present it here.

Apart from the difference in the procedure of the TFSI-treatment between the two samples (standard 14 was pretreated in forming gas while standard 12 with the standard process) which we have not found to cause any difference, the time that the Raman measurements were taken is different: The “standard 12” was measured just 1-2 hours after the treatment while “standard 14” was measured 1 day after the treatment due to the Raman set-up availability.

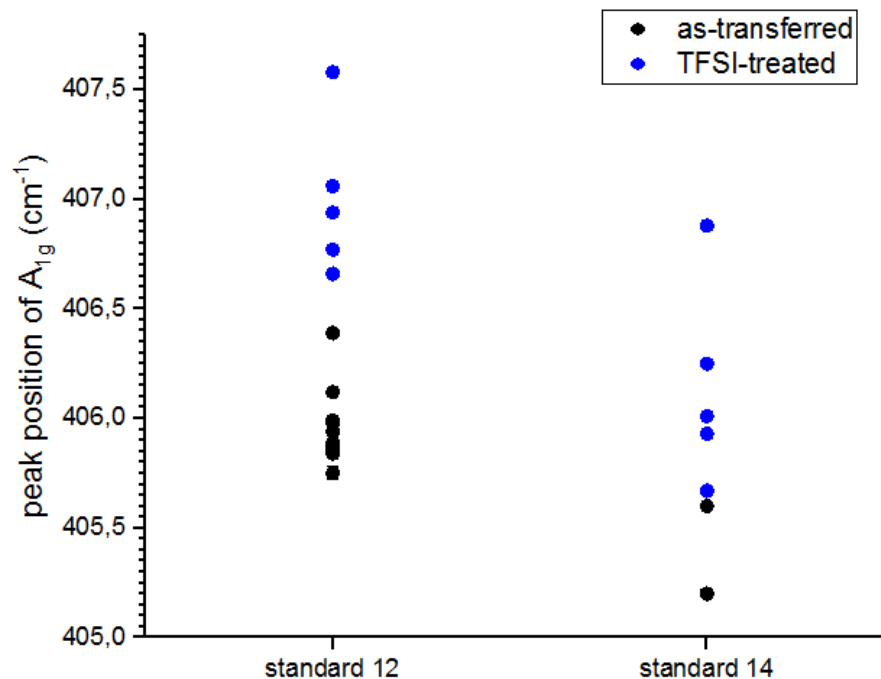


Figure 56: A_{1g} mode comparison between as-transferred and treated samples.

The main change that we observe in the Raman characteristics is the stiffening of A_{1g} mode (and consequently a small change in mode spacing) which could be attributed to p-doping of the sample. This hypothesis will be checked by PL measurements.

4.3.3 PL spectrum

The PL response of freshly treated samples was recorded using the Raman set up. Various spots throughout the sample were irradiated with a fluence of 10^4 Wcm^{-2} at room temperature and atmospheric pressure.

In figure 57a), we present three representative spectra: when the sample was as-grown, as-transferred and TFSI treated. The intensity axis is in a logarithmic scale. We observe that $I_{\text{TFSI}} \approx 100 \cdot I_{\text{transferred}} \approx 10 \cdot I_{\text{as-grown}}$. Also, in figure 57b) we can see the same spectra with normalized intensities. The A-exciton recombination mechanism becomes dominant again after the chemical treatment while the emission from trions and B-excitons has diminished. Our results agree with the assumptions made in the analysis of the transferred samples (release of strain, trion and B-exciton emission have a big contribution in the spectrum). The domination of A-exciton over the rest after treatment, indicates that TFSI possibly causes p-type doping and/or passivation of defects as we have explained before.

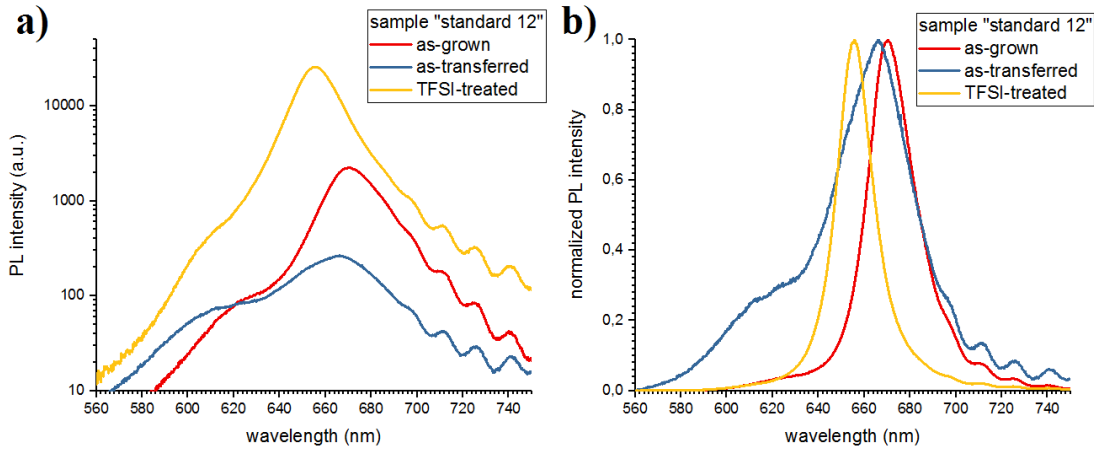


Figure 57: Comparison between as-grown, as-transferred and TFSI-treated representative spots on sample “Standard 12”. In a) the PL intensity is in logarithmic scale in order to present the change in peak intensity while in b) the intensity is normalized in order to compare the shape of the curves. The fluence used was around 10^4 Wcm^{-2} .

These observations are systematic, i.e. they were found in all samples. Our results show that there is a clear enhancement of the PL signal by 10-100 times. In all samples, the characteristics of the emission (peak wavelength and linewidth) became much more uniform across the monolayer region after the treatment which could be explained by the domination of the A-exciton in all regions across the monolayer.

Some more interesting results/conclusions are presented here:

- Ten days after the use of TFSI on a sample, when the effect had nearly vanished, we repeated the treatment. Again, there was a great enhancement of

the PL emission verifying that the effect is indeed coming from a reversible attachment of the TFSI molecules on the surface.

- The SiO₂ evaporation on TFSI-treated sample influenced the TFSI effect and the PL emission decreased almost to the value before the treatment. Even the remaining effect was not maintained in time as the intensity continued to drop. Also, the peak shifted (from 657nm to 670nm) and broadened after the evaporation which could be attributed to doping effect. Finally, when we used high fluences ($10^3 - 10^4 \text{ Wcm}^{-2}$), the encapsulated monolayer region under irradiation was destroyed leading us to assume dangling bonds in the encapsulation material are chemically active causing reactions.

4.3.3.1 Time evolution of TFSI treatment in air

We studied the time evolution of the PL intensity in a sample that was treated with the standard recipe and we compared it to a sample that was pretreated in forming gas. We measured the samples for a period of 9 days under constant conditions in the bespoke PL set-up (pump fluence: 110 Wcm^{-2} , room temperature, 60s exposure time, atmospheric pressure). During this period of time, samples were stored at room temperature and atmospheric pressure. Because the PL emission was not uniform across the monolayer region we measured several sites. The PL spectra evolution with time of a sample (which was pretreated in forming gas before the TFSI process) are shown below.

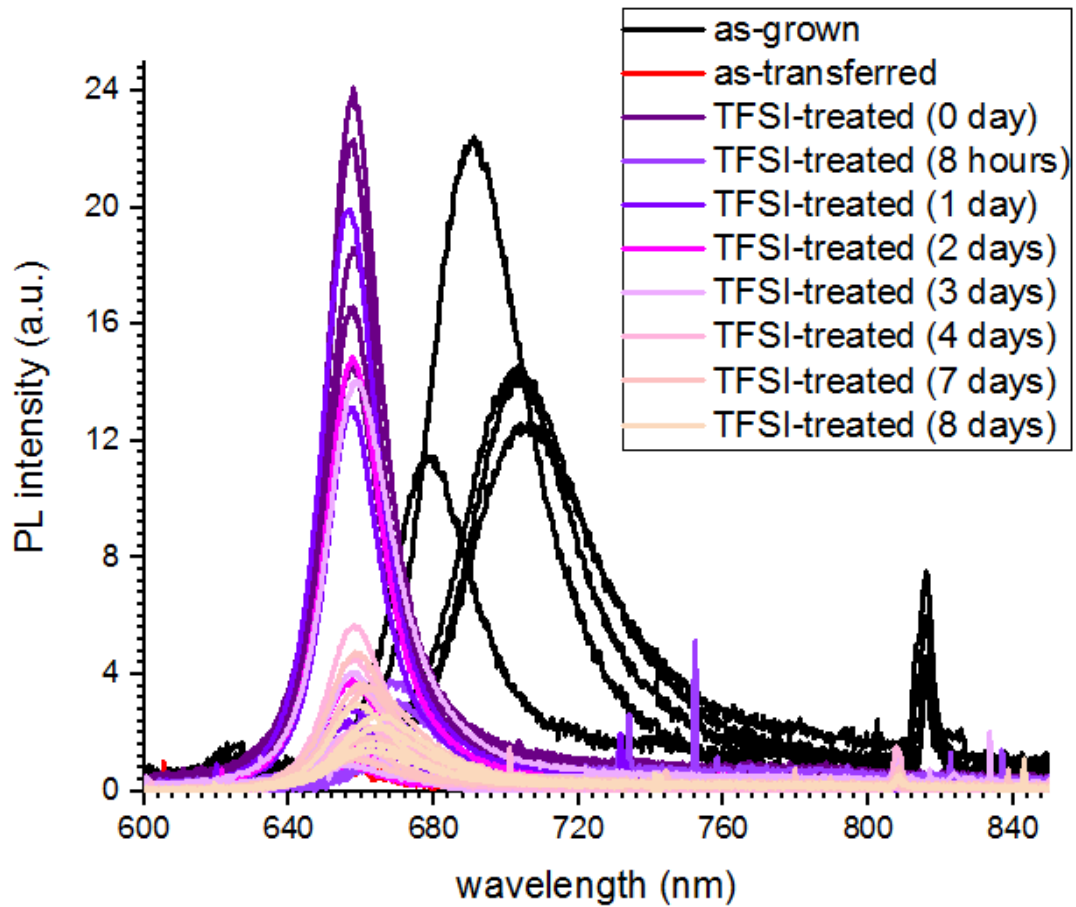


Figure 58: Spectra evolution with time of sample “Standard 14” which was annealed in forming gas before the treatment. The fluence used was 110Wcm^{-2} .

We find the integrated intensity of the peak for all measured sites and by calculating their average we are able to estimate the time evolution of the effect.

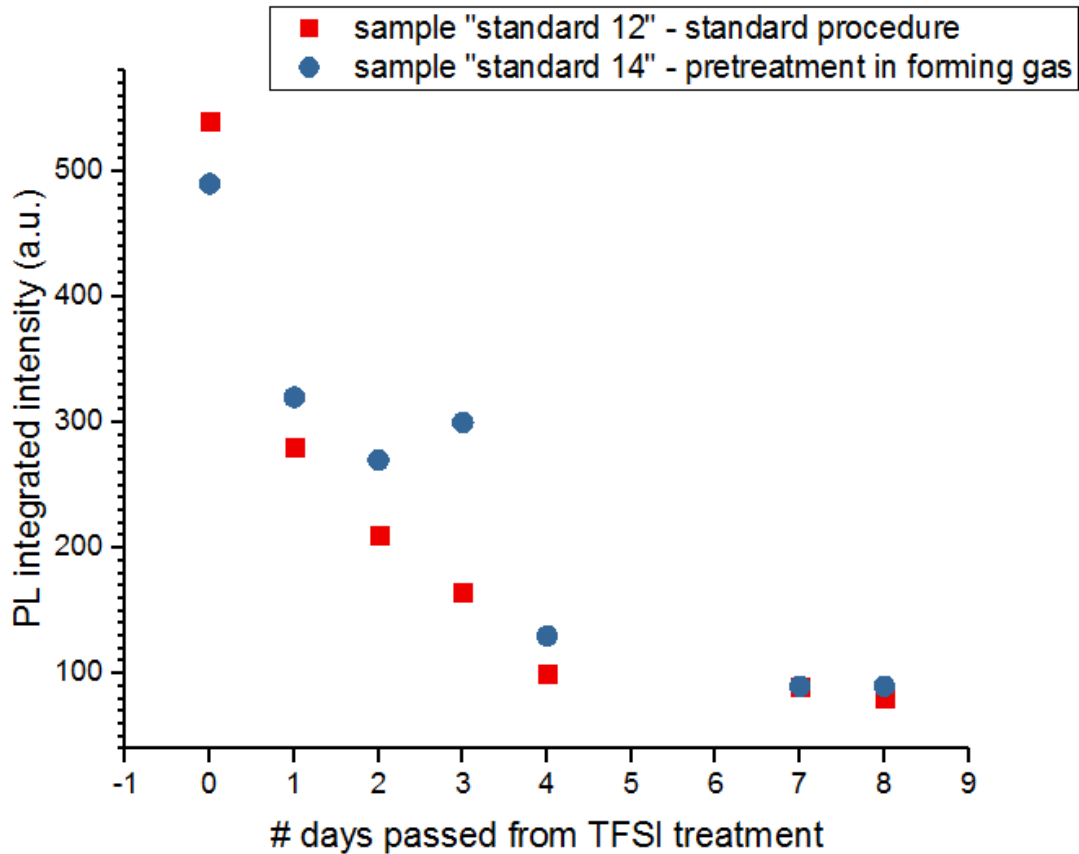


Figure 59: Time evolution of the TFSI effect on two samples: “Standard 12” was treated with the standard process while “Standard 14” was annealed in forming gas before the treatment. The fluence used was 110Wcm^{-2} .

Based on reference [18], the effect of TFSI is more stable in samples that are pretreated. Neither of the two treatments resulted in a stable enhancement of the PL emission and the influence fades away after one week (see figure 59). Furthermore, the two treatments do not appear to offer different stability in contrast to what is reported in [18].

Except from the intensity drop, we track changes in other characteristics of the spectrum as well. The peak tends to redshift and broaden as time goes by (e.g. the linewidth changes from 18-20nm to 25-30nm). Also, the peak wavelength presented a very small variation in freshly treated samples but the variation increased with time. For example, in the freshly-treated sample “standard 12”, the peak wavelength was 655-658nm while in aged TFSI-treated the variation was higher: 662-671nm. All of these observations could be explained by the competition between A-exciton and trion: After TFSI treatment the contribution of trion is negligible (so the peak frequency is around the frequency of the A-exciton and the linewidth is mainly the exciton’s linewidth). As TFSI destabilises, the effect fades away and so the trion’s contribution becomes more important. The relative intensity of A-exciton to trion

could vary from spot to spot. As a result we have less uniform emission and we conclude that the effect evolves differently in different sites of the sample (which is supported by the differences in the intensity as well).

4.3.3.2 Temperature dependent Photoluminescence

Temperature dependent measurements for a TFSI-treated sample were taken. The sample was placed in the vacuum chamber and vacuum (10^{-4} mbar.) was drawn. The sample was cooled down to 25K. Then, we gradually increased the temperature to 300K with a step of 25K. At each temperature, we tried to maximize the emission changing the focus and the irradiated site. The bespoke PL set-up was used for these measurements and the fluence was 450 Wcm^{-2} . The results are shown below.

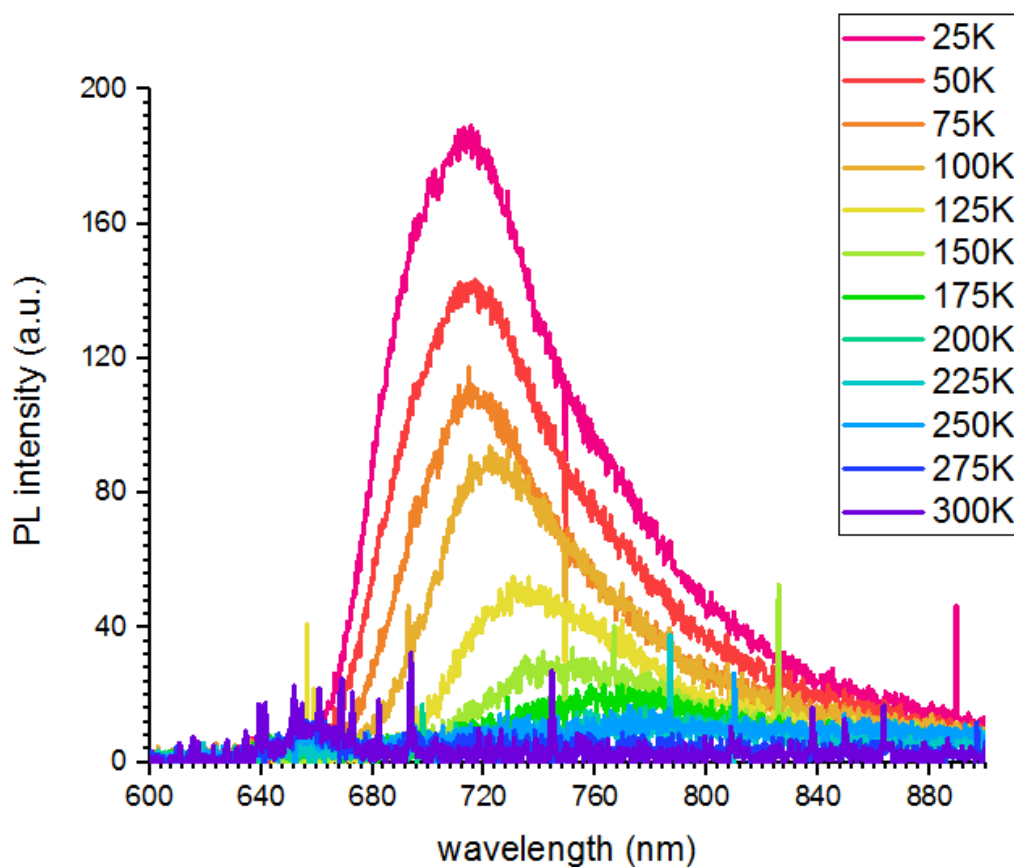


Figure 60: PL spectrum evolution with temperature.

We observe the bound exciton and its evolution with temperature until 200K where it vanishes which was also the case in as-grown samples. However, the relative intensity of free exciton is much smaller and can barely be seen in the recorded spectra.

We find the characteristics of the bound exciton peak (without fitting) and plot them in figure 61.

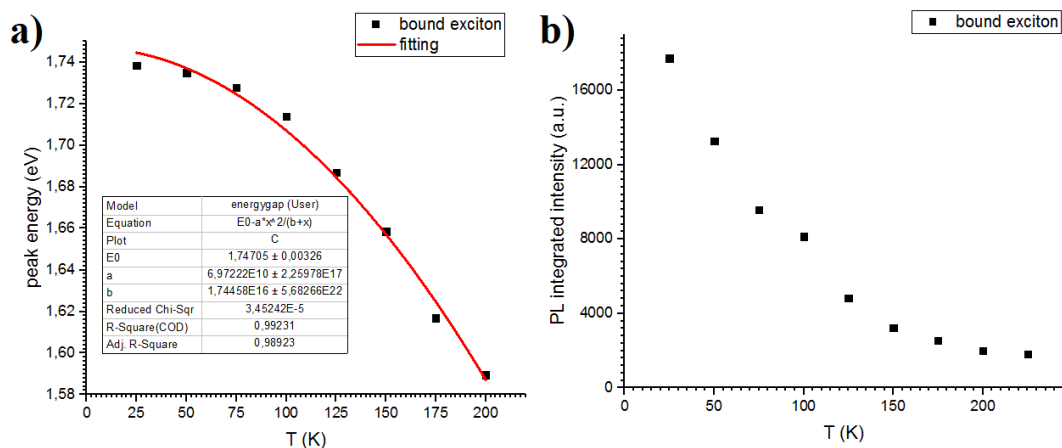


Figure 61: PL a) peak energy and b) integrated intensity of bound exciton as a function of temperature.

The fitting function that we used in peak energy-temperature diagram is the one that was used in as-grown samples. However, the fitting parameters do not coincide in the two cases leading us to identify other mechanisms that affect the PL emission.

4.3.3.3 Low temperature power-dependent Photoluminescence

At the lowest possible temperature in the cryostat (17K), we measured the power dependent PL response of the material. The pump fluence varied from 80-4000 $W\text{cm}^{-2}$ and the wavelength of the laser beam used was 532nm. Below, we present the data.

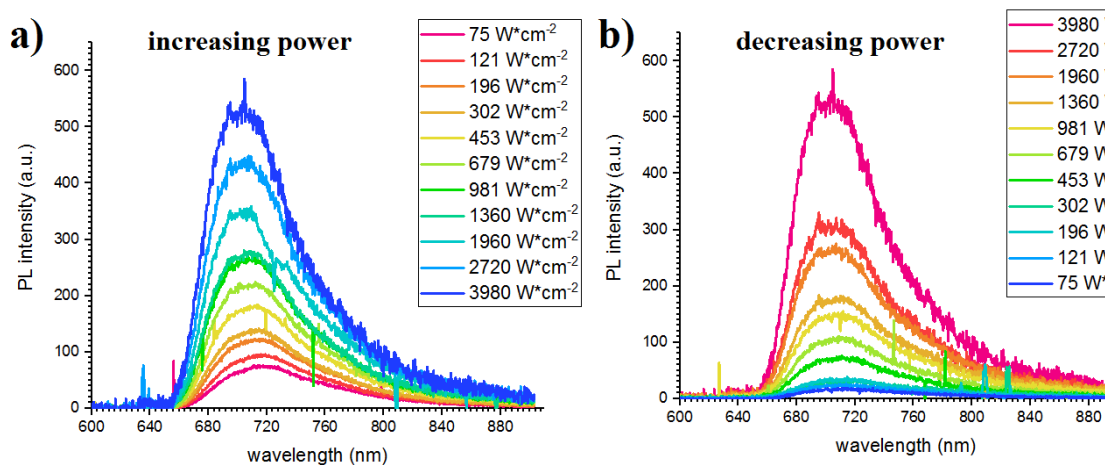


Figure 62: PL response of the material a) increasing the incident fluence, b) decreasing the incident fluence.

The integrated intensity of the bound exciton peak was calculated and plotted in figure 63.

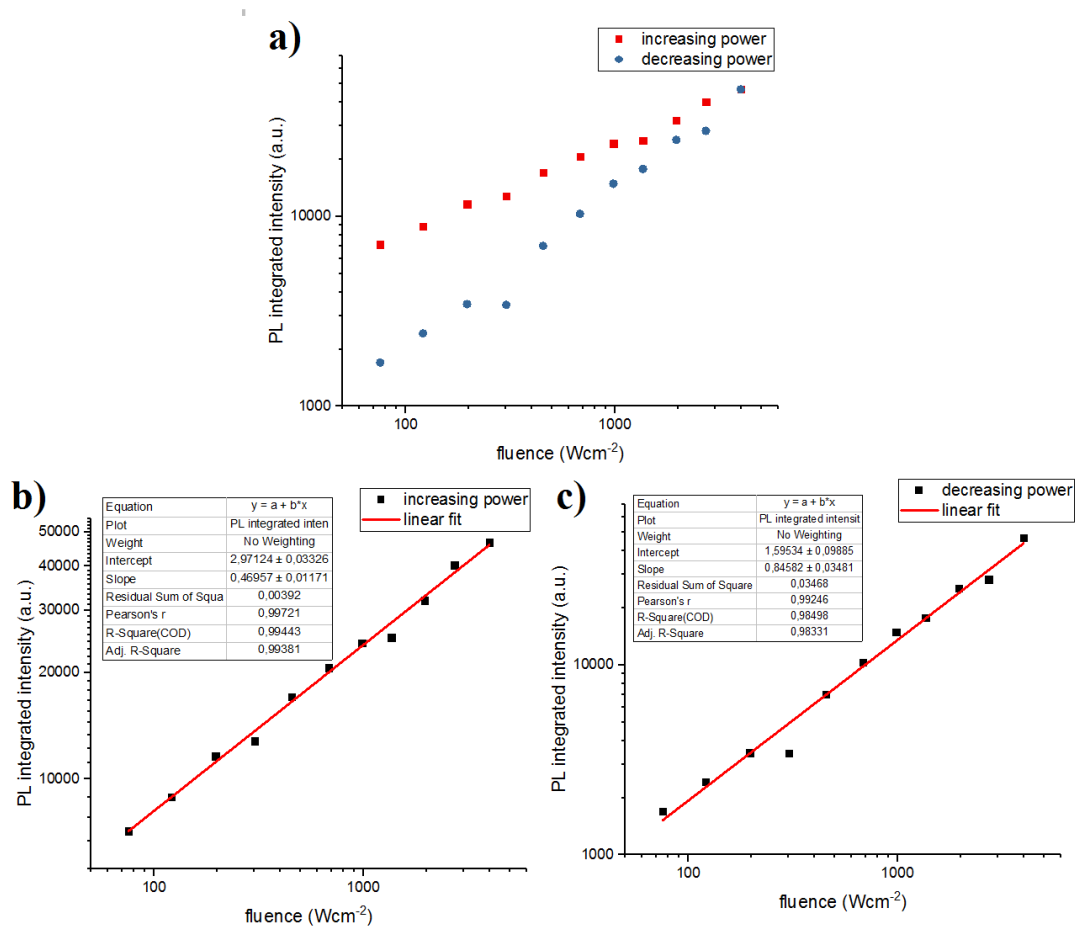


Figure 63: a) Fluence dependence of integrated intensity of bound exciton for “increasing” and “decreasing” power and b), c) their linear fit. All axis are in logarithmic scale.

The PL response of bound exciton follows the same power law as in as-grown samples both for increasing and decreasing power case: $I \sim P^a$ where

- in the increasing power case: $a = 0.47 \pm 0.01$ for TFSI-treated samples and 0.50 ± 0.03 for as-grown samples

- in the decreasing power case: $a = 0.85 \pm 0.03$ for TFSI-treated samples and 0.79 ± 0.02 for as-grown samples

Room temperature power-dependent Photoluminescence in air

The effect of TFSI on our material will be better understood with power dependent measurements in room temperature. The same range of fluences was used to record those spectra. The measurements were taken in room temperature and atmospheric pressure.

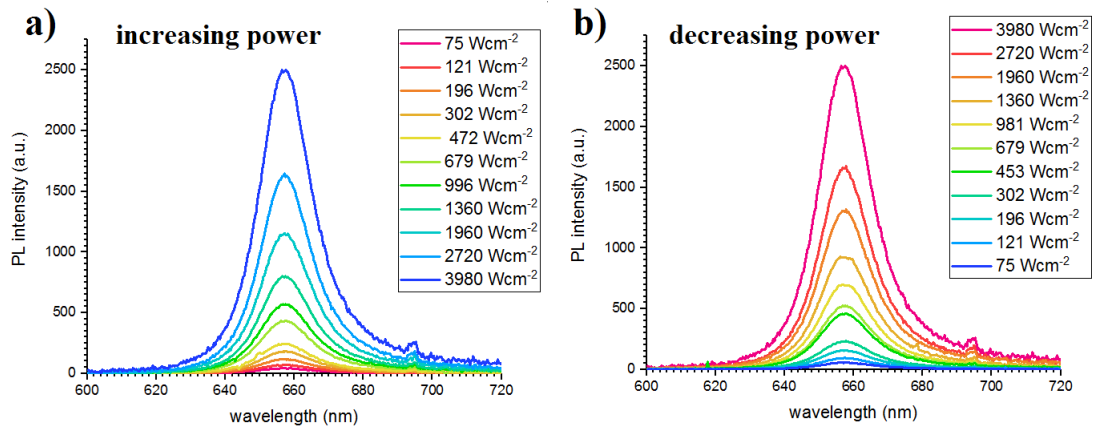


Figure 64: a) The PL spectrum evolution when we a) increase and b) decrease the pump power

We calculate the integrated intensity of the peak (no fitting was used) and plotted the data in a logarithmic scale diagram (figure 65). In this range, the data follow a linear dependence as the slope in the logarithmic scale diagram is approximately unity (1.02 ± 0.01 for “increasing power” and 0.95 ± 0.03 for “decreasing power”). This result is consistent with the passivation of defects. Also, the shape of the peak (peak wavelength, FWHM) remains unchanged when we vary the pump which is in contrast to what we found in as-grown samples. The relative emission of radiative species does not seem to be perturbed by irradiation of the sample. This could be related to the p-doping induced by the TFSI. The intrinsic n-type character of the material has vanished and the adsorbates do not remove the excess electrons from the sample.

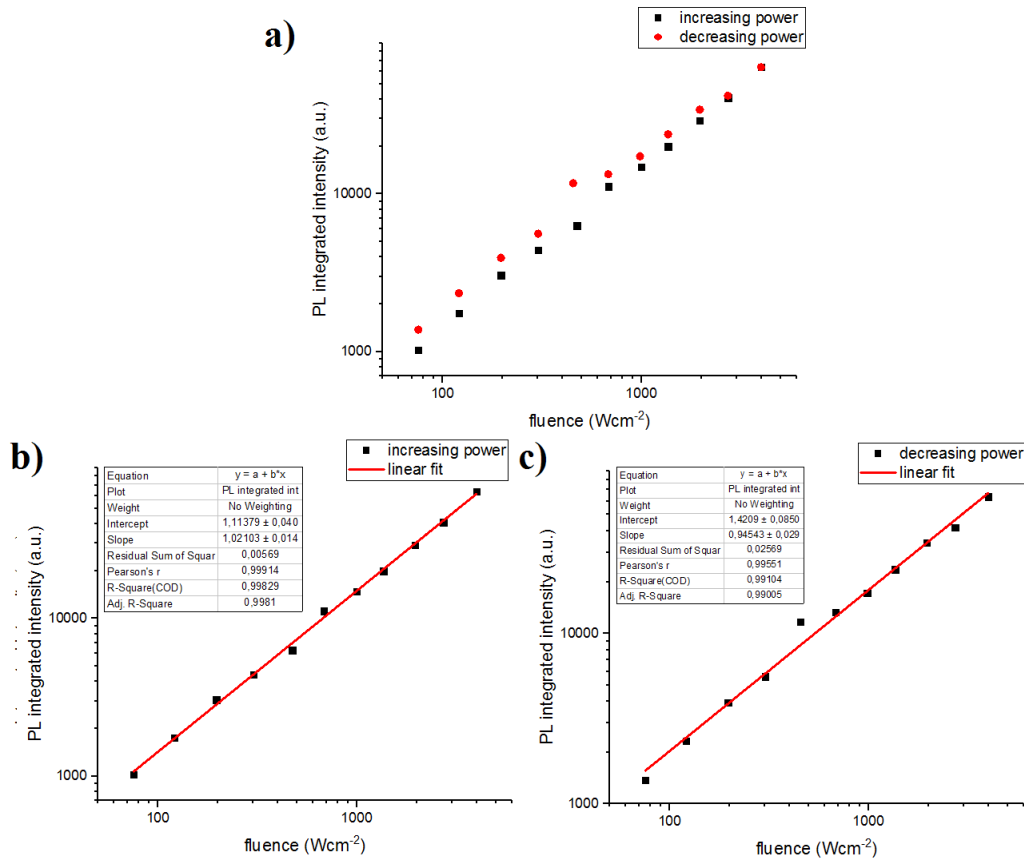


Figure 65: a) The evolution of the integrated intensity as a function of pump fluence in a log scale when we increase (red data) and decrease (black data) the incident power, b), c) fitting the data with linear functions

4.3.3.4 Impact of surrounding environment on PL emission

The interaction of the sample with the environment was tested for TFSI-treated samples as well. The conditions are the same: We exposed the sample in ambient air, in vacuum, in N₂ and again in air and measured its PL response in each case. The fluence was 680 Wcm⁻², the sample was inside the vacuum chamber and a Verdi (532 nm) was the pump laser used. All measurements were taken in room temperature.

In the beginning of the experiment we measured twice the PL emission in a small area of the sample trying to maximize the signal each time. Then, we pumped down to a vacuum of 10⁻² mbar and tried to find again the site with maximum emission. We repeated the measurement one more times after 20 minutes to check if the PL response changed. The next step was to introduce the N₂ in the chamber. After the first measurement we repeated the measurement 2 more times with a total time difference between the first and last measurement around 20 minutes. Last but not least, we created vacuum to remove the excess N₂ and reintroduced air in the

chamber. We measured the sample 3 times in total with a time difference between the exposures of 25 minutes (total time 50 minutes).

In figure 66, we present all PL spectra that were measured and b) their integrated intensity.

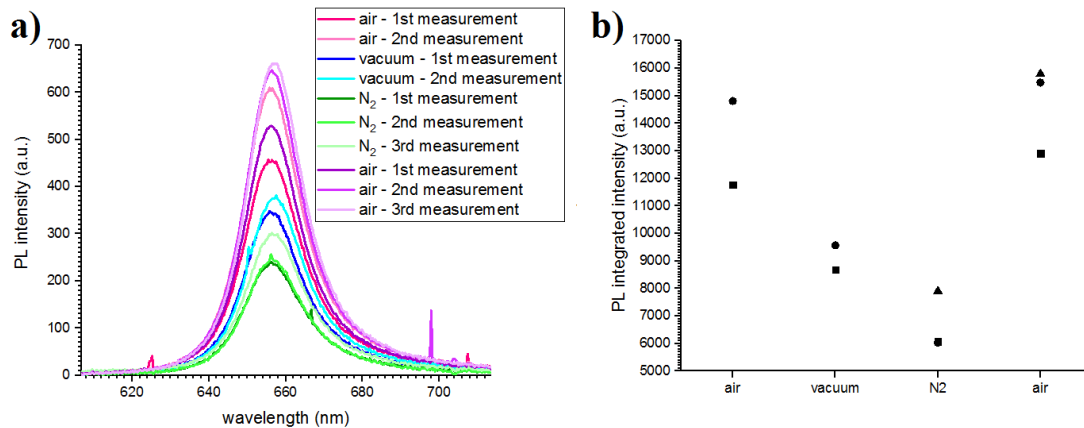


Figure 66: a) Comparison of the PL spectra in air, vacuum and N₂ at 295K and b) the evolution of integrated intensity in different environments, The different data in the same environment correspond to different times and possibly different focus and irradiated spot. The used fluence is 680Wcm^{-2} .

As the sample is exposed to different conditions we observe the following: I) air exposed sample shows the highest PL signal. When exposed to vacuum the signal drops (by a factor of 2) and the effect is even stronger when the sample is exposed to Nitrogen conditions. Finally returning to air leads to a recovery of the PL emission leading us to the assumption that the TFSI is not removed but the interaction with adsorbates is still enhancing the measured response. These results are similar to the ones found in as-grown samples: the intensity drops in vacuum, some measurements in N₂ show an even lower intensity and when air is reintroduced in the chamber the intensity increases again. The peak wavelength did not seem to move (less than 1nm variation) when the sample was exposed to different environments (variation in as-grown case was 2.5nm). This could be attributed to the effect of TFSI that has already induced a significant p-doping to the material. One further observation which was different in the two samples (as-grown and TFSI-treated) is the following: the PL intensity of the TFSI-treated sample seemed to follow a monotonic increase after its reexposure in air, which was not the case in as-grown sample where the intensity remained quite constant.

4.3.3.5 Impact of irradiation time on PL response in vacuum and in air

We wanted to study the effect of sample's irradiation on the PL emission and how it evolves in time. We used a TFSI-treated sample that was pretreated at 300°C in forming gas. The used pump fluence in all experiments was 340 Wcm⁻² and the laser emitted in 532nm (Verdi). All measurements were taken at room temperature.

In the first experiment, the sample was placed in the vacuum. We used 15 sec exposure time for every measurement with a 5-15sec interval between measurements to save the acquired spectrum. During that time, the sample was not exposed to the laser beam. Before the first measurement, we optimized the focus and then left the sample untouched for 10-15min.

Below, we present the recorded PL spectra and their integrated intensity.

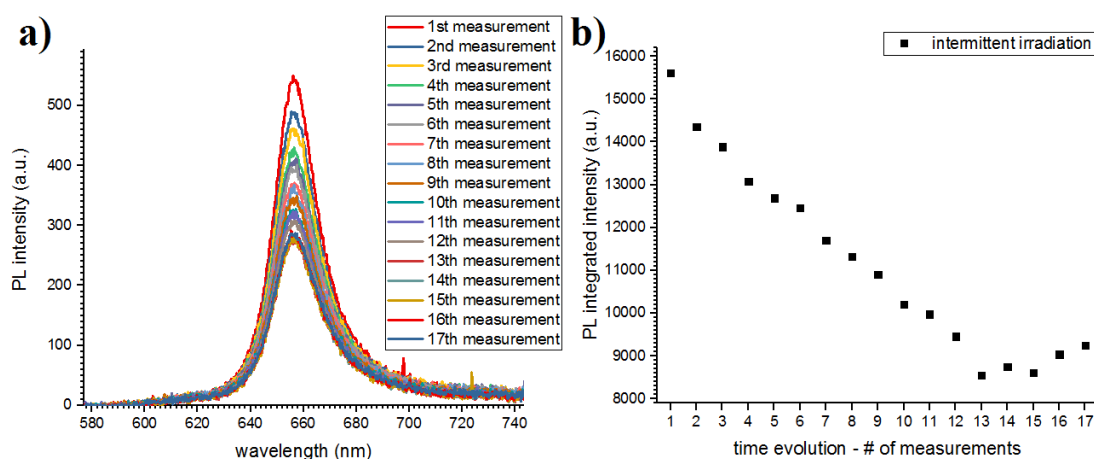


Figure 67: a) Time evolution of the PL spectrum and b) the integrated intensity of the PL peak as a function of number of measurement. The sample had not been exposed to the laser beam during the waiting time between the measurements.

We observe that the PL signal drops monotonically until it stabilizes around 260-390 sec after the first exposure. To check if this effect is associated with exposure to the pump laser we stopped for 13 minutes, letting the sample to rest. We then took one last spectrum. The comparison of the two measurements is presented below.

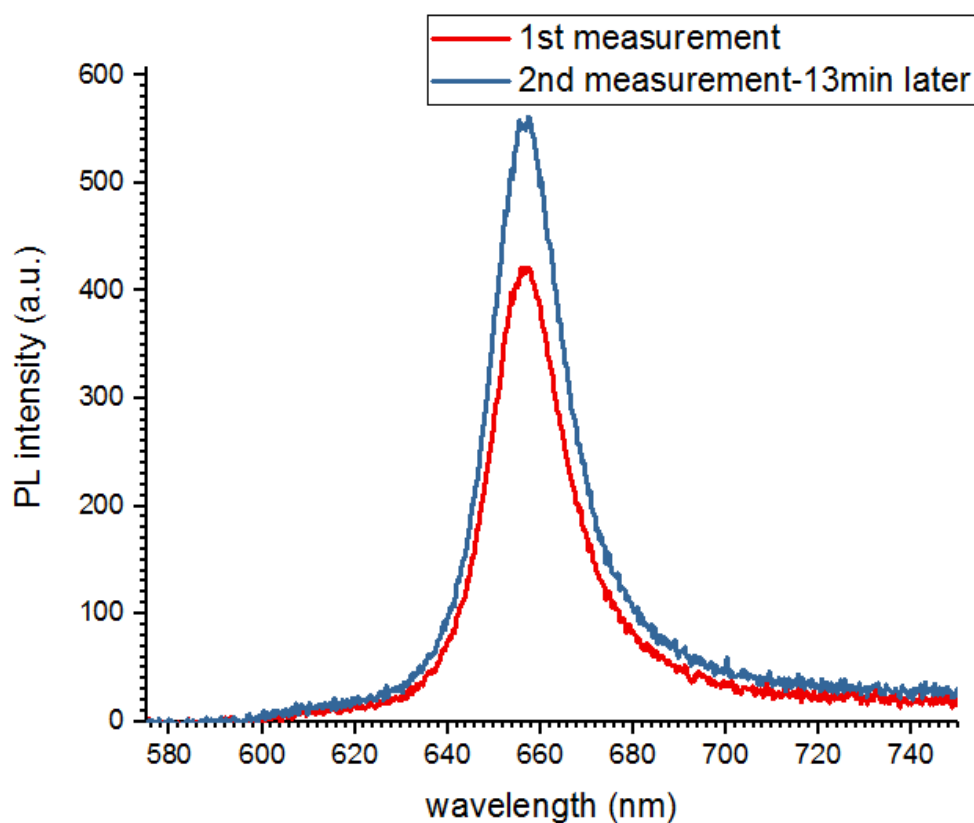


Figure 68: PL spectra comparison of a site after multiple pump laser exposures and the same spot after it was left to recover for 13min.

The PL emission appears to recover after a few minutes. We repeated the same experiment in air (Exposed a site to the pump laser and recorded the PL every 20-30sec). The results are presented below.

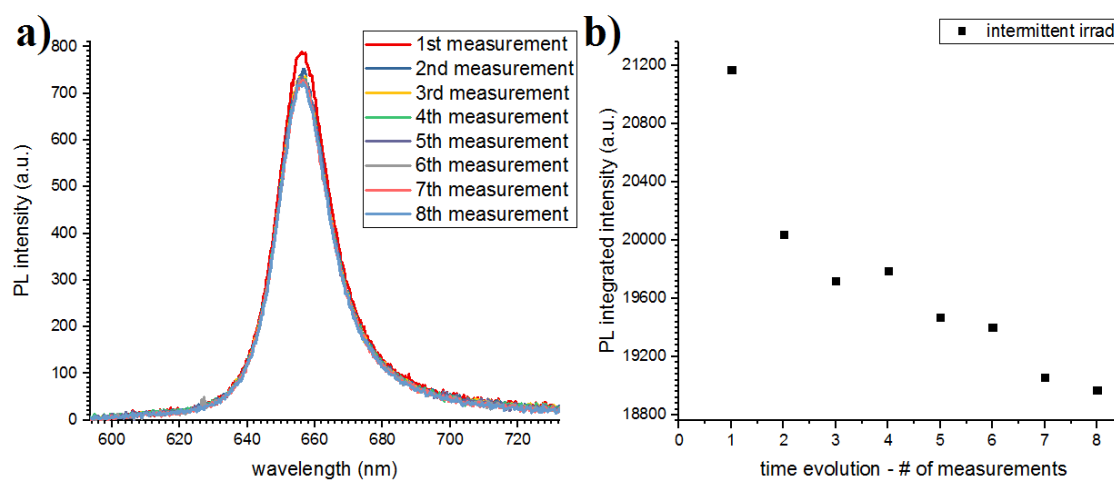


Figure 69: a) Time evolution of the PL spectra and b) the integrated intensity of the PL peak as a function of number of measurement. The sample had not been exposed

to the laser beam during the waiting time between the measurements,

We found that the changes in PL emission are minor (the drop is less than 10%) in contrast to what we observed in vacuum where the intensity dropped by a factor of 2.

Finally, we wanted to check if the recovery time in air is less than 5-15sec and this is the reason why the changes in PL spectrum are so small. So, we repeated the same experiment but this time the pump laser was constantly ON. The results are shown here.

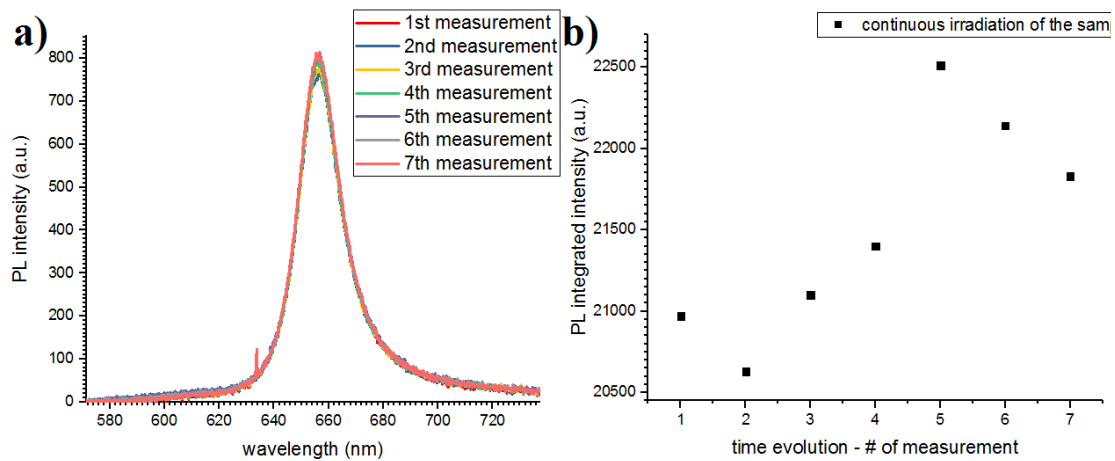


Figure 70: a) Time evolution of the PL spectra and b) the integrated intensity of the PL peak as a function of number of measurement. The sample had been exposed to the laser beam even during the time between the measurements,.

The changes are again very small. So, the sample was not recovering during the measurements in the previous experiment, the effect of irradiation is much smaller in atmospheric pressure (ambient air).

4.4 Encapsulation / Stacking

4.4.1 Encapsulation

The goal was to find if we can stack layers of MoS₂ on top of each other without them interacting (using a spacer). In order to achieve this, we used e-gun evaporation to evaporate 5nm of SiO₂ on the surface of a transferred sample. The samples had been transferred to a DBR/SiO₂ substrate. Two samples were encapsulated this way and the results are systematic. The method was successful but we observed small changes in the Raman and PL emission of the material.

4.4.1.1 Raman spectrum

The Raman spectra of 3 spots were recorded before and after the evaporation using the same parameters with 4.1.2.

The comparison of the spectra of one of the two samples is presented below.

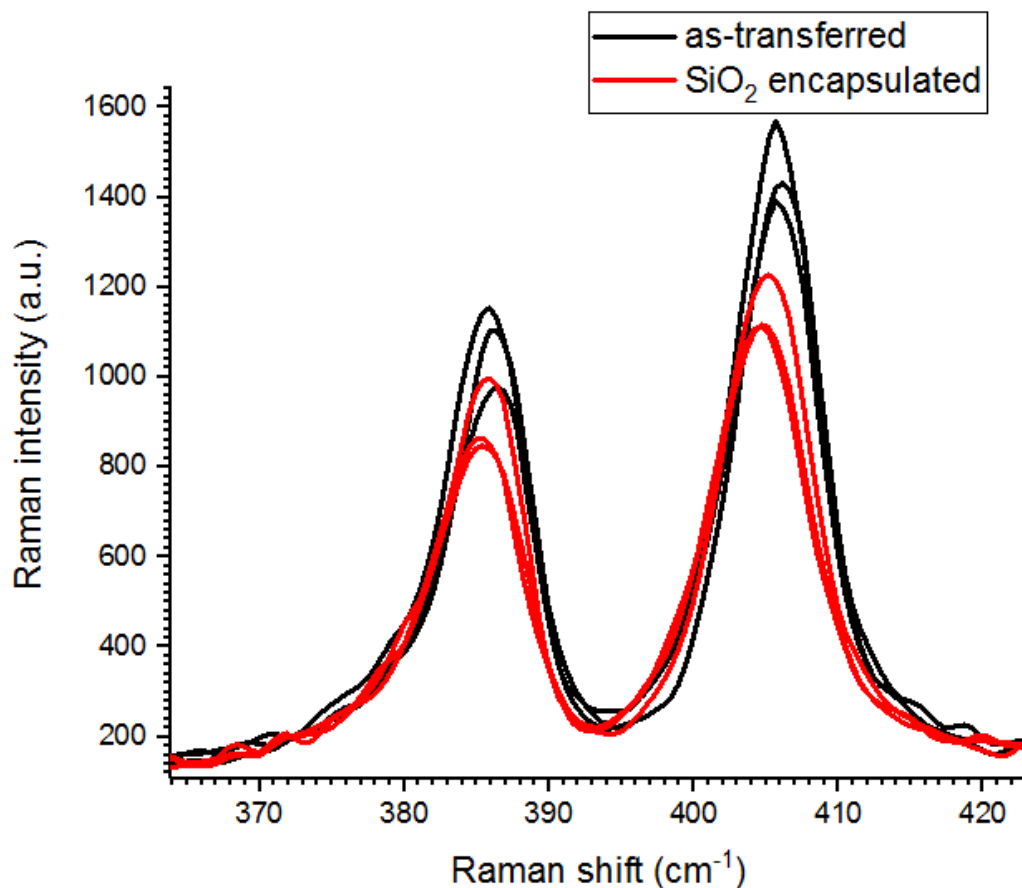


Figure 71: Comparison between the Raman emission of the sample “standard 03” when it was just transferred and after the evaporation of the SiO₂ layer.

From the fitting of the peaks (pseudovoigt), we find that A_{1g} mode softens by 1 cm⁻¹ in both samples that were encapsulated with SiO₂. The linewidth of the mode changes as well but the change is different in the two encapsulated samples and so it is not a consistent phenomenon.

4.4.1.2 PL spectrum

The PL spectra before and after the evaporation of SiO₂ was recorded in the Raman set-up using the same parameters as above. 3 different sites were measured again.

The comparison of the PL emission from a sample before and after it was encapsulated is presented in figure 72.

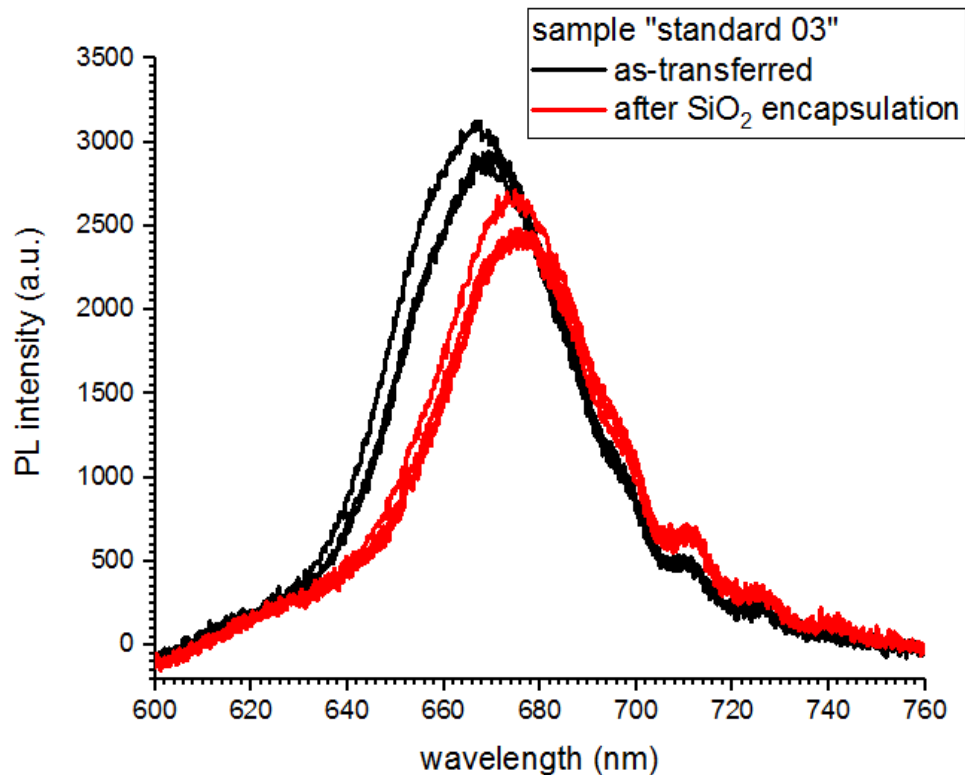


Figure 72: Comparison between the PL emission of the sample “standard 03” when it was just transferred and after the evaporation of the SiO₂ layer.

The peak shifted from around 667nm to 675nm and the intensity was slightly decreased. This could be related to doping induced by the substrate as SiO₂ is known to have a high degree of charge impurities [66] or it could be caused by the absence of interaction with the molecules of the air (absence of physisorption), which again is related to a change in the doping level as discussed previously. The relative population of excitons to trions seems to have decreased. The increased electron density is supported by the Raman findings as well.

4.4.2 Stacking

After the encapsulation of a transferred sample with a thin film of SiO₂ (5nm), we transferred one more sample on top of it. In the optical microscope, we can observe the overlapping monolayer region of the two samples. Finally, we measured its PL and Raman emission using again the same parameters. The Raman spectrum will not be shown as it did not give us any information.

4.4.2.1 Optical microscopy

In the following diagram we observe the two monolayer samples that have been transferred perpendicular to each other.

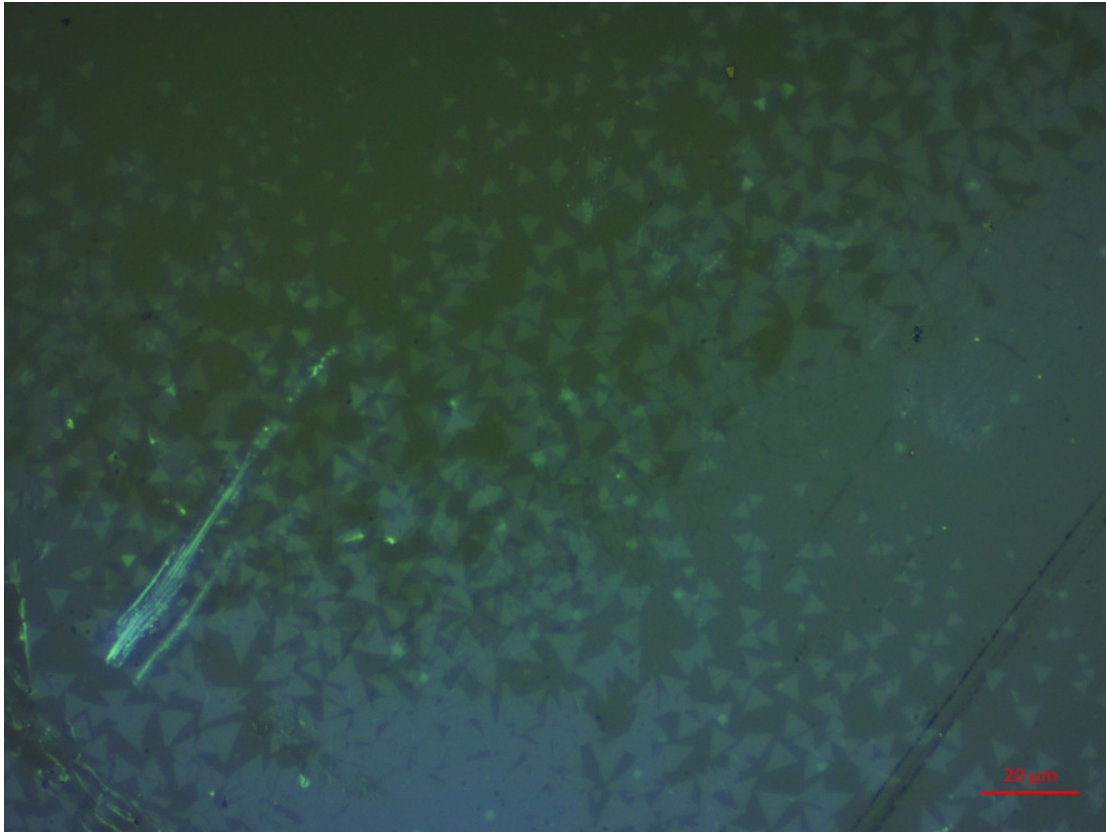


Figure 73: An optical picture where we can distinguish the two layers of MoS₂.

4.4.2.2 PL spectrum

We measured the PL emission of the bottom and upper layer alone and then the emission from the area that they were overlapping. The spectra were recorded using the Raman set-up in PL mode and their comparison is shown below.

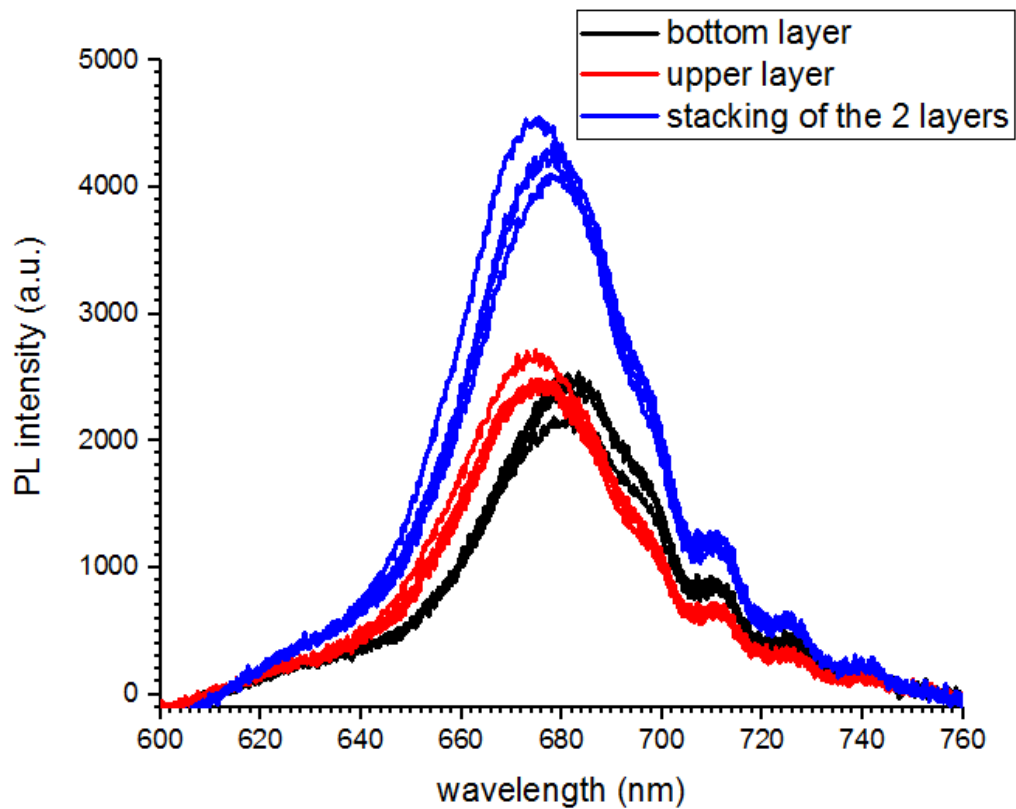


Figure 74: Comparison between the PL emission from the bottom layer, the upper layer and the combination of the two layers. The different curves of the same color represent different sites on the sample.

Both of the monolayers contributed to the total emission resulting in an increased PL intensity as expected.

5 *Conclusions*

In this work, we studied the properties of monolayer MoS₂ and optimized its PL emission. CVD-grown samples were used and the material quality was studied with optical microscopy, Raman and PL measurements. The samples are not completely uniform and we track variations in their Raman and PL response. Power and temperature dependent PL measurements showed that there is a significant amount of defects in the material. Low temperature emission (below 100K) is dominated by bound excitons that have been correlated with defect sites and specifically, S-vacancies. The sublinear power dependence of the emission at room temperature in vacuum and air supports the defective character of the material. These measurements also indicated that there is interaction between air molecules and the sample. This was confirmed by the systematic study of the PL emission as a function of exposure to air, vacuum and an inert gas, N₂.

The transfer process drastically influenced the quality of the samples. The changes in Raman and PL spectrum could have been caused by a combination of strain release, n-doping and possibly generation of defects in the material. We could not quantify the doping and defect variations but we calculated the amount of strain.

The TFSI treatment resulted in a significant improvement of the PL emission (x10-100). Apart of the intensity's enhancement, we noticed further changes in the PL spectrum that are probably associated with p-doping. Despite the great enhancement that it caused in PL emission, the effect is not stable and it diminishes quite quickly (characteristic time of one week). Because of the hypothesis of passivation of defects, we would expect the low temperature PL spectrum to present an increased concentration of free to bound excitons which was not the case here. However, the linear power dependence at room temperature indicated the domination of neutral excitons and passivation of non-radiative pathways. Measuring the sample in different environments (air, vacuum and N₂) lead us to the assumption that the TFSI is not removed in vacuum but the interaction with adsorbates is enhancing the measured response.

Finally, we managed to successfully encapsulate the monolayer with a thin layer of SiO₂ and transfer another monolayer MoS₂ on top improving the total emission twofold.

Further investigation is needed in order to improve the stability and effect of the TFSI. Alterations in the method used until now, such as the change in temperature of pretreatment, can be made for this purpose. The variation in time evolution of different sites on the sample could further help in this direction by systematically studying their differences. Also, the impact of TFSI on samples that have not been transferred to a new substrate (as-grown) has to be elaborated. Other encapsulation techniques apart from e-gun evaporation need to be tested in order to maintain the effect.

Better understanding of the acting mechanism of the treatment is challenging. The time evolution of the effect when the sample is stored in vacuum will help in answering the question if the stability is poor because of interaction of the material with the air molecules. Also, power and temperature dependent measurements need to be done in as-transferred samples in order to ensure if the differences we observed are coming from the TFSI-treatment or the transfer process. The impact of irradiation time on PL response of as-grown and transferred samples will help us understand the interaction of the TFSI with the laser beam. Finally, time and energy resolved Photoluminescence at varying temperature and power will offer vital information on the recombination mechanisms of the material (as-grown, transferred and TFSI-treated).

6 Literature

- [1] X. Li and H. Zhu, “Two-dimensional MoS₂: Properties, preparation, and applications,” *Journal of Materiomics*, vol. 1, no. 1, pp. 33–44, Mar. 2015, doi: 10.1016/j.jmat.2015.03.003.
- [2] M. Ye *et al.*, “Recent Advancement on the Optical Properties of Two-Dimensional Molybdenum Disulfide (MoS₂) Thin Films,” *Photonics*, vol. 2, no. 1, pp. 288–307, Mar. 2015, doi: 10.3390/photonics2010288.
- [3] S. Manzeli, D. Ovchinnikov, D. Pasquier, O. V. Yazyev, and A. Kis, “2D transition metal dichalcogenides,” *Nature Reviews Materials*, vol. 2, no. 8, Art. no. 8, Jun. 2017, doi: 10.1038/natrevmats.2017.33.
- [4] I. Matsuda, *Monatomic Two-Dimensional Layers: Modern Experimental Approaches for Structure, Properties, and Industrial Use*. Elsevier, 2018.
- [5] A. Kuc, “Low-dimensional transition-metal dichalcogenides,” in *Chemical Modelling*, vol. 11, Royal Society of Chemistry, 2014, pp. 1–29.
- [6] J. Xiao, M. Zhao, Y. Wang, and X. Zhang, “Excitons in atomically thin 2D semiconductors and their applications,” *Nanophotonics*, vol. 6, no. 6, 2017, doi: 10.1515/nanoph-2016-0160.
- [7] G. Eda, H. Yamaguchi, D. Voiry, T. Fujita, M. Chen, and M. Chhowalla, “Photoluminescence from chemically exfoliated MoS₂,” *Nano Lett.*, vol. 11, no. 12, pp. 5111–5116, Dec. 2011, doi: 10.1021/nl201874w.
- [8] Y. Lin *et al.*, “Dielectric screening of excitons and trions in single-layer MoS₂,” *Nano Lett.*, vol. 14, no. 10, pp. 5569–5576, Oct. 2014, doi: 10.1021/nl501988y.
- [9] K. S. Novoselov and A. H. C. Neto, “Two-dimensional crystals-based heterostructures: materials with tailored properties,” *Phys. Scr.*, vol. T146, p. 014006, Jan. 2012, doi: 10.1088/0031-8949/2012/T146/014006.
- [10] A. Koma, “Van der Waals epitaxy—a new epitaxial growth method for a highly lattice-mismatched system,” *Thin Solid Films*, vol. 216, no. 1, pp. 72–76, Aug. 1992, doi: 10.1016/0040-6090(92)90872-9.
- [11] J.-H. Park and T. S. Sudarshan, *Chemical Vapor Deposition*, vol. 2. ASM International, 2001.
- [12] P. M. Martin, *Handbook of Deposition Technologies for Films and Coatings: Science, Applications and Technology*, 3 edition. Amsterdam: William Andrew, 2009.
- [13] A. Castellanos-Gomez *et al.*, “Deterministic transfer of two-dimensional materials by all-dry viscoelastic stamping,” *2D Mater.*, vol. 1, no. 1, p. 011002, Apr. 2014, doi: 10.1088/2053-1583/1/1/011002.
- [14] R. Frisenda *et al.*, “Recent progress in the assembly of nanodevices and van der Waals heterostructures by deterministic placement of 2D materials,” *Chem. Soc. Rev.*, vol. 47, no. 1, pp. 53–68, Jan. 2018, doi: 10.1039/C7CS00556C.
- [15] G. Deokar *et al.*, “Towards high quality CVD graphene growth and transfer,” *Carbon*, vol. 89, pp. 82–92, Aug. 2015, doi: 10.1016/j.carbon.2015.03.017.
- [16] H. Van Ngoc, Y. Qian, S. K. Han, and D. J. Kang, “PMMA-Etching-Free Transfer of Wafer-scale Chemical Vapor Deposition Two-dimensional Atomic Crystal by a Water Soluble Polyvinyl Alcohol Polymer Method,” *Scientific Reports*, vol. 6, no. 1, Art. no. 1, Sep. 2016, doi: 10.1038/srep33096.
- [17] M. Amani *et al.*, “High Luminescence Efficiency in MoS₂ Grown by Chemical Vapor Deposition,” *ACS Nano*, vol. 10, no. 7, pp. 6535–6541, Jul. 2016, doi: 10.1021/acsnano.6b03443.

- [18] M. Amani *et al.*, “Near-unity photoluminescence quantum yield in MoS₂,” *Science*, vol. 350, no. 6264, pp. 1065–1068, Nov. 2015, doi: 10.1126/science.aad2114.
- [19] M. Amani *et al.*, “Recombination Kinetics and Effects of Superacid Treatment in Sulfur- and Selenium-Based Transition Metal Dichalcogenides,” *Nano Lett.*, vol. 16, no. 4, pp. 2786–2791, Apr. 2016, doi: 10.1021/acs.nanolett.6b00536.
- [20] F. Cadiz *et al.*, “Well separated trion and neutral excitons on superacid treated MoS₂ monolayers,” *Appl. Phys. Lett.*, vol. 108, no. 25, p. 251106, Jun. 2016, doi: 10.1063/1.4954837.
- [21] A. Alharbi, P. Zahl, and D. Shahrjerdi, “Material and device properties of superacid-treated monolayer molybdenum disulfide,” *Appl. Phys. Lett.*, vol. 110, no. 3, p. 033503, Jan. 2017, doi: 10.1063/1.4974046.
- [22] D. Kiriya *et al.*, “Systematic Study of Photoluminescence Enhancement in Monolayer Molybdenum Disulfide by Acid Treatment,” *Langmuir*, vol. 34, no. 35, pp. 10243–10249, Sep. 2018, doi: 10.1021/acs.langmuir.8b01425.
- [23] Y. Zeng, W. Chen, B. Tang, J. Liao, J. Lou, and Q. Chen, “Synergetic photoluminescence enhancement of monolayer MoS₂ via surface plasmon resonance and defect repair,” *RSC Adv.*, vol. 8, no. 42, pp. 23591–23598, Jun. 2018, doi: 10.1039/C8RA03779E.
- [24] M. R. Molas *et al.*, “Tuning carrier concentration in a superacid treated MoS₂ monolayer,” *Sci Rep*, vol. 9, no. 1, p. 1989, Feb. 2019, doi: 10.1038/s41598-018-38413-6.
- [25] Y. Yu *et al.*, “Enhancing Multifunctionalities of Transition-Metal Dichalcogenide Monolayers via Cation Intercalation,” *ACS Nano*, vol. 11, no. 9, pp. 9390–9396, Sep. 2017, doi: 10.1021/acsnano.7b04880.
- [26] A. Kavokin, J. J. Baumberg, G. Malpuech, and F. P. Laussy, *Microcavities*. Oxford University Press.
- [27] J. Costello, “Quantum Electronics, Laser physics, Chapter 3: The optical resonator,” Dublin City University, Accessed: Apr. 04, 2020. [Online]. Available: <http://www.physics.dcu.ie/~jtc/QE4.pdf>.
- [28] W. Rosenfeld, “A high finesse optical resonator for cavity QED experiments,” Diploma Thesis, Rheinischen Friedrich-Wilhelms-Universität, 2003.
- [29] M. S. Skolnick, T. Fisher, and D. M. Whittaker, “Strong coupling phenomena in quantum microcavity structures,” *Semiconductor Science and Technology*, vol. 13, p. 645, Jan. 1999, doi: 10.1088/0268-1242/13/7/003.
- [30] “Nanophotonics I: Quantum Theory of Microcavities - School of Physics - Trinity College Dublin.” <https://www.tcd.ie/Physics/research/groups/qlamg/teaching/nanophotonics.php> (accessed Apr. 12, 2020).
- [31] Y. Yamamoto, F. Tassone, and H. Cao, *Semiconductor Cavity Quantum Electrodynamics*. Berlin Heidelberg: Springer-Verlag, 2000.
- [32] H. A. MacLeod, *Thin-Film Optical Filters*. CRC Press, 2010.
- [33] A. Eljarrat, “Quantitative methods for Electron Energy Loss Spectroscopy,” PhD thesis, Barcelona, 2015.
- [34] S. J. Byrnes, “Multilayer optical calculations,” *arXiv:1603.02720 [physics]*, Mar. 2016, Accessed: Sep. 03, 2018. [Online]. Available: <http://arxiv.org/abs/1603.02720>.
- [35] D. T. Ha, D. T. Thuy, V. T. Hoa, T. T. T. Van, and N. A. Viet, “On the theory of three types of polaritons (phonon, exciton and plasmon polaritons),” *J. Phys.*:

Conf. Ser., vol. 865, no. 1, p. 012007, 2017, doi: 10.1088/1742-6596/865/1/012007.

- [36] D. Knez, “Plasmons, Polaritons.” [Online]. Available: <https://lampx.tugraz.at/~hadley/ss2/problems/plasmonpolariton/s.pdf>.
- [37] L. K. van Vugt, “Optical properties of semiconducting nanowires,” Mar. 28, 2007. <http://dSPACE.library.uu.nl/handle/1874/20802> (accessed Sep. 03, 2018).
- [38] “What does excitonic interaction mean in terms of wavelength absorption or emission? - Quora.” <https://www.quora.com/What-does-excitonic-interaction-mean-in-terms-of-wavelength-absorption-or-emission> (accessed Sep. 03, 2018).
- [39] O. L. Berman, R. Ya. Kezerashvili, Y. E. Lozovik, and D. W. Snoke, “Bose—Einstein condensation and superfluidity of trapped polaritons in graphene and quantum wells embedded in a microcavity,” *Philosophical Transactions: Mathematical, Physical and Engineering Sciences*, vol. 368, no. 1932, pp. 5459–5482, 2010.
- [40] X. Liu, W. Bao, Q. Li, C. Ropp, Y. Wang, and X. Zhang, “Control of Coherently Coupled Exciton Polaritons in Monolayer Tungsten Disulphide,” *Phys. Rev. Lett.*, vol. 119, no. 2, p. 027403, Jul. 2017, doi: 10.1103/PhysRevLett.119.027403.
- [41] L. C. Flatten *et al.*, “Room-temperature exciton-polaritons with two-dimensional WS₂,” *Scientific Reports*, vol. 6, no. 1, Art. no. 1, Sep. 2016, doi: 10.1038/srep33134.
- [42] S. Wang *et al.*, “Coherent Coupling of WS₂ Monolayers with Metallic Photonic Nanostructures at Room Temperature,” *Nano Lett.*, vol. 16, no. 7, pp. 4368–4374, 13 2016, doi: 10.1021/acs.nanolett.6b01475.
- [43] V. Savona, “Fifteen Years of Microcavity Polaritons,” in *The Physics of Semiconductor Microcavities*, Wiley-Blackwell, 2007, pp. 1–29.
- [44] C. Schneider, M. M. Glazov, T. Korn, S. Höfling, and B. Urbaszek, “Two-dimensional semiconductors in the regime of strong light-matter coupling,” *Nature Communications*, vol. 9, no. 1, Art. no. 1, Jul. 2018, doi: 10.1038/s41467-018-04866-6.
- [45] X. Liu *et al.*, “Strong light–matter coupling in two-dimensional atomic crystals,” *Nature Photonics*, vol. 9, no. 1, Art. no. 1, Jan. 2015, doi: 10.1038/nphoton.2014.304.
- [46] Y.-J. Chen, J. D. Cain, T. K. Stanev, V. P. Dravid, and N. P. Stern, “Valley-polarized exciton–polaritons in a monolayer semiconductor,” *Nature Photonics*, vol. 11, no. 7, Art. no. 7, Jul. 2017, doi: 10.1038/nphoton.2017.86.
- [47] Z. Sun *et al.*, “Optical control of room-temperature valley polaritons,” *Nature Photonics*, vol. 11, no. 8, Art. no. 8, Aug. 2017, doi: 10.1038/nphoton.2017.121.
- [48] S. Dufferwiel *et al.*, “Exciton–polaritons in van der Waals heterostructures embedded in tunable microcavities,” *Nature Communications*, vol. 6, no. 1, Art. no. 1, Oct. 2015, doi: 10.1038/ncomms9579.
- [49] M. I. Vasilevskiy, D. G. Santiago-Pérez, C. Trallero-Giner, N. M. R. Peres, and A. Kavokin, “Exciton polaritons in two-dimensional dichalcogenide layers placed in a planar microcavity: Tunable interaction between two Bose-Einstein condensates,” *Phys. Rev. B*, vol. 92, no. 24, p. 245435, Dec. 2015, doi: 10.1103/PhysRevB.92.245435.
- [50] G. V. Kolmakov, L. M. Pomirchi, and R. Y. Kezerashvili, “Toward room-temperature superfluidity of exciton polaritons in an optical microcavity with an embedded MoS₂ monolayer,” *J. Opt. Soc. Am. B, JOSAB*, vol. 33, no. 7, pp. C72–C79, Jul. 2016, doi: 10.1364/JOSAB.33.000C72.

- [51] “Basic of Raman spectroscopy,” *Nanophoton corp*, Mar. 12, 2019. <https://www.nanophoton.net/raman-spectroscopy/lessons> (accessed Jan. 28, 2020).
- [52] E. Smith and G. Dent, *Modern Raman Spectroscopy – A Practical Approach*. John Wiley & Sons, Ltd, 2005.
- [53] G. Turrell and J. Corset, *Raman Microscopy: Developments and Applications*. Academic Press, 1996.
- [54] X. Zhang, X.-F. Qiao, W. Shi, J.-B. Wu, D.-S. Jiang, and P.-H. Tan, “Phonon and Raman scattering of two-dimensional transition metal dichalcogenides from monolayer, multilayer to bulk material,” *Chem Soc Rev*, vol. 44, no. 9, pp. 2757–2785, May 2015, doi: 10.1039/c4cs00282b.
- [55] “Chapter 4 : Phonons and Crystal vibration.” http://grdelin.phy.hr/~ivo/Nastava/CvrstoStanje/arhiva/udzbenici/Upali_Siriwardane/586c4.htm (accessed Jan. 21, 2020).
- [56] “Spectroscopy Facilities || The Prashant Kamat lab at the University of Notre Dame.” https://www3.nd.edu/~kamatlab/facilities_spectroscopy.html#Pos7 (accessed Aug. 17, 2020).
- [57] C. Lee, H. Yan, L. E. Brus, T. F. Heinz, J. Hone, and S. Ryu, “Anomalous lattice vibrations of single- and few-layer MoS₂,” *ACS Nano*, vol. 4, no. 5, pp. 2695–2700, May 2010, doi: 10.1021/nn1003937.
- [58] A. Molina-Sánchez, “Phonons in single and few-layer MoS₂ and WS₂,” *Phys. Rev. B*, vol. 84, no. 15, Oct. 2011, doi: 10.1103/PhysRevB.84.155413.
- [59] H. Li *et al.*, “From Bulk to Monolayer MoS₂: Evolution of Raman Scattering,” *Advanced Functional Materials*, vol. 22, no. 7, pp. 1385–1390, 2012, doi: 10.1002/adfm.201102111.
- [60] F. Li *et al.*, “Pressure confinement effect in MoS₂ monolayers,” *Nanoscale*, vol. 7, no. 19, pp. 9075–9082, May 2015, doi: 10.1039/c5nr00580a.
- [61] Y. Zhan, Z. Liu, S. Najmaei, P. M. Ajayan, and J. Lou, “Large-Area Vapor-Phase Growth and Characterization of MoS₂ Atomic Layers on a SiO₂ Substrate,” *Small*, vol. 8, no. 7, pp. 966–971, 2012, doi: 10.1002/smll.201102654.
- [62] W. H. Chae, J. D. Cain, E. D. Hanson, A. A. Murthy, and V. P. Dravid, “Substrate-induced strain and charge doping in CVD-grown monolayer MoS₂,” *Appl. Phys. Lett.*, vol. 111, no. 14, p. 143106, Oct. 2017, doi: 10.1063/1.4998284.
- [63] C. Rice *et al.*, “Raman-scattering measurements and first-principles calculations of strain-induced phonon shifts in monolayer MoS₂,” *Phys. Rev. B*, vol. 87, no. 8, p. 081307, Feb. 2013, doi: 10.1103/PhysRevB.87.081307.
- [64] Y. Wang, C. Cong, C. Qiu, and T. Yu, “Raman spectroscopy study of lattice vibration and crystallographic orientation of monolayer MoS₂ under uniaxial strain,” *Small*, vol. 9, no. 17, pp. 2857–2861, Sep. 2013, doi: 10.1002/smll.201202876.
- [65] G. Kukucska and J. Koltai, “Theoretical Investigation of Strain and Doping on the Raman Spectra of Monolayer MoS₂,” *physica status solidi (b)*, vol. 254, no. 11, p. 1700184, 2017, doi: 10.1002/pssb.201700184.
- [66] M. Buscema, G. A. Steele, H. S. J. van der Zant, and A. Castellanos-Gomez, “The effect of the substrate on the Raman and photoluminescence emission of single-layer MoS₂,” *Nano Res.*, vol. 7, no. 4, pp. 561–571, Apr. 2014, doi: 10.1007/s12274-014-0424-0.
- [67] D. Pierucci *et al.*, “Tunable Doping in Hydrogenated Single Layered Molybdenum Disulfide,” *ACS Nano*, vol. 11, no. 2, pp. 1755–1761, Feb. 2017, doi: 10.1021/acsnano.6b07661.

- [68] C. R. Zhu *et al.*, “Strain tuning of optical emission energy and polarization in monolayer and bilayer MoS₂,” *Phys. Rev. B*, vol. 88, no. 12, p. 121301, Sep. 2013, doi: 10.1103/PhysRevB.88.121301.
- [69] A. Castellanos-Gomez *et al.*, “Local Strain Engineering in Atomically Thin MoS₂,” *Nano Lett.*, vol. 13, no. 11, pp. 5361–5366, Nov. 2013, doi: 10.1021/nl402875m.
- [70] H. J. Conley, B. Wang, J. I. Ziegler, R. F. Haglund, S. T. Pantelides, and K. I. Bolotin, “Bandgap engineering of strained monolayer and bilayer MoS₂,” *Nano Lett.*, vol. 13, no. 8, pp. 3626–3630, Aug. 2013, doi: 10.1021/nl4014748.
- [71] D. Lloyd *et al.*, “Band Gap Engineering with Ultralarge Biaxial Strains in Suspended Monolayer MoS₂,” *Nano Lett.*, vol. 16, no. 9, pp. 5836–5841, Sep. 2016, doi: 10.1021/acs.nanolett.6b02615.
- [72] G. Plechinger *et al.*, “Control of biaxial strain in single-layer molybdenite using local thermal expansion of the substrate,” *2D Mater.*, vol. 2, no. 1, p. 015006, Mar. 2015, doi: 10.1088/2053-1583/2/1/015006.
- [73] H. Li *et al.*, “Optoelectronic crystal of artificial atoms in strain-textured molybdenum disulphide,” *Nature Communications*, vol. 6, no. 1, pp. 1–7, Jun. 2015, doi: 10.1038/ncomms8381.
- [74] A. McCreary *et al.*, “Effects of Uniaxial and Biaxial Strain on Few-Layered Terrace Structures of MoS₂ Grown by Vapor Transport,” *ACS Nano*, vol. 10, no. 3, pp. 3186–3197, Mar. 2016, doi: 10.1021/acsnano.5b04550.
- [75] L. Su, Y. Yu, L. Cao, and Y. Zhang, “Effects of substrate type and material-substrate bonding on high-temperature behavior of monolayer WS₂,” *Nano Res.*, vol. 8, no. 8, pp. 2686–2697, Aug. 2015, doi: 10.1007/s12274-015-0775-1.
- [76] S. K. C. R. C. Longo, R. Addou, R. M. Wallace, and K. Cho, “Impact of intrinsic atomic defects on the electronic structure of MoS₂ monolayers,” *Nanotechnology*, vol. 25, no. 37, p. 375703, Sep. 2014, doi: 10.1088/0957-4484/25/37/375703.
- [77] B. Chakraborty, A. Bera, D. V. S. Muthu, S. Bhowmick, U. V. Waghmare, and A. K. Sood, “Symmetry-dependent phonon renormalization in monolayer MoS₂ transistor,” *Phys. Rev. B*, vol. 85, no. 16, p. 161403, Apr. 2012, doi: 10.1103/PhysRevB.85.161403.
- [78] N. Mao, Y. Chen, D. Liu, J. Zhang, and L. Xie, “Solvatochromic Effect on the Photoluminescence of MoS₂ Monolayers,” *Small*, vol. 9, no. 8, pp. 1312–1315, Apr. 2013, doi: 10.1002/smll.201202982.
- [79] M. R. Laskar *et al.*, “p-type doping of MoS₂ thin films using Nb,” *Appl. Phys. Lett.*, vol. 104, no. 9, p. 092104, Mar. 2014, doi: 10.1063/1.4867197.
- [80] Y. Yu, C. Li, Y. Liu, L. Su, Y. Zhang, and L. Cao, “Controlled Scalable Synthesis of Uniform, High-Quality Monolayer and Few-layer MoS₂ Films,” *Scientific Reports*, vol. 3, no. 1, pp. 1–6, May 2013, doi: 10.1038/srep01866.
- [81] M. S. Kim *et al.*, “Biexciton Emission from Edges and Grain Boundaries of Triangular WS₂ Monolayers,” *ACS Nano*, vol. 10, no. 2, pp. 2399–2405, Feb. 2016, doi: 10.1021/acsnano.5b07214.
- [82] K. M. McCreary, A. T. Hanbicki, S. V. Sivaram, and B. T. Jonker, “A- and B-exciton photoluminescence intensity ratio as a measure of sample quality for transition metal dichalcogenide monolayers,” *APL Materials*, vol. 6, no. 11, p. 111106, Nov. 2018, doi: 10.1063/1.5053699.
- [83] W. M. Parkin *et al.*, “Raman Shifts in Electron-Irradiated Monolayer MoS₂,” *ACS Nano*, vol. 10, no. 4, pp. 4134–4142, Apr. 2016, doi: 10.1021/acsnano.5b07388.

- [84] A. Barron, *Physical Methods in Chemistry and Nano Science*, Null. Connexions, Rice University, 2012.
- [85] “Course: SSCP4473 SPECTROSCOPY AND MATERIAL ANALYSIS.” <http://ocw.utm.my/course/view.php?id=351> (accessed Jan. 27, 2020).
- [86] D. R. Paschotta, “Photoluminescence.” <https://www.rp-photonics.com/photoluminescence.html> (accessed Jan. 27, 2020).
- [87] T. H. Gfroerer, “Photoluminescence in Analysis of Surfaces and Interfaces,” in *Encyclopedia of Analytical Chemistry*, American Cancer Society, 2006.
- [88] N. H. Patel, “CHAPTER 2: Basic Principle, Working and Instrumentation of Experimental Techniques,” PhD thesis, Sardar Patel University, 2015.
- [89] “What is the Difference between Luminescence, Photoluminescence, Fluorescence, and Phosphorescence?” by Edinburgh Instruments Direct Industry.” <https://trends.directindustry.com/edinburgh-instruments/project-25178-187746.html> (accessed Jan. 28, 2020).
- [90] A. Splendiani *et al.*, “Emerging Photoluminescence in Monolayer MoS₂,” *Nano letters*, vol. 10, no. 4, pp. 1271–5, Mar. 2010, doi: 10.1021/nl903868w.
- [91] Y. Lin, “Optical properties of two-dimensional transition metal dichalcogenides,” Thesis, Massachusetts Institute of Technology, 2014.
- [92] G. Kioseoglou, A. T. Hanbicki, M. Currie, A. L. Friedman, D. Gunlycke, and B. T. Jonker, “Valley polarization and intervalley scattering in monolayer MoS₂,” *Appl. Phys. Lett.*, vol. 101, no. 22, p. 221907, Nov. 2012, doi: 10.1063/1.4768299.
- [93] A. M. van der Zande *et al.*, “Grains and grain boundaries in highly crystalline monolayer molybdenum disulphide,” *Nature Materials*, vol. 12, no. 6, pp. 554–561, Jun. 2013, doi: 10.1038/nmat3633.
- [94] K. F. Mak *et al.*, “Tightly bound trions in monolayer MoS₂,” *Nature Materials*, vol. 12, no. 3, Art. no. 3, Mar. 2013, doi: 10.1038/nmat3505.
- [95] G. Plechinger *et al.*, “A direct comparison of CVD-grown and exfoliated MoS₂ using optical spectroscopy,” *Semicond. Sci. Technol.*, vol. 29, no. 6, p. 064008, May 2014, doi: 10.1088/0268-1242/29/6/064008.
- [96] T. Korn, S. Heydrich, M. Hirmer, J. Schmutzler, and C. Schüller, “Low-temperature photocarrier dynamics in monolayer MoS₂,” *Appl. Phys. Lett.*, vol. 99, no. 10, p. 102109, Sep. 2011, doi: 10.1063/1.3636402.
- [97] K. He, C. Poole, K. F. Mak, and J. Shan, “Experimental Demonstration of Continuous Electronic Structure Tuning via Strain in Atomically Thin MoS₂,” *Nano Lett.*, vol. 13, no. 6, pp. 2931–2936, Jun. 2013, doi: 10.1021/nl4013166.
- [98] E. Scalise, M. Houssa, G. Pourtois, V. Afanas’ev, and A. Stesmans, “Strain-induced semiconductor to metal transition in the two-dimensional honeycomb structure of MoS₂,” *Nano Res.*, vol. 5, no. 1, pp. 43–48, Jan. 2012, doi: 10.1007/s12274-011-0183-0.
- [99] P. Johari and V. B. Shenoy, “Tuning the Electronic Properties of Semiconducting Transition Metal Dichalcogenides by Applying Mechanical Strains,” *ACS Nano*, vol. 6, no. 6, pp. 5449–5456, Jun. 2012, doi: 10.1021/nn301320r.
- [100] C. V. Nguyen and N. N. Hieu, “Effect of biaxial strain and external electric field on electronic properties of MoS₂ monolayer: A first-principle study,” *Chemical Physics*, vol. 468, pp. 9–14, Apr. 2016, doi: 10.1016/j.chemphys.2016.01.009.
- [101] S. Tongay *et al.*, “Broad-Range Modulation of Light Emission in Two-Dimensional Semiconductors by Molecular Physisorption Gating,” *Nano Lett.*, vol. 13, no. 6, pp. 2831–2836, Jun. 2013, doi: 10.1021/nl4011172.

- [102] S. Mouri, Y. Miyauchi, and K. Matsuda, "Tunable Photoluminescence of Monolayer MoS₂ via Chemical Doping," *Nano Lett.*, vol. 13, no. 12, pp. 5944–5948, Dec. 2013, doi: 10.1021/nl403036h.
- [103] Y. Yu *et al.*, "Engineering Substrate Interactions for High Luminescence Efficiency of Transition-Metal Dichalcogenide Monolayers," *Advanced Functional Materials*, vol. 26, no. 26, pp. 4733–4739, 2016, doi: 10.1002/adfm.201600418.
- [104] S.-L. Li, H. Miyazaki, H. Song, H. Kuramochi, S. Nakaharai, and K. Tsukagoshi, "Quantitative Raman Spectrum and Reliable Thickness Identification for Atomic Layers on Insulating Substrates," *ACS Nano*, vol. 6, no. 8, pp. 7381–7388, Aug. 2012, doi: 10.1021/nn3025173.
- [105] S. Mignuzzi *et al.*, "Effect of disorder on Raman scattering of single-layer MoS₂," *Phys. Rev. B*, vol. 91, no. 19, p. 195411, May 2015, doi: 10.1103/PhysRevB.91.195411.
- [106] S. Tongay *et al.*, "Defects activated photoluminescence in two-dimensional semiconductors: interplay between bound, charged and free excitons," *Scientific Reports*, vol. 3, no. 1, Art. no. 1, Sep. 2013, doi: 10.1038/srep02657.
- [107] A. Zafar *et al.*, "Probing the intrinsic optical quality of CVD grown MoS₂," *Nano Res.*, vol. 10, no. 5, pp. 1608–1617, May 2017, doi: 10.1007/s12274-016-1319-z.
- [108] J. Pandey and A. Soni, "Unraveling biexciton and excitonic excited states from defect bound states in monolayer MoS₂," *Applied Surface Science*, vol. 463, pp. 52–57, Jan. 2019, doi: 10.1016/j.apsusc.2018.08.205.